DESIGN OF A HIGH LUMINOSITY 100 TeV PROTON-ANTIPROTON COLLIDER

A Dissertation
presented in partial fulfillment of requirements
for the degree of Doctor of Philosophy
in the Department of Physics and Astronomy
The University of Mississippi

by

SANDRA JIMENA OLIVEROS TAUTIVA

April 2017

ABSTRACT

Currently new physics is being explored with the Large Hadron Collider at CERN and with Intensity Frontier programs at Fermilab and KEK. The energy scale for new physics is known to be in the multi-TeV range, signaling the need for a future collider which well surpasses this energy scale. A 10^{34} cm^{-2} s^{-1} luminosity 100 TeV proton-antiproton collider is explored with 7$\times$ the energy of the LHC. The dipoles are 4.5 T to reduce cost. A proton-antiproton collider is selected as a future machine for several reasons. The cross section for many high mass states is 10 times higher in $p\bar{p}$ than pp collisions. Antiquarks for production can come directly from an antiproton rather than indirectly from gluon splitting. The higher cross sections reduce the synchrotron radiation in superconducting magnets and the number of events per bunch crossing, because lower beam currents can produce the same rare event rates. Events are also more centrally produced, allowing a more compact detector with less space between quadrupole triplets and a smaller β^* for higher luminosity. To adjust to antiproton beam losses (burn rate), a Fermilab-like antiproton source would be adapted to disperse the beam into 12 different momentum channels, using electrostatic septa, to increase antiproton momentum capture 12 times. At Fermilab, antiprotons were stochastically cooled in one Debuncher and one Accumulator ring. Because the stochastic cooling time scales as the number of particles, two options of 12 independent cooling systems are presented. One electron cooling ring might follow the stochastic cooling rings for antiproton stacking. Finally antiprotons in the collider ring would be recycled during runs without leaving the collider ring, by joining them to new bunches with snap bunch coalescence and synchrotron damping. These basic ideas are explored in this work on a future 100 TeV proton-antiproton collider and the main parameters are presented.

DEDICATION

To my parents for their loving support and encouragement during all these years of study away from home.

To John Acosta, his company in all this time has been the motivation in my academic growth.

ACKNOWLEDGEMENTS

I want to express my deepest gratitude to Dr. Donald Summers and my advisor Dr. Lucien Cremaldi for their helpful contributions to this work. Thanks for their guidance and valuable corrections to this work.

Also, I want to thank Dr. Hailin Sang and Dr. Alakabha Datta for serving as members on my thesis committee and for their suggestions and comments about this work.

TABLE OF CONTENTS

ABSTRACT ii

DEDICATION iii

ACKNOWLEDGEMENTS iv

LIST OF FIGURES viii

LIST OF TABLES xiii

1 INTRODUCTION 1

2 LITERATURE REVIEW 3

2.1 Standard Model 3

2.2 The LHC 4

2.2.1 CERN Proton-Antiproton Collider 6

2.3 The Tevatron at Fermilab 6

2.3.1 The Antiproton Source 7

2.4 Antiproton Cooling 11

2.4.1 RF Bunch Rotation 11

2.4.2 Stochastic Cooling 12

2.4.3 Antiproton Stacking 15

2.4.4 Electron Cooling 17

2.5 Beam Parameters in Particle Accelerators 19

2.6 Synchrotron Radiation 21

2.7 Magnetic Devices in Particle Accelerators 22

2.7.1 Magnetic Dipoles . . . 22
2.7.2 Magnetic Quadrupoles . . . 24
2.7.2.1 Inner Quadrupole System for the Interaction Regions (IP) . . 26
2.7.2.2 Quadrupole Matrix Formalism . . . 28
2.7.3 Lithium Lens . . . 30
2.7.4 Beam Separation Devices . . . 31
2.8 Radio Frequency Cavity . . . 33
2.9 Beam Simulation Programs . . . 35

3 PROTON-ANTIPROTON COLLIDER REMARKS . . . 37
3.1 Cross Section for Higher Masses in pp and $p\bar{p}$ Collisions . . . 37
3.2 Synchrotron Radiation in High Energy Colliders . . . 43

4 ANTIPROTON CAPTURE . . . 45
4.1 Luminosity Requirements . . . 45
4.2 Increase in Antiproton Momentum Acceptance . . . 46
4.3 Antiproton Beam Separation and Transport . . . 50

5 ANTIPROTON COOLING . . . 58
5.1 Debuncher-Accumulator Rings . . . 59
5.2 Debuncher Rings . . . 60
5.3 Electron Cooling System . . . 61
5.4 Recycling of Antiprotons in the Collider Ring . . . 65

6 COLLIDER DESIGN AND PARAMETERS . . . 67
6.1 Collider Layout . . . 67
6.2 Tunneling . . . 71
6.3 Main Dipole Magnets . . . 73
6.4 Parameter Calculation . . . 76

6.5 Inner Quadrupole System 78

7 CONCLUSIONS 82

BIBLIOGRAPHY 85

LIST OF APPENDICES 93

A G4BEAMLINE CODE 94

B MADX PROGRAM FILE 101

VITA 103

LIST OF FIGURES

2.1 The Standard Model. Source: [6] 3

2.2 The Large Hadron Collider LHC. 5

2.3 Fermilab's accelerator chain. 7

2.4 Antiproton Source. Antiprotons are generated in the target station, then enter the Debuncher through of the AP2 line and then are sent to the Accumulator ring to be finally extracted through of the AP3 line. 8

2.5 Fermilab Target Station. 9

2.6 Accumulator Lattice. Source: [12]. 10

2.7 RF Bunch Rotation. (a) A bunch with large energy spread is injected. (b) The bunch starts rotating in phase space. (c) The RF voltage is reduced and starts the adiabatic debunching. (d) The bunch rotation is complete when the energy spread reduction is complete. 12

2.8 Model of Stochastic Cooling. 13

2.9 Cooling and heating effects in terms of the system gain [18]. 15

2.10 Stacking Process. (a) The first bunch is injected. (b) The bunch is moved to the stack region. (c) A second bunch in injected 2.2s later. (d) The second bunch is moved to the stack region. (e) After successive bunch injections a dense core is formed in the stack. 16

2.11 Antiprotons density distribution in the stacking process for the accumulator ring. 16

2.12 Accumulator Cooling Systems. Figure adapted from [12]. 17

2.13 Principle of electron cooling. The high energy spread of the antiprotons is reduced when they are injected into a cooling section to interact with electrons with low energy spread. 18

2.14 Phase space of a beam with the form of an ellipse. The coordinate u represents the position x or y. 20

2.15 Magnetic Dipole. Source: [25]. 23

2.16 A Dipole bends particles according to their momentum. 24

2.17 Magnetic quadrupole. Source: [25]. The magnetic field is proportional to the radial direction and is zero at the center. 25

2.18 Magnetic focusing and defocusing quadrupole. 25

2.19 Quadrupole FODO Cell. A focusing (F) and defocusing (D) quadrupole separated by a drift space. 26

2.20 Inner quadrupole system to provide the final focusing for the collision of the particle beams. 27

2.21 Inner triplet quadrupole scheme for CMS and ATLAS. 27

2.22 Inner triplet quadrupole scheme for the Tevatron (Fermilab). 27

2.23 Initial vector coordinates (x_0, x_0') entering a lens and final vector coordinates (x_1, x_1') leaving the lens. 28

2.24 A lithium lens collecting particles and orientating them horizontally. 30

2.25 Beam deflection produced by an electric septa. 31

2.26 Electrostatic septum used to extract one part of the beam [26]. 32

2.27 DC Magnetic Septum. The beam is separated into two parts, one enters in the field region B and the other part continues without change in the no field region. 33

2.28 Radio Frequency Cavity. Source: [28]. 34

2.29 Electric and magnetic fields in a cavity. The electric field accelerates or decelerates the particles according to their arrival time. 34

2.30 Simulation example in G4beamline. A flat beam goes through two quadrupole magnets which focus the beam in a specific region [30]. 35

2.31 MAD-X Betatron Function Plot for the CMS Interaction Region. 36

3.1 Cross sections in term of the mass for the Higgs production at E_{cm} =7 TeV [41]. 38

3.2 Top-like Anti-top-like Cross section production as a function of the mass using pp and $p\bar{p}$ collisions [39]. 39

3.3 Feynman Diagrams for W' production from a) $q\bar{q}$ collision, b) qq collision. . . 41

3.4 MadGraph results for W' Boson production cross section as a function of the mass using pp and $p\bar{p}$ collisions with a E_{cm} = 100 TeV. 42

3.5 Pythia results for W' Boson production cross section as a function of the mass using pp and $p\bar{p}$ collisions with a E_{cm} = 100 TeV. 42

4.1 Momentum distribution of the antiprotons produced by a 120 GeV proton beam hitting a tungsten target [51]. 47

4.2 8.9 GeV/c$\pm$ 2% antiproton beam simulation crossing a lithium lens. The plots show the transverse momentum distribution of the beam before entering (left plot) and in the output of the lithium lens (right plot). 48

4.3 11 GeV/c $\pm$ 24% antiproton beam simulation crossing a lithium lens in G4beamline. The plots show the transverse momentum distribution of the beam before entering (left plot) and in the output of the lithium lens (right plot). 49

4.4 Momentum vs x position for the initial beam (left plot) and the dispersed beam (right plot). 51

4.5 Configuration to divide the beam into two parts. An initial beam with momentum acceptance p = 11.0 GeV/c $\pm$ 24% is collected by the Li lens and dispersed by a magnetic dipole to be then divided by a electrostatic septa ES and two magnetic dipoles MS. 51

4.6 Momentum distribution of the initial beam (upper plot) and when it is divided into two (bottom plot). 53

4.7 An initial beam with momentum acceptance p = 11.0 GeV/c $\pm$ 24%is divided to finally get twelve beams. 54

4.8 Momentum distribution of the beams 1, 2 and 3. 55

4.9 Momentum distribution of the beams 4, 5 and 6. 55

4.10 Momentum distribution of the beams 7, 8 and 9. 56

4.11 Momentum distribution of the beams 10, 11 and 12. 56

5.1 To cool 12× more antiprotons, 12 independent cooling systems would be implemented. Two accumulator rings can keep up with one $40 \times 10^{10}\,\bar{p}$/h Debuncher output rate. 59

5.2 12 independent cooling systems using only Debuncher rings. Alternatively, bunch coalescing might be done with electron rather than stochastic cooling. 60

5.3 Antiprotons are sent alternatively from the target to each Debuncher to increase the cooling time from 2.2 to 4.4 s, allowing emittance (RMS, Normalized) reduction from 330 to 3 μm. 61

5.4 Fermilab Electron Cooling System [59]. 62

5.5 Electric fields at the beam pipe center and wall of a circulating beam. 64

5.6 Snap Bunch Coalescing. (a) A group of bunches are centered at low frequency and their momentum spread is reduced. From (b) to (c) the bunches are rotated for 1/4 of a synchrotron oscillation period at low frequency and then captured at high frequency. The momentum spread increases and the bunches are captured in a single bucket. 65

6.1 100 TeV proton-antiproton collider (not to scale). An intermediate energy ring between 120 GeV and 22 TeV is not shown. Bunch stacking in the single electron cooling ring might replace the 24 Accumulator rings. A bit of additional transverse cooling would have to be coaxed out of the Debuncher rings to allow electron cooling. 68

6.2 Possible scenario to construct the 270 km ring in Illinois connected to Fermilab. An engineering study has been done for a 233 km ring at Fermilab [79, 80]. Map data: Google. 69

6.3 Layout of the 270 km ring around Dallas, Texas [83]. Map data: Google. . . . 70

6.4 80 -100 km tunnel to host a 100 TeV pp collider at CERN in the Lake Geneva valley. Image credit: CERN. 71

6.5 LHC Main Dipole Magnet. There are two cosθ layers [87]. 73

6.6 4.5 T superferric dual bore dipole magnet [5]. A $p\bar{p}$ collider would only require one bore. 74

6.7 4.5 T superferric dual bore dipole magnetic design [5]. A $p\bar{p}$ collider would only require one bore. 74

6.8 Beta function plots for the D0 Experiment interaction region. 79

6.9 Beta functions plots for the 100 TeV $p\bar{p}$ collider interaction region. A combination of quadrupoles focus the beam in the IP with $\beta^* = 14$ cm. 80

LIST OF TABLES

2.1 Parameter list for Tevatron and LHC Colliders. 21

2.2 Longitudinal emittance damping time for Tevatron and LHC Colliders. 22

3.1 Synchrotron Radiation (SR) for a 100 km pp and 270 km $p\bar{p}$ circumference colliders. γ = E/m = 53,300. 50 TeV beam energy. 43

4.1 Parameters of the basic cell to divide the initial beam. 53

4.2 Mean momentum value of the 12 beams obtained. 57

5.1 Fermilab antiproton cooling stages [54]. The normalized rms emittance shown comes from multiplying geometric rms emittance by $\beta\,\gamma$ = p/m = 8.9/0.938 = 9.49. A modest amount of stochastic cooling is performed in the Recycler ring to prepare for electron cooling in the same ring. 58

5.2 Electron Cooling System Main Parameters. 62

5.3 Electron Ring Main Parameters. 63

6.1 Comparison between tunneling cost for three different locations considered for a 270 km collider ring [85]. 72

6.2 Tunneling-time estimate. 72

6.3 Main Dipole Magnets for the 270 km collider ring. 75

6.4 Parameter list for the Tevatron, the LHC, the Future Circular Collider FCC-hh, and the 100 TeV $p\bar{p}$ proposed here. 76

6.5 Inner Triplet Quadrupole parameters 81

CHAPTER 1

1 INTRODUCTION

With the recent discovery of the Higgs boson the standard model of particle physics is complete, but exploration will continue to search for beyond the standard model (BSM) physics that many agree must exist. The CMS and ATLAS experiments at the LHC (Large Hadron Collider) observed a Higgs boson with mass of about 125 GeV, using a data sample with collision energies of 7 and 8 TeV [1, 2]. The LHC started taking data at 13 TeV in 2015, and it will continue increasing the number of collisions. The LHC reached its design luminosity of 10^{34} cm^{-2} s^{-1} in June 2016.

The second most powerful hadron collider was the Tevatron at Fermilab. This collided protons and antiprotons with a center of mass energy of 1.96 TeV. During its 28 years of operation (closing in 2011) one of its greatest discovery was the top quark in 1995 [3, 4]. Currently Fermilab experimenters will continue analyzing previous data and new particle research projects are under development. Among them are new high intensity neutrino and muon decay experiments.

Many agree that hadron colliders beyond 14 TeV are necessary to fully explore new BSM physics. For that reason, some projects are being carried out, as for example, a 100 TeV proton-proton collider in a 100 km ring with 16 T Nb_3Sn dipoles is being considered for CERN. Synchrotron radiation in the dipoles, 16 T fields, and detector pileup are concerns. The design is challenging. Might a simpler hadron collider be possible? This is the motivation to consider the construction of a high energy proton-antiproton ($p\bar{p}$) collider. The center of mass energy considered would be 100 TeV with a luminosity of 10^{34} cm^{-2}s^{-1}, and would use 4.5 T NbTi superferric dipoles [5] in a 270 km tunnel. Much of the technology for this

collider is available and was demonstrated at the Tevatron ($\mathcal{L}$ = 4 x 10^{32} $cm^{-2}s^{-1}$). The most important factor in the study of a 100 TeV $p\bar{p}$ machine would be to find a way to cool and recycle more antiprotons to achieve higher luminosity.

The main literature review of this work is presented in chapter 2, mainly about the Tevatron antiproton source and some concepts in accelerator physics.

In chapter 3, we present the important advantages of a high energy(HE) $p\bar{p}$ collider with respect to a HE pp collider. Cross sections for the production of many high mass objects are much larger in $p\bar{p}$ collisions. Calculations and results are shown and compared for both types of colliders. Furthermore, advantages deduced from these calculations are discussed.

In chapter 4 we discuss some important aspects in achieving higher luminosities with proton-antiproton colliders. Among those is, increased momentum acceptance in a Fermilab-like antiproton source to get more antiprotons and the separation of them into 12 different momentum channels.

Chapter 5 is dedicated to the cooling of the antiprotons. This process is important to control the random motion of the particles and beam emittance. Also, because 12 times more antiprotons are needed, twelve independent cooling systems are proposed. One option uses Debuncher and Accumulator rings and a second option uses only Debuncher rings. Finally, an electron cooling ring would follow either of the two cooling system options.

Chapter 6 focuses on the final collider parameters together with relevant calculations. We discuss the beam optics necessary to achieve lower values of β^* for achieving higher luminosity.

Finally in chapter 7 the conclusions of this work are presented.

CHAPTER 2

2 LITERATURE REVIEW

2.1 Standard Model

The standard model of particle physics is based on fundamental particles called fermions and bosons. Fermions are spin 1/2 particles which include quarks and leptons. Bosons are particles having integer spin, including the fundamental force carriers: the photon, the W and Z bosons, the gluon, and the Higgs boson. The structure of the standard model is shown in Fig. 2.1, where it is observed that the fundamental quarks and leptons form a fermion group and the force carrying bosons together with the Higgs form the boson group.

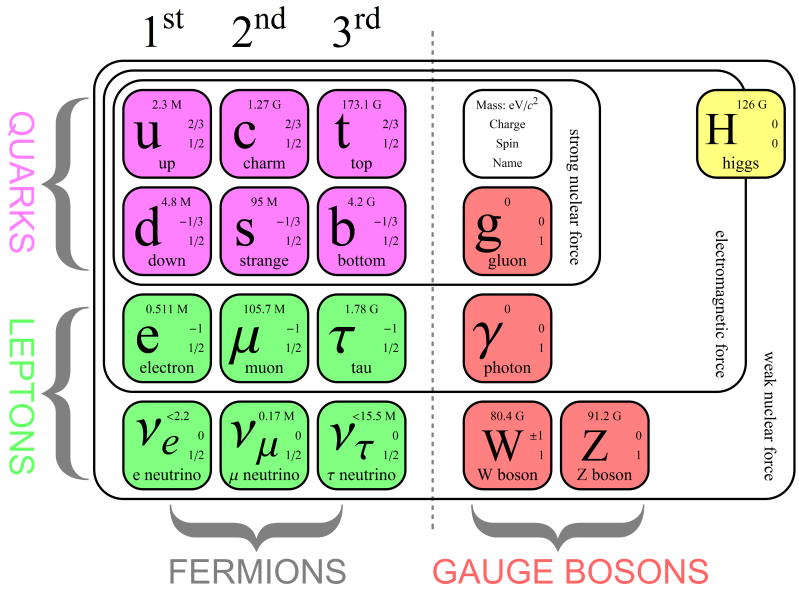

Figure 2.1. The Standard Model. Source: [6]

Looking more closely, there are six types or "flavors" of quarks grouped by generations. The quarks, up and down, belong to the first generation which are the most stable

and least massive. For the second generation we have the quarks, charm and strange, and the third one the quarks, top and bottom, which are more massive. The quarks cannot exist alone, thus a quark and antiquark form the mesons (pion π, kaons K, eta η, rho ρ, omega ω, phi ϕ, etc.). The combination of three quarks qqq (or antiquarks $\bar{q}\bar{q}\bar{q}$) form the baryons. These are massive particles, among which are the proton p and neutron n. Other baryons are the lambda (Λ), sigma (Σ), delta (Δ), chi (ξ), and omega(Ω). The individual quarks have fractional electric charge, $\pm$e/3 or $\pm$2e/3, but they combine to form hadrons (mesons and baryons) which have integer charge as they hadronize.

The leptons are classified by generation, in which the electron, e, has the least mass and the tau lepton, τ, the greatest mass. The muon, μ, and the tau are unstable particles with a lifetime of 2.2 μs and 0.29 ps, respectively. The electron, muon, and tau each have an associated neutrino, ν_e, ν_μ, ν_τ. These neutrinos have no charge and their masses are slightly above zero. Neutrinos interact with matter through the weak interaction.

Five particles form the group of the gauge bosons: the gluon, photon, W, Z, and the most recent Higgs boson. These gauge bosons are the force-carrying particles. The gluon is the mediator of the strong force, which binds protons and neutrons together inside the nucleus. The photon mediates the electromagnetic force which acts between charged particles; for example, it binds electrons to the nucleus. The weak force, which describes β-decay, is carried by the bosons W and Z.

2.2 The LHC

The Large Hadron Collider (LHC), Fig. 2.2, is a circular accelerator of 27 km circumference located 100 m underground near Geneva, Switzerland. It was built by CERN (European Organization for Nuclear Research) in order to explore new physics at the energy scale of the order of 14 TeV. It is designed for proton-proton collisions. The protons are accelerated in groups of 1.15 x 10^{11} interacting every 25 ns from opposite directions at the interaction point (IP). There are about 20-40 proton-proton inelastic collisions at the IP each

25 ns and a few high transverse momentum interactions, possibly with high mass particles. Its biggest goal was the search of the Higgs Boson, a particle that plays a fundamental role in the Standard Model of elementary particle physics.

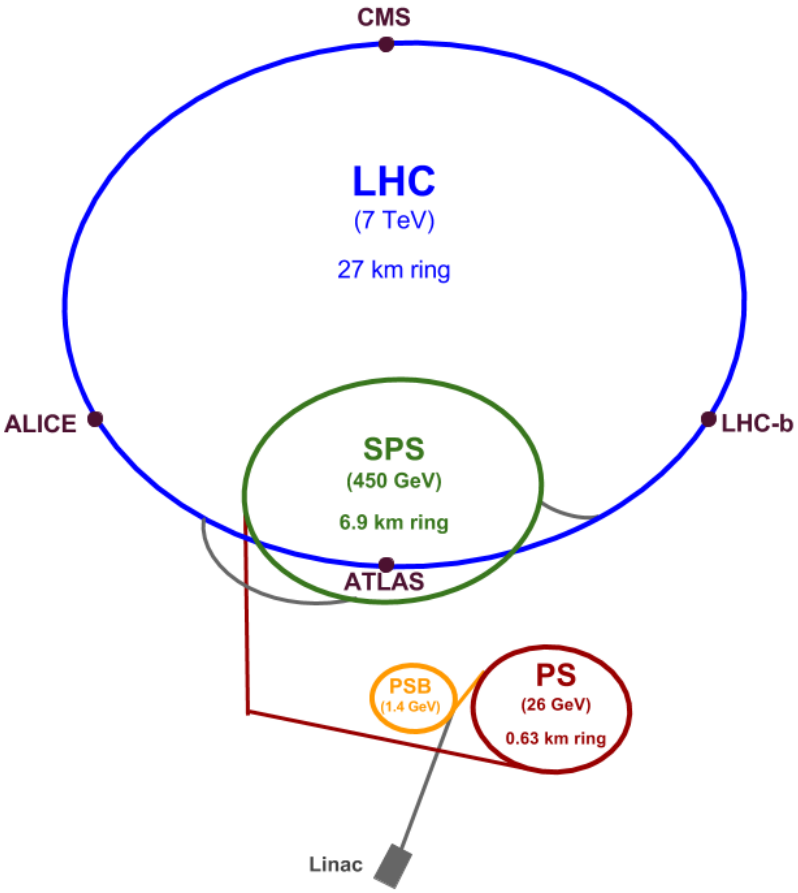

Figure 2.2. The Large Hadron Collider LHC.

At the LHC the injections chain starts with a proton linear accelerator that accelerates protons to an energy of 50 MeV. The Proton Synchrotron Booster (PSB) accelerates the protons to the energy of 1.4 GeV. The particles are then injected in to the Proton Synchrotron (PS), which produces proton bunches with 25 ns spacing. From there they are directed to the 6.9 km Super Proton Synchrotron (SPS) ring where they are accelerated to an energy of 450 GeV. Finally two proton beams (2808 bunches each) are injected into the 27 km LHC

ring to be accelerated to an energy of 7 TeV in opposite directions. The LHC ring uses two pipes, one for each beam. Four experiments, CMS, ATLAS, LHCb and ALICE, are located at the four interaction points of protons. The CMS and ATLAS experiments are of general purpose type and their objective is to explore the limits of the Standard Model. LHCb and ALICE are smaller experiments. The LHCb experiment focuses on bottom quark (b) physics and ALICE focuses on heavy ion physics.

2.2.1 CERN Proton-Antiproton Collider

The Super Proton Synchrotron (SPS) was used as a $p\bar{p}$ collider [7]. From the SP ring a 26 GeV proton beam hit a Cu target, from which antiprotons are created. For each proton beam (10^{23} protons) around 7×10^6 antiprotons were created. Only those with momentum p = 3.5 GeV/c $\pm$ 1.5% were selected, which is the SPS momentum acceptance. The first collisions were observed in 1981 with a 0.55 TeV collision energy. Then, in 1982 the W boson was discovered [8, 9], and with an increase in luminosity the Z boson was discovered in 1983 [10,11]. Its last run occurred circa 1989 in time for CERN to begin building the Large Electron Positron Collider, LEP. However, CERN still produces antiprotons for antimatter experiments.

2.3 The Tevatron at Fermilab

The Tevatron was the largest circular proton-antiproton collider built to date. In 1985 its first proton-antiproton collisions with a center of mass energy E_{cm} of 1.6 TeV were produced. The Tevatron finished operations at the end of September in 2011 with E_{cm} of 1.96 TeV. One of its greatest discovery was the top quark in 1995.

The Tevatron accelerator chain of components (Fig. 2.3) are the Cockcroft-Walton Accelerator, in which hydrogen gas is ionized to H^- and accelerated to 750 keV, the Linac (Linear accelerator), where the H^- ions are accelerated to an energy of 400 MeV. Then, they pass through a thin carbon foil, which removes the electrons leaving only protons. The Booster (circular accelerator) accelerates the protons to 8.9 GeV in 20,000 revolutions. Then,

the accelerated protons enter the Main Injector, where some are accelerated to 150 GeV to be injected into the Tevatron. The remainder are accelerated to 120 GeV and sent to the antiproton source, where the antiprotons are produced. In the Main Injector, the protons and antiprotons are accelerated to 150 GeV and injected into the Tevatron. There, protons and antiprotons are accelerated until they reach an energy of 0.98 TeV per beam prior to collision. In the Tevatron the proton and antiproton beams are collided at the CDF and D0 detectors.

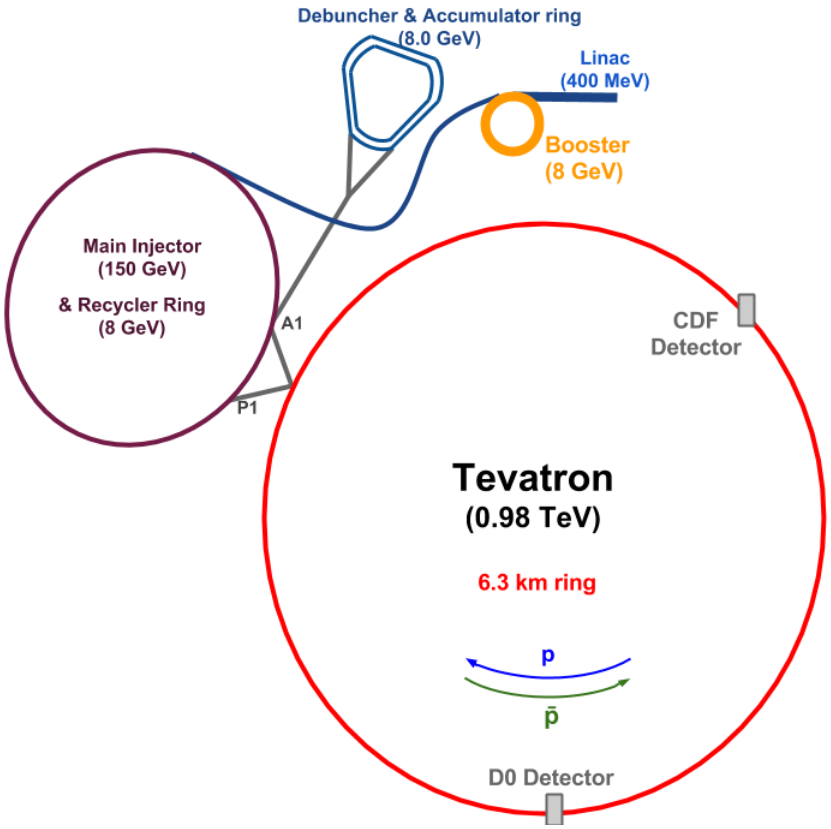

Figure 2.3. Fermilab's accelerator chain.

2.3.1 The Antiproton Source

The antiproton source consists of four parts (Fig. 2.4), the target station and three storage rings: the Debuncher, the Accumulator, and the Recycler (not shown in the figure).

In the target station, Fig. 2.5, around 2.0×10^8 antiprotons of energy 8.94 GeV (peak Booster energy) are created every 2.2 s by hitting the 8 cm long nickel target with a beam of 8×10^{12} protons (120 GeV) coming from the main injector. Then a lithium lens (the least dense solid conductor) is used to horizontally and vertically focus the particles into a beam line, acting like magnetic quadrupoles. Using a pulsed magnet the particles are separated according to their charge. The negatively charged particles are mainly antiprotons and pions. The remaining particles are absorbed by a graphite-core beam dump. The antiprotons production rate depends on the proton beam energy. The antiproton collection efficiency (from the target) is greater if the proton beam spot size on the target is reduced.

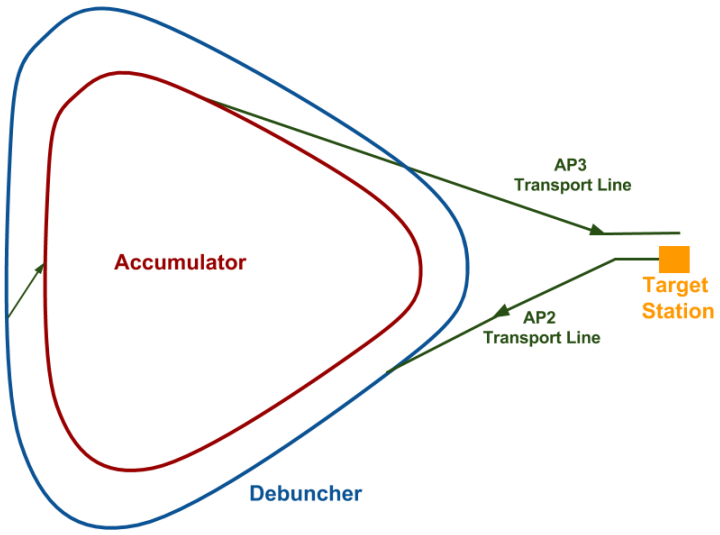

Figure 2.4. Antiproton Source. Antiprotons are generated in the target station, then enter the Debuncher through of the AP2 line and then are sent to the Accumulator ring to be finally extracted through of the AP3 line.

The Debuncher is a 500 m round triangle storage where the antiprotons are collected from the target station. It is divided into 6 sectors, which contain 19 quadrupole magnets, 11 dipoles, a system of correction dipoles to control the beam and a system of sextupoles for chromaticity control. In the Debuncher the momentum spread of the 8.9 GeV/c antiprotons

is reduced using RF bunch rotation. The Debuncher supplies around 40 $\times$ 10^{10} $\bar{p}$/h to the Accumulator. From the Debuncher the 8.9 GeV/c antiprotons are sent to the Accumulator.

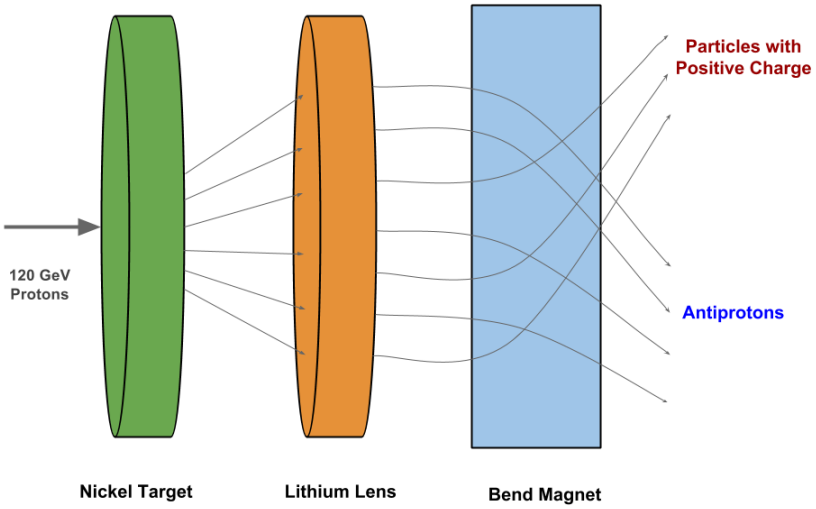

Figure 2.5. Fermilab Target Station.

The Accumulator, Fig. 2.4, is a 474 m rounded triangular shape (6 straight sections and 6 flattened corners) designed to store, cool, and stack the antiprotons. In the arc sections the dispersion (beam separation according to its momentum) is large ($\sim$ 9 m), and the straight sections have low and high dispersion. Fig. 2.6 shows a lattice of the Accumulator, which represents one sector of the six, where 14 quadrupoles (QF, QD), 5 sextupoles, 5 dipoles, and other devices are located. In the sectors A10 and A20 are located the cooling systems. In the Accumulator the antiprotons are stacked and cooled using a cooling process called stochastic cooling; this method will be explained in the next section. The maximum stack of antiproton into the Accumulator is 150 x 10^{10}. It supplies around 25 $\times$ 10^{10} $\bar{p}$/h to the Recycler. The transfer time of antiprotons from the Accumulator to the Recycler is 30 minutes.

The Recycler is an 8.9 GeV/c storage ring located in the main injector tunnel, on the top of the Main Injector Ring, with the same circumference (3.32 km). In the Recy-

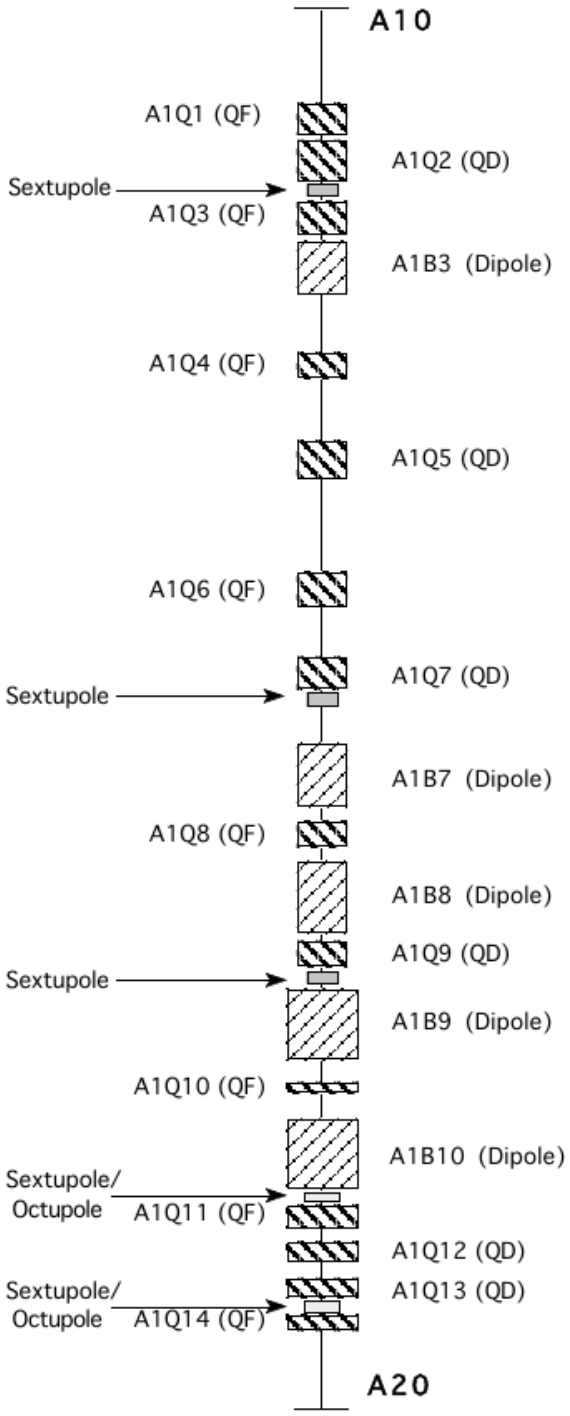

Figure 2.6. Accumulator Lattice. Source: [12].

cler Ring there are approximately 344 permanent magnets, which provide bending and 100 permanent quadrupoles to perform optical focusing. Its initial purpose was to recycle the

unused antiprotons from the collisions, as well as to accumulate large quantities of antiprotons (around 600 $\times$ 10^{10}) [13]. However, the recycler proved not to be effective in recycling antiprotons and therefore it was never used for that purpose. But it was useful for storing and cooling antiprotons. In the scheme more antiprotons can be stored prior to collision, increasing luminosity. With this new ring the number of stored antiprotons was increased to 350-450 x 10^{10} $\bar{p}$. The antiprotons are stored for about 15 hours and then sent to the Main Injector. The storage efficiency of 93% is determined by the loss in injection and extraction processes (4%) and by of the antiproton beam lifetime (3%). In the Recycler the antiprotons are initially cooled by stochastic cooling and then by electron cooling. These cooling systems are explained in the next section.

2.4 Antiproton Cooling

The cooling process in a beam is very important to its quality, allowing the collision of beam bunches. The cooling process consists of reducing the random motion of the beam or its phase space volume. Several types of beam cooling are in use. The random motion of antiprotons can be reduced by stochastic and electron cooling. Cooling by synchrotron radiation damping is used for electron and positron storage rings [14]. Laser cooling [15] is used for ions and ionization cooling [16] can be used for muons.

2.4.1 RF Bunch Rotation

In this process a bunch of antiprotons, initially with large energy spread, is rotated (90°) in phase space reducing the energy spread through RF voltage manipulations [17], as seen in the Fig. 2.7. This technique is used in the Debuncher ring to reduce the momentum spread of the antiprotons from 2.25% to 0.1%, which it takes around 60 ms. The rest of the time (2.2s), the antiprotons are cooled through stochastic cooling to reduce the RMS Normalized emittance from 330 to 30 μm. Longitudinal stochastic cooling is employed as well. The Debuncher Ring is called the debuncher because the small bunch momentum spread comes at the cost of longer bunches.

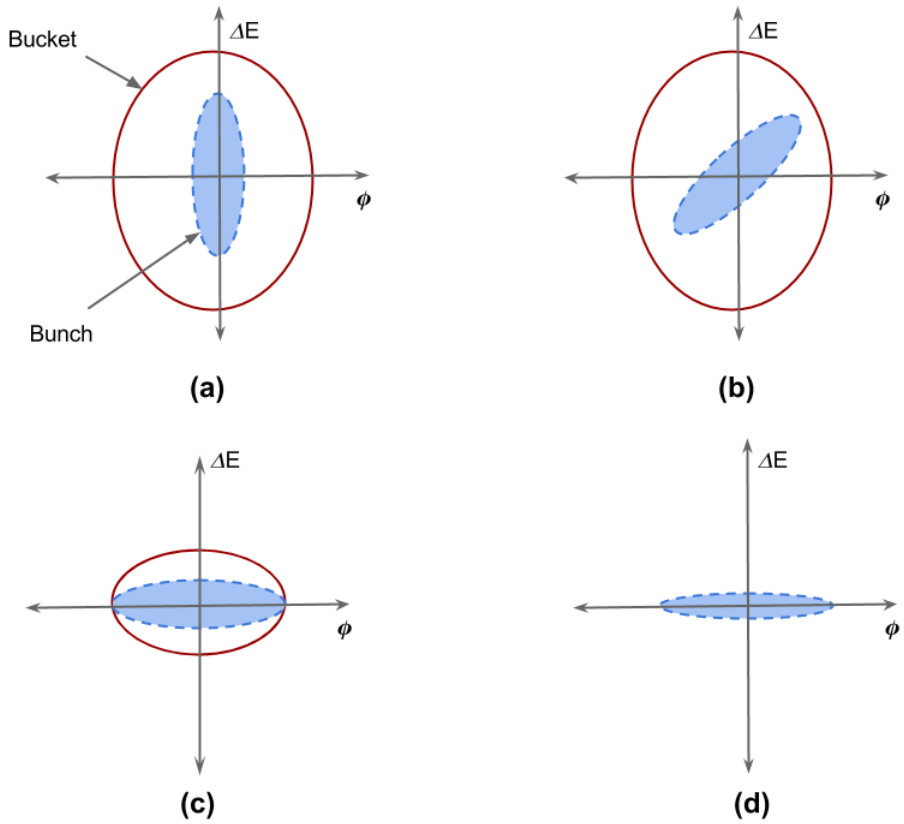

Figure 2.7. RF Bunch Rotation. (a) A bunch with large energy spread is injected. (b) The bunch starts rotating in phase space. (c) The RF voltage is reduced and starts the adiabatic debunching. (d) The bunch rotation is complete when the energy spread reduction is complete.

2.4.2 Stochastic Cooling

The stochastic cooling principle was initiated by Simon van der Meer in 1972. He received a Nobel Prize in 1984 for his work. The cooling consists of reducing the transverse size, transverse angles, the longitudinal size, and the momentum spread ($\Delta p/p$) of a particle beam, with minimal beam loss. The relative velocity of the particles with respect to each other in a bunch is reduced. Stochastic cooling covers both betatron and momentum cooling. Betatron (or transverse) cooling refers to the reduction of the betatron oscillation in the horizontal and vertical transverse planes, while momentum cooling refers to the reduction in momentum spread of the particles in the beam. In these processes, particles can be

considered as points with some empty space between them allowing conservation of density in small scale [18]. For this reason the Liouville theorem [19], which states the phase space density must remain constant, would not be violated. Stochastic cooling is a not conservative process. Kickers can cool a bunch as long as the number of particles is finite.

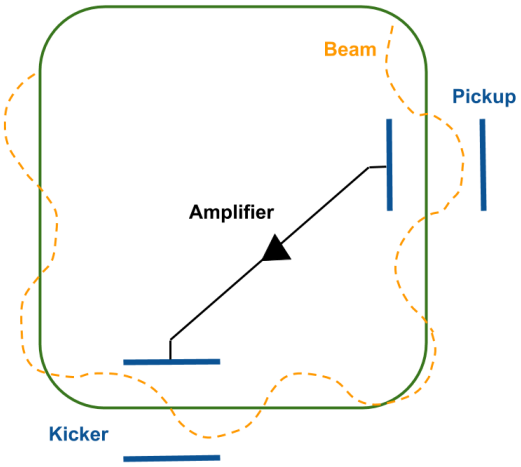

Figure 2.8. Model of Stochastic Cooling.

Fig. 2.8 shows the main basic principle of stochastic cooling, where a pickup (array of electrodes within a vacuum tank) is used to identify the position of the particles. Then this signal is amplified and sent to the kicker, which corrects the motion of particles reducing its betatron oscillation using an electric field. This process is repeated many times to cool the beam. The pickup and the kicker are separated by a odd number of quarter betatron wavelengths λ in order to cancel any oscillation. In practice, the signal will overlap due to the large quantity of particles, but the perturbing effect (heating) is zero on average.

In the Accumulator, in the low dispersion sections, it is convenient to place the pickup system for betatron cooling, while in the high dispersion region the pickup system is suitable for momentum cooling. To determine the cooling time, consider N particles in the ring, the signal arriving at the kicker depends on W, which is the bandwidth of the cooling system

(up to 8 GHz). The cooling rate, which is the inverse of cooling time, is given by

$$\frac{1}{\tau} = \frac{W}{2N} \tag{2.1}$$

Here we have that the cooling time scales in proportion to the number of particles. Now, taking x as the offset to the test particle, the correction in the kicker is λx, where λ is related to the amplification of the system. The corrected position received from the kicker [20] is

$$\Delta x = -\lambda x - \sum \lambda x_i \tag{2.2}$$

where the second term of the right side refers to the other particles excluding the test particle. The average sample error

$$\langle x \rangle_s = \frac{1}{N_s} \sum x_i \tag{2.3}$$

then Δx can be written as

$$\Delta x = -g \langle x \rangle_s \tag{2.4}$$

Here $g = N_s \lambda$ is called the gain. This shows how the cooling system applies a correcting kick by measurement $\langle x \rangle_s$. Another important parameter considered in the cooling system is the mixing factor M, ($M \geq 1$, with $M = 1$ being the perfect mixing) which is related to the heating effect due to the other particles. The thermal noise factor, U=noise/signal, is related to the amplifier system. In terms of these variables, the stochastic cooling rate [18] can be calculated using equation 2.5. If g<1, and $g = 1/(M + U)$ is the optimum system gain to get fastest cooling. However, the maximum cooling rate (W/N) is obtained if the gain is $g = 1$, zero noise $U = 0$, and perfect mixing $M = 1$.

$$\frac{1}{\tau} = \frac{W}{2N}(2g - g^2(M + U)) \tag{2.5}$$

An optimum gain can be determined in order to have more cooling and less heating. This is

shown in Fig. 2.9, where the cooling effect is directly proportional to the gain while the heating effect is corresponding to g^2. There the optimum gain is the point where the difference between the cooling rate and the heating rate is greatest. Stochastic cooling is applied in the

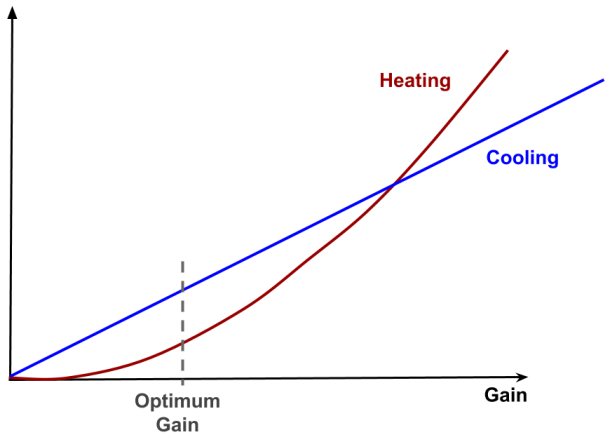

Figure 2.9. Cooling and heating effects in terms of the system gain [18].

Debuncher (in addition to Bunch Rotation) and accumulator rings. In the Debuncher the beam size is reduced by decreasing the transverse emittance (RMS Normalized) from about 330 to 30 μm. The antiprotons are next sent to the Accumulator ring. There, additional stochastic cooling is used, where the transverse emittance (RMS Normalized) is reduced to 15 μm, together with RF manipulations to accumulate 25×10^{10} $\bar{p}$/h. This amount is transferred to the Recycler every 60 minutes.

2.4.3 Antiproton Stacking

To optimize the collection of antiprotons in the accumulator ring, a stacking process is carried out using stochastic cooling. This is shown in Fig. 2.10. The first antiproton group coming from the Debuncher ring is injected into the "Injection" orbit. Then this group is moved to the "Stack" region by decelerating the antiprotons using an RF system. 2.2 seconds later the next bunch is injected and the same procedure is repeated. After one hour all the bunches in the stack form a dense core and the extraction process takes place. Fig. 2.11

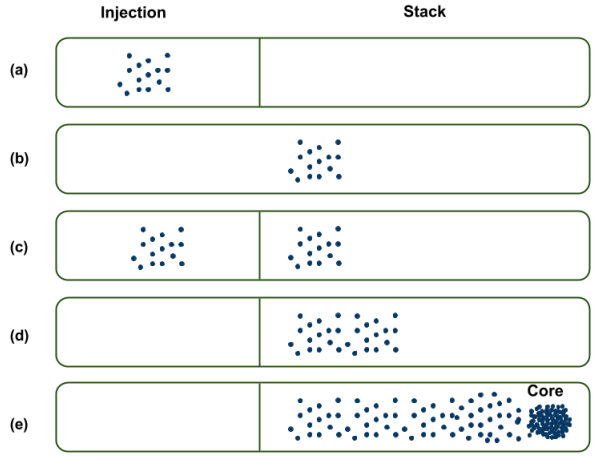

Figure 2.10. Stacking Process. (a) The first bunch is injected. (b) The bunch is moved to the stack region. (c) A second bunch in injected 2.2s later. (d) The second bunch is moved to the stack region. (e) After successive bunch injections a dense core is formed in the stack.

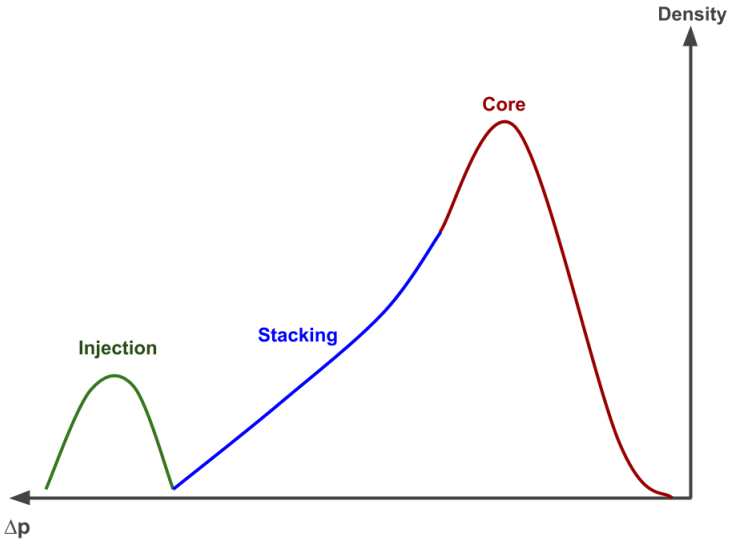

Figure 2.11. Antiprotons density distribution in the stacking process for the accumulator ring.

shows the density variation in each region of the stacking process as well as the momentum cooling, which is greater in the "core" region. Additional stochastic cooling, momentum and transverse, is done in this region.

In the Accumulator, the cooling system is distributed as is shown in Fig. 2.12. The pickups for stacktail cooling are located in the zone A60 together with the pickups for core 2-4 GHz momentum cooling, while in the zone A30 are found the kickers for these systems. Similarly, in the zone A10 we can find the pickups for core 2-4 GHz and core 4-8 GHz betatron cooling and in the zone A30 also the kicker for these systems. Finally, for core 4-8 GHz momentum cooling the pickups are in the zone A20 with their corresponding kickers located in the zone A50.

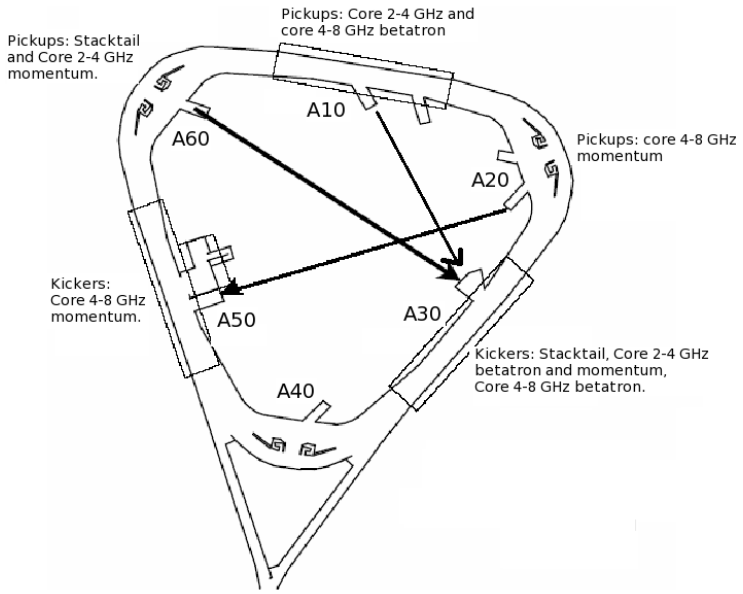

Figure 2.12. Accumulator Cooling Systems. Figure adapted from [12].

2.4.4 Electron Cooling

Electron cooling is based on the heat exchanger basis through the Coulomb interaction between a high energy spread (antiprotons or ions) beam and a low energy spread electron beam. See Fig. 2.13. In this cooling process the circulating electron beam has the same average speed as the antiproton beam, which transfers energy to the electron beam, reducing its energy spread. Maximum cooling is reached when the temperature of the two beams are equal. An important characteristic of the electron cooling process is the high efficiency for

low energy beams. The cooling time [20] is independent on the number of antiprotons, but is directly proportional to γ^2,

$$\tau = \frac{\gamma^2 M u^3}{4\pi\eta m_e Z^2 r_e^2 c^4 \rho_L L_C} \tag{2.6}$$

where M is the ion mass, u the velocity of the ion, η=cooling section length/ring circumference, m_e the electron mass, Z the ion charge number, c the speed of light, ρ_L the electron beam density, and L_C is a constant factor (Coulomb Logarithm) for the cooler, on the order of 10.

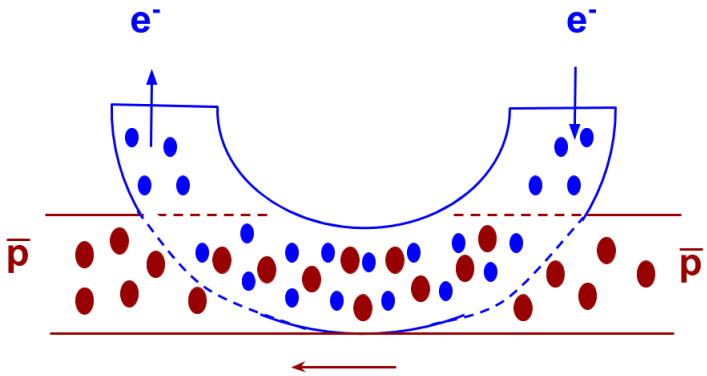

Figure 2.13. Principle of electron cooling. The high energy spread of the antiprotons is reduced when they are injected into a cooling section to interact with electrons with low energy spread.

In the Recycler ring the antiprotons are initially cooled using stochastic cooling. The antiproton and electron speeds must be close for electron cooling to work. Electron cooling follows stochastic cooling. Electron cooling was implemented at Fermilab in 2005. The cooling section is 20 m long inside the Recycler, and there a 4.3 MeV electron beam is used to cool the 8.9 GeV/c antiprotons transversely and longitudinally. The Recycler accumulated about 400×10^{10} antiprotons (with a 200 h lifetime) thanks to the use of electron cooling, which contributed to the overall Tevatron luminosity improvement by a factor of 25%.

2.5 Beam Parameters in Particle Accelerators

In a particle accelerator, the energy and the luminosity are the most important parameters. Higher masses can be produced if the collision energy is greater. The luminosity is defined as the number of particles per unit of area and time in a collision. Its units are usually expressed in $\mathrm{cm}^{-2}\ \mathrm{s}^{-1}$. The luminosity (equation 2.7) depends on the revolution frequency f_0, the number of bunches per beam N_B, the number of particles per bunch N_1 (beam 1), N_2(beam 2), the beam sizes σ_x and σ_y.

$$\mathcal{L} = \frac{f_0 N_B N_1 N_2}{4\pi\sigma_x\sigma_y} \tag{2.7}$$

The beam size can be expressed in terms of the emittance ε, and the β function. The parameter emittance refers to the beam quality, and is related to the beam size and the area of the phase space ellipse (u, u'). In Fig. 2.14, we show the phase space of a beam of area $\pi\varepsilon_{x,y}$. It is common to use the term normalized emittance ($\varepsilon_{N(x,y)}$), which is equal to the geometrical emittance ($\varepsilon_{x,y}$) multiplied by the relativistic parameter $\beta\,\gamma$. The parameter $\beta_{x,y}$ is the optical beta function. β^* is the betatron function at the interaction point. The beam size $\sigma_{x,y}$ can be calculated using the equation 2.8, where $\varepsilon_{N(x,y)}$ is the normalized transverse emittance, β_{rel}=p/E and γ=E/m is the Lorentz gamma factor.

$$\sigma_{x,y} = \sqrt{\frac{\beta\varepsilon_{N(x,y)}}{\beta_{rel}\,\gamma}} \tag{2.8}$$

In terms of these parameters, equation 2.7 for the luminosity [21] can be written as:

$$\mathcal{L} = \frac{\gamma f_0 N_B N_1 N_2}{4\pi\varepsilon_{N(x,y)}\beta^*} \tag{2.9}$$

Considering that the beam is a group of charged particles, when two beam collide, the electromagnetic fields generated by each beam affects the other beam, producing a defocusing force in the transverse direction. This force makes the particles experience a tune shift. The

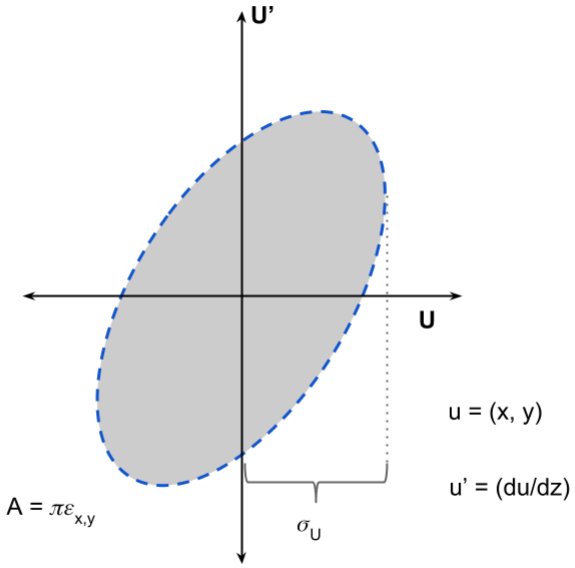

Figure 2.14. Phase space of a beam with the form of an ellipse. The coordinate u represents the position x or y.

number of betatron oscillations per turn is called *tune*. The beam-beam tune shift per collision is given by,

$$\xi = \frac{N r_0}{4\pi\varepsilon_N} \tag{2.10}$$

Here, N is the number of particles in the bunch, r_0 is the classical radius of the particle, and ε_N the normalized emittance. For example, the beam-beam tune shift for the LHC, with $N = 11.5 \times 10^{10}$ particles/bunch, the classical radius of proton $r_0 = 1.53 \times 10^{-18}$ m and the normalized emittance $\varepsilon = 3.75$ μm-rad, is $\xi = 0.003$. In Table 2.1 some luminosity and beam parameters for the Tevatron [22] and LHC are shown.

Also, an important parameter that can be calculated using the luminosity is the event rate of a collider,

$$R = \sigma\mathcal{L} \tag{2.11}$$

where σ is the corresponding total cross section. For example, for the LHC the total cross

section at E_{cm} = 14 TeV is about 110 mb. Thus, with L = $10^{34}\,cm^{-2}s^{-1}$ the event rate is 11 $\times\ 10^8\,s^{-1}$.

Table 2.1. Parameter list for Tevatron and LHC Colliders.

Collider Parameters	**Tevatron**	**LHC**	**Unit**
Luminosity ($\mathcal{L}$)	3.4 x 10^{32}	1.0 x 10^{34}	$cm^{-2}s^{-1}$
Energy Center of Mass (E_{cm})	1.96	14	TeV
Circumference (C)	6.28	27	km
Collision Frequency (f)	0.048	40	MHz
Lorentz Gamma Factor (γ)	1044	7460	
Number of Bunches (N_B)	36	2808	
Number of Protons/Bunch (N_p)	29 x 10^{10}	11.5 x 10^{10}	
Number of Antiprotons/Bunch (N_a)	8 x 10^{10}		
Normalized RMS Transverse Emittance (ε_N)	2.25	3.75	μm
Betatron Function at IP (β^*)	0.28	0.55	m
Beam Size at IP (σ)	33	16.6	μm

2.6 Synchrotron Radiation

Relativistic charged particles moving along a curved trajectory emit synchrotron radiation due to the transverse acceleration. The power emitted per particle is given by the equation [23],

$$P = \frac{c}{6\pi\epsilon_0} q^2 \frac{(\beta\gamma)^4}{\rho R} \tag{2.12}$$

where $\epsilon_0 = 8.85 \times 10^{-12}$ F/m, $q = 1.6 \times 10^{-19}$ C, ρ is the curvature or bend radius, which can be calculated using equation 2.17 (next section), and R is the ring radius.

Now, the energy loss per turn (per proton), is

$$U_0(keV) = 7.6 \frac{E[TeV]^4}{\rho[m]} \tag{2.13}$$

where E is the particle energy. Damping originates in lost energy in synchrotron radiation, which decreases particle momentum in the direction of its motion. Faster particles lose more energy. The longitudinal damping time, the time for a particle of energy E to radiate that

energy, is given by,

$$\tau_\epsilon = \frac{2E_0T_0}{J_\epsilon U_0} \tag{2.14}$$

where E_0 is the particle's energy, T_0 the orbit period (2πR/c), J_ϵ the damping partition number (2 for J_ϵ, 1 for J_x and J_y) and U_0 the energy loss per turn [24]. For colliders it is more usual to use the term "longitudinal emittance damping time", which is half of the longitudinal amplitude damping time. In Table 2.2 we show some parameters together with the longitudinal emittance damping time calculations for the Tevatron and LHC.

Table 2.2. Longitudinal emittance damping time for Tevatron and LHC Colliders.

Collider	$\mathbf{E}_{beam}$**(TeV)**	**B (T)**	ρ **(km)**	$\mathbf{U}_0$ **(keV)**	$\mathbf{T}_0$**(s)**	τ_ϵ **(h)**
Tevatron	0.98	4.2	0.754	0.0095	2.1 x 10^{-5}	305
LHC	7	8.3	2.80	6.7	9.1 x 10^{-5}	13

2.7 Magnetic Devices in Particle Accelerators

Superconducting magnets are used to transport and control the size of the particle beam in an accelerator. The magnets perform no linear acceleration, where Radio Frequency (RF) cavities are used instead.

2.7.1 Magnetic Dipoles

Among the magnet categories used in accelerators is the dipole, which is composed of a north and south pole separated by a distance producing a constant magnetic field inside as is shown in Fig. 2.15. A magnetic dipole is used to bend particles and produce dispersion. Mathematically the dispersion $D(s)$ is defined as

$$D(s) = \frac{\Delta x(s)}{\Delta p} p \tag{2.15}$$

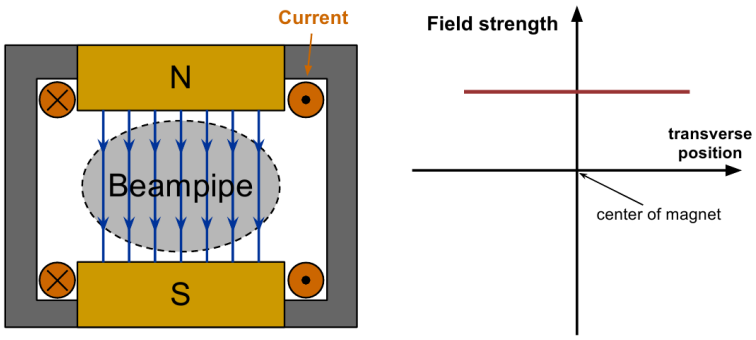

Figure 2.15. Magnetic Dipole. Source: [25].

where $\Delta x(s)$ is the displacement due to the momentum spread, Δp the momentum acceptance and p the central particle momentum. A dipole spreads the particles according to their momentum, thus particles with higher momentum will be have a smaller deflection than particles with low momentum when passing though a dipole as is shown in Fig. 2.16. From the magnetic part of the Lorentz force $F = q(v \times B)$, the bending radius ρ of the charged particle trajectory is given by,

$$\rho = \frac{p}{qB} \tag{2.16}$$

or in a more convenient form,

$$\rho[m] = \frac{p[GeV/c]}{0.3B[T]} \tag{2.17}$$

Now, with the magnetic field in the y direction and the particles moving along the z axis, the deflection angle $\Delta\theta \simeq \Delta p/p$, where Δp is the transverse momentum variation. This can be written as,

$$\Delta\theta = \frac{\Delta p \Delta t}{p \Delta t \Delta z}\Delta z = \frac{1}{pv}F dz \tag{2.18}$$

Integrating the previous expression in terms of the dipole length l,

$$\theta = \frac{Fl}{pv} = \frac{qBl}{p} \tag{2.19}$$

where the force $F = qvB$ was written in terms of the magnetic field, with B perpendicular to v. This expression can be expressed in a more appropriate form by multiplying it by c (the speed of light) and using electron-volts units for p to cancel the q term. Then we have finally the expression,

$$\theta_x[rad] = 0.3\frac{B[T]l[m]}{p[GeV/c]} \tag{2.20}$$

where the term 0.3 comes from the ratio between the speed of light value and the equivalence of 1 GeV to 10^9 eV.

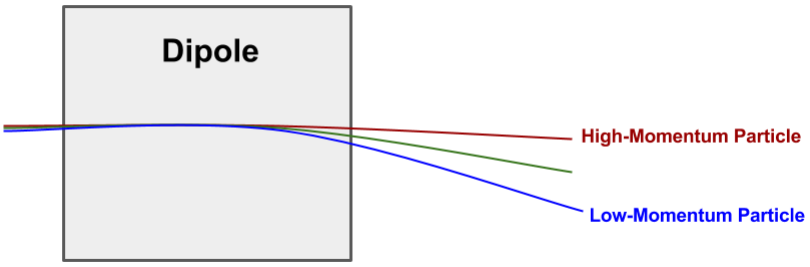

Figure 2.16. A Dipole bends particles according to their momentum.

2.7.2 Magnetic Quadrupoles

Another very important magnet used in particle accelerator is the quadrupole. A magnetic quadrupole, Fig. 2.17, consists of 4 magnets where the magnetic field grows in the radial direction,

$$B_z = -G \cdot x \qquad B_x = -G \cdot z \tag{2.21}$$

where G is the quadrupole gradient. Its units are T/m. Another important parameter for a quadrupole is the magnetic strength k given by,

$$k[m^{-2}] = 0.3\frac{G[T/m]}{p[GeV/c]} \tag{2.22}$$

the quadrupole focal length f is related with k and the quadrupole length l by,

$$f = \frac{1}{kl} \tag{2.23}$$

Generally, when $f >> l$ the quadrupole can be considered as a thin lens. Quadrupoles

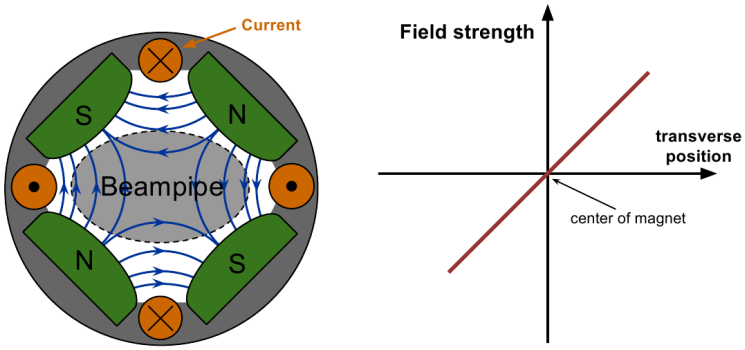

Figure 2.17. Magnetic quadrupole. Source: [25]. The magnetic field is proportional to the radial direction and is zero at the center.

have the characteristic of focusing in one plane and defocusing in the other. A focusing quadrupole focuses in the horizontal plane and a defocusing quadrupole focuses in the vertical plane. Fig. 2.18 shows these types of quadrupoles. To convert a focusing quadrupole

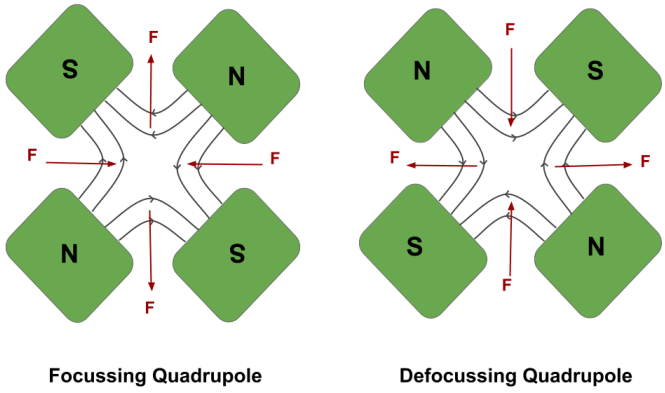

Figure 2.18. Magnetic focusing and defocusing quadrupole.

into a defocusing quadrupole and vice versa it is only necessary to rotate it 90 degrees. A quadrupole system provides the final focusing of the particle beams before collision by alternating focusing and defocusing. A FODO cell as is shown in Fig. 2.19 can be used to transport the beam. FODO refers to focus, drift, defocus, drift.

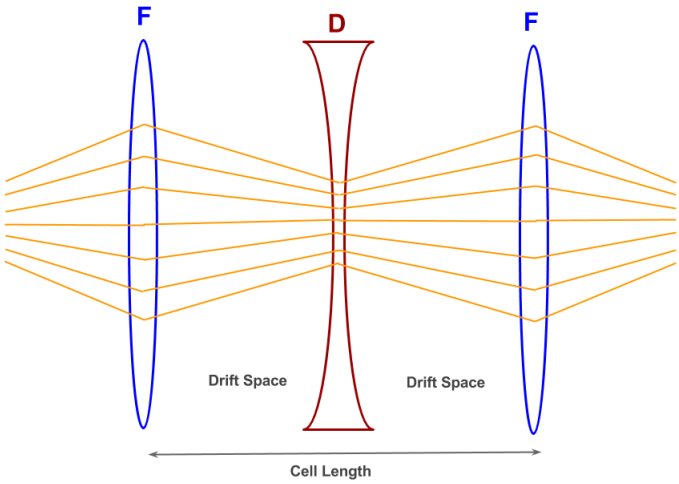

Figure 2.19. Quadrupole FODO Cell. A focusing (F) and defocusing (D) quadrupole separated by a drift space.

Quadrupoles also produce the aberration chromaticity with the quadrupole focal length depending on the momentum. To correct or control this chromaticity one often uses sextupoles, which allow stronger focusing of higher momentum particles.

2.7.2.1 Inner Quadrupole System for the Interaction Regions (IP)

In a particle collider, a quadrupole triplet system provides the final focusing of the particle beam to bring them to a collision point. A basic configuration is shown in Fig. 2.20. A symmetric combination of focusing and defocusing quadrupoles is placed in each side to provide the collision or interaction point, IP. The focal length of the triplet is the distance from the center of the quadrupole triplet system to the IP,

$$L_f = L^* + l_1 + a_1 + \frac{l_2}{2} \tag{2.24}$$

where L^* is the distance from the interaction point to the quadrupole Q1. Fig. 2.21 shows

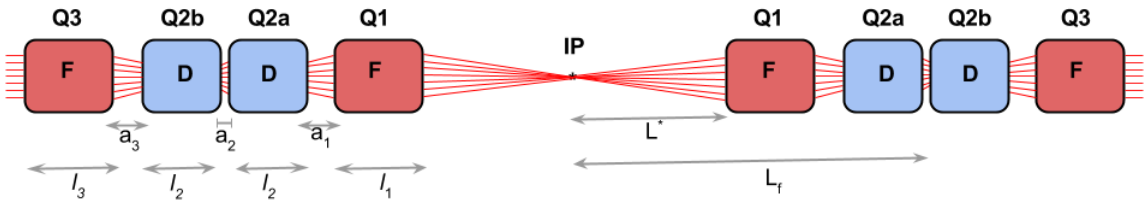

Figure 2.20. Inner quadrupole system to provide the final focusing for the collision of the particle beams.

a scheme of the inner quadrupole system corresponding to the interaction region of the LHC, such as the IP where the CMS detector is located. These quadrupoles have a field gradient of 205 T/m and aperture diameter of 70 mm. Similarly in Fig. 2.22 a scheme for

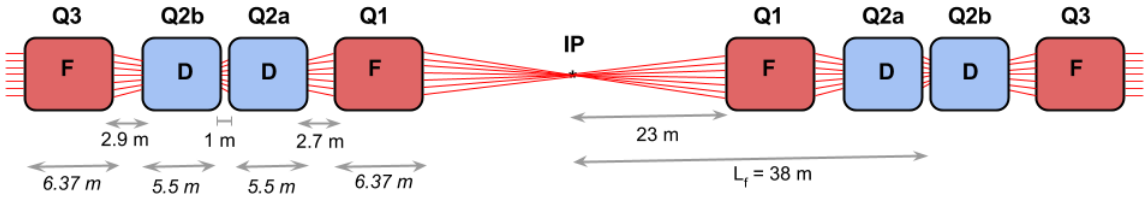

Figure 2.21. Inner triplet quadrupole scheme for CMS and ATLAS.

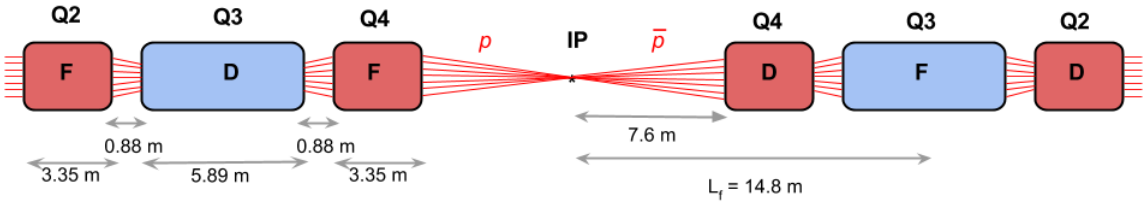

Figure 2.22. Inner triplet quadrupole scheme for the Tevatron (Fermilab).

the Tevatron inner quadrupole system is shown, which has a field gradient of 141 T/m and aperture diameter of 88.9 mm. There the quadrupoles are smaller in length, as well as a smaller IP distance with respect to the first quadrupole (Q4).

2.7.2.2 Quadrupole Matrix Formalism

The differential equation that describe the particle trajectory in quadrupoles has the form

$$u'' + K(s)u = 0 \tag{2.25}$$

where u can be either the position x or y, and s is the longitudinal position. For the plane, with bending, $K = -k + 1/\rho^2$, where ρ is the bending radius and k the quadrupole strength. For the plane with no bending, $K = k$. In beam dynamics, the transfer matrix M describes the transformation between the position u and angle u' in one point with respect to another initial point (u_0, u'_0) as is shown in Fig. 2.23 for the coordinate x.

$$\begin{pmatrix} u \\ u' \end{pmatrix} = M \begin{pmatrix} u_0 \\ u'_0 \end{pmatrix}$$

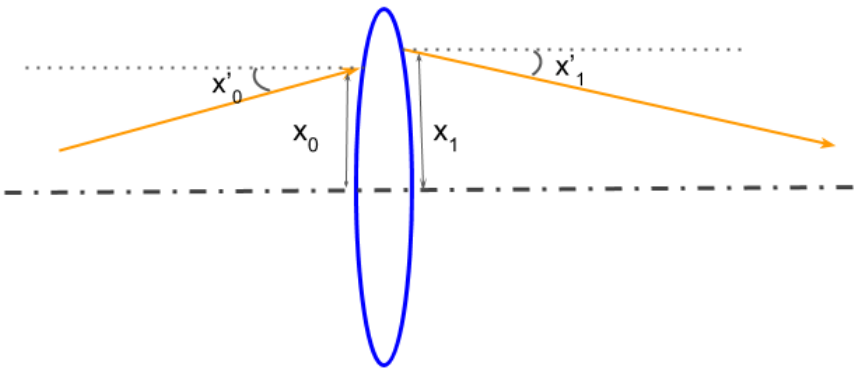

Figure 2.23. Initial vector coordinates (x_0, x'_0) entering a lens and final vector coordinates (x_1, x'_1) leaving the lens.

For a focusing quadrupole the transfer matrix M is written as

$$M_{QF} = \begin{pmatrix} cos(\sqrt{K}l) & \frac{1}{\sqrt{K}} sin(\sqrt{K}l) \\ -\sqrt{K} sin(\sqrt{K}l) & cos(\sqrt{K}l) \end{pmatrix}$$

where l is the quadrupole length. For a defocusing quadrupole the transfer matrix M is written as

$$M_{QD} = \begin{pmatrix} cosh(\sqrt{K}l) & \frac{1}{\sqrt{K}}sinh(\sqrt{K}l) \\ \sqrt{K}sinh(\sqrt{K}l) & cosh(\sqrt{K}l) \end{pmatrix}$$

Now, for a drift space the matrix M is

$$M_{Drift} = \begin{pmatrix} 1 & s \\ 0 & 1 \end{pmatrix}$$

where s is the length of the drift space.

Now, in thin lens approximation ($l = 0$),the transfer matrices are:

$$M_{QF} = \begin{pmatrix} 1 & 0 \\ -\frac{1}{f} & 1 \end{pmatrix} \qquad M_{QD} = \begin{pmatrix} 1 & 0 \\ \frac{1}{f} & 1 \end{pmatrix} \qquad M_{Drift} = \begin{pmatrix} 1 & s \\ 0 & 1 \end{pmatrix}$$

In the case that focal length of the focusing and defocusing quadrupoles are the same f, we have that for a FODO cell (Fig. 2.19) the transfer Matrix is given by,

$$M_{FODO} = \begin{pmatrix} 1 & 0 \\ -1/f & 1 \end{pmatrix} \times \begin{pmatrix} 1 & s \\ 0 & 1 \end{pmatrix} \times \begin{pmatrix} 1 & 0 \\ 1/f & 1 \end{pmatrix} \times \begin{pmatrix} 1 & s \\ 0 & 1 \end{pmatrix} = \begin{pmatrix} 1+\frac{s}{f} & 2s+\frac{s^2}{f} \\ \frac{-s}{f^2} & 1-\frac{s}{f}-\frac{s^2}{f^2} \end{pmatrix}$$

which is a multiplication of the transfer matrix of each element of the FODO cell. The stability condition (periodic motion) for a FODO is related with the trace of this matrix,

$$|Tr(M_{FODO})| < 2 \tag{2.26}$$

From this condition we can infer that the drift space s should be less than $2f$.

2.7.3 Lithium Lens

The most important characteristic of a lithium lens is the ability to focus in both transverse planes at the same time. Lithium is chosen because it is the least dense conductor, minimizing particle losses and multiple scattering. The lithium lens is basically an electromagnetic lens, in which a uniform axial current I flows though a solid lithium cylinder along its $\hat{z}$ axis generating a magnetic field $B(r)$ whose strength is directly proportional to the radial coordinate r, and whose direction follows concentric rings about the conductor in the $\hat{\phi}$ direction,

$$B(r) = \frac{\mu_0 I r}{2\pi R^2} = Gr \tag{2.27}$$

where G is the gradient field [T/m] of the lens. By the Lorentz force the field focuses particles to the center at $r = 0$. Fig. 2.24 shows this characteristic. At the Tevatron 120 GeV protons

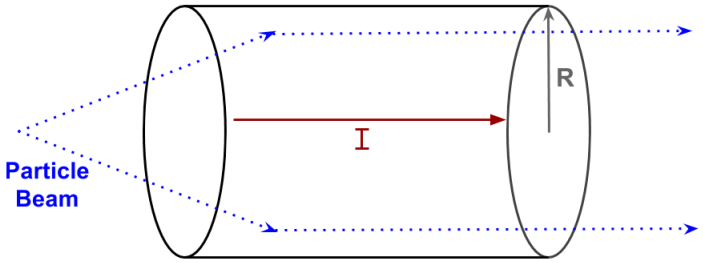

Figure 2.24. A lithium lens collecting particles and orientating them horizontally.

hit a small spot on a Nickel target. The Lithium Lens collected the antiprotons and the rest of the particles produced by the proton beam hitting the target. The focal length can be calculated using the equations 2.22 and 2.23 to obtain,

$$f[m] = \frac{p[GeV/c]}{0.3G[T/m]l[m]} \tag{2.28}$$

Now, the acceptance angle of the lens for the particles collected is given by,

$$\alpha[rad] = \frac{R}{f} \tag{2.29}$$

2.7.4 Beam Separation Devices

Beam separation should be made with minimum beam loss and disruption of emittance. Some specialized devices are used for this purpose. Among them are the electrostatic and magnetic septa. An electrostatic septum (Fig. 2.25) is used to split a particle beam

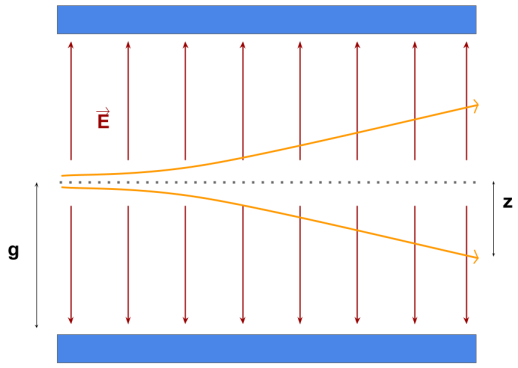

Figure 2.25. Beam deflection produced by an electric septa.

using electrostatic fields. Two electric fields of opposite direction are created by an array of grounded wires placed in the center. Thus, when the particle beam goes though the septum, it is separated in opposite directions. If only a portion of the beam is required to be extracted, a modified electrostatic septum is used as is shown in Fig. 2.26. This consists of thin foils that forms a ground plane that separates two field regions between the electrode and the field free region for the circulating beam. The beam is divided into two parts, in which the part that passes in the field region is extracted. From the Lorentz force $F = qE$, and taking the electric field in relativistic form, the force is given by,

$$F_z = \frac{d}{dt}\gamma m v_z \tag{2.30}$$

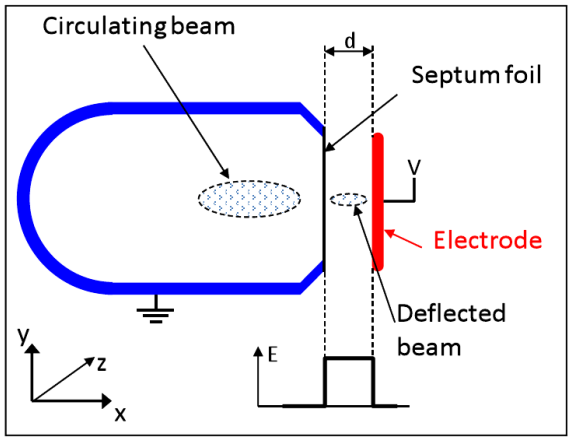

Figure 2.26. Electrostatic septum used to extract one part of the beam [26].

then,

$$\gamma m v_z = qEt \tag{2.31}$$

Now, solving for z,

$$z = \frac{qE}{2\gamma m} t^2 \tag{2.32}$$

using that $E = V/g$ (where V is the voltage and g the gap width) and $t = L/\beta c$, the vertical deflection z (Fig. 2.25) becomes,

$$z = \frac{qVL^2}{2\gamma g \beta^2 m_0} \tag{2.33}$$

In terms of the deflection angle [27], using small angle approximation $\theta = z/L$, we have that

$$\theta = \frac{VL}{2\gamma g \beta^2 m_0} \tag{2.34}$$

or

$$\theta[rad] = \frac{E[V/m]L[m]}{p[GeV/c] \cdot 10^9 \beta} \tag{2.35}$$

where the mass m_0 is in eV units. Among the typical technical values for an electrostatic septum are: range length $0.5 - 3.0\,m$, gap width $10 - 35\,\text{mm}$, septum thickness $\leq 100\,\text{mm}$, voltage up to 300 kV and electric field up to 10 MV/m [26].

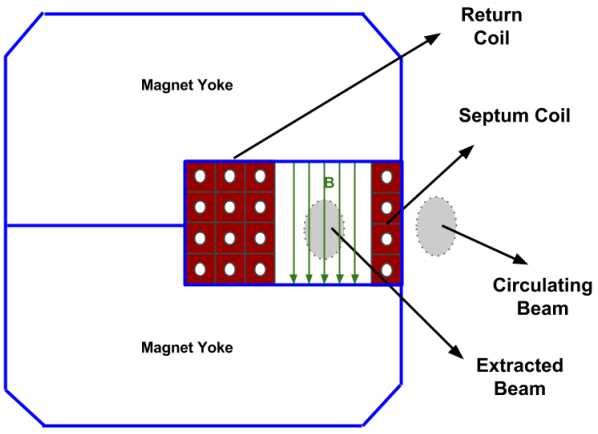

Figure 2.27. DC Magnetic Septum. The beam is separated into two parts, one enters in the field region B and the other part continues without change in the no field region.

Regarding magnetic septum, four types are widely used: Lambertson, Eddy current, pulsed, and DC magnetic septum. All of them have two regions or apertures, one region with a magnetic field produced by a dipole to deflect the beam, and the other a field free region. Fig. 2.27 shows the form of a DC magnetic septum. The current coils form the magnet to produce the magnetic field in the region where the beam is extracted. For this configuration, the magnetic field is given by,

$$B = \frac{\mu_0 I}{g} \tag{2.36}$$

where $\mu_0 = 4\pi \times 10^{-7}$ T$\cdot$ m/A is the vacuum permeability constant, I the current, and g is the gap width of the field region. Typical parameters values for this septum are: current between 0.5 and 4 kA, septum thickness from 6 to 20 mm, density current of 85 A/mm^2 and gap width of 25 to 60 mm [26].

2.8 Radio Frequency Cavity

The radio frequency (RF) cavity provides a source of Electromagnetic Field for beam acceleration, deceleration, bunching, and debunching. Basically, it is a region enclosed by

conducting walls (Fig. 2.28) where electromagnetic waves become resonant. These electro-

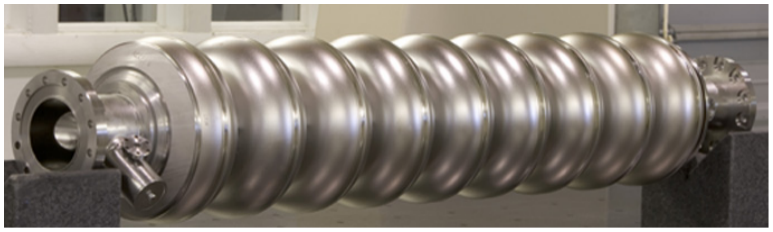

Figure 2.28. Radio Frequency Cavity. Source: [28].

magnetic fields are solutions to the wave equation,

$$(\nabla^2 - \frac{1}{c^2}\frac{\partial^2}{\partial t^2}) \begin{vmatrix} E \\ H \end{vmatrix} = 0 \tag{2.37}$$

where the boundary conditions or the fields at the surface are,

$$\hat{n} \times \vec{E} = 0, \qquad \hat{n} \cdot \vec{H} = 0 \tag{2.38}$$

where $\hat{n}$ is the normal vector in the surface. These boundary conditions allow no tangential

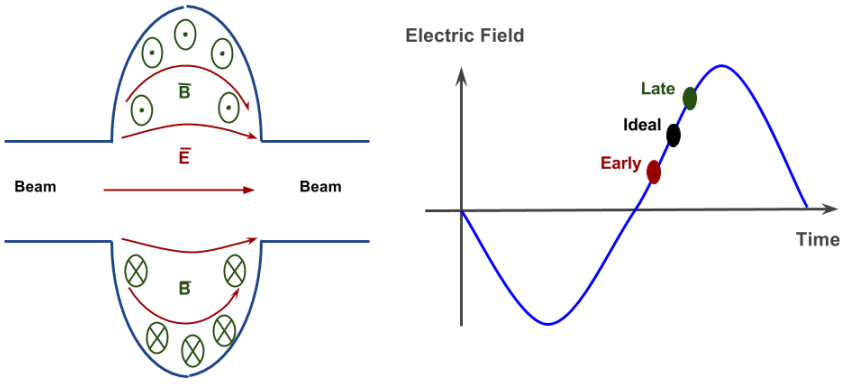

Figure 2.29. Electric and magnetic fields in a cavity. The electric field accelerates or decelerates the particles according to their arrival time.

electric field and no normal magnetic field at the walls of the cavity. An RF cavity provides a longitudinal electric field for acceleration. Thus, particles arriving earlier or later will be accelerated less o more so that they reach the reference energy of the ideal particle (see Fig. 2.29).

2.9 Beam Simulation Programs

There are various programs used in the analysis of particle beam and charged particle transport. They are designed to study the trajectory and behavior of these particles by using sophisticated tools to simulate components used in the particle accelerators.

One of those simulation programs is called G4beamline [29], which is used in this work. G4beamline is a particle tracking program, which models the behavior of particle beams, for example, when going through magnetic elements, RF cavities, target, etc. These elements are created using geometric forms, varieties of materials, and electromagnetic fields. A nice advantage of this simulation program is the output GUI environment, which shows all the elements used and the beam position. The geometry of the simulation can be verified through the visualization of the elements used in the simulation. For example, Fig. 2.30 shows a basic simulation of a beam going through two separated quadrupole magnets to focus the beam in a specific region. The data of interest can be stored to be plotted or

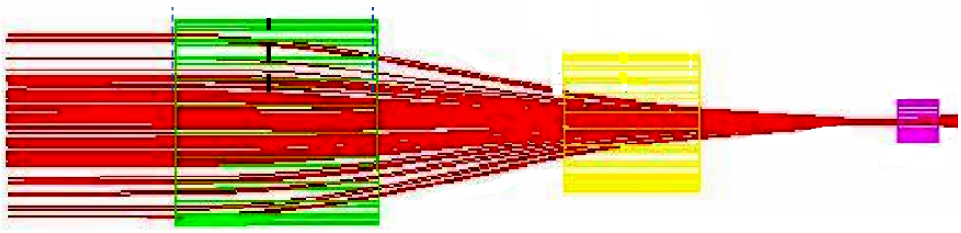

Figure 2.30. Simulation example in G4beamline. A flat beam goes through two quadrupole magnets which focus the beam in a specific region [30].

analyzed. These data include position, momentum components, beam sizes, etc., for a given position along the horizontal axis (z).

Another simulation program widely used is MAD-X [31] (Methodical Accelerator Design), which is also created to study beam dynamics in the design of accelerators. It also includes a large variety of elements to be simulated with the particle beam. Parameters such as beam size, beta values, dispersion, and other optics parameters are calculated. This program is able to study the behavior of beam size along its path through magnetic devices. For example, Fig. 2.31 shows the MAD-X output plot for the simulation of the CMS inner

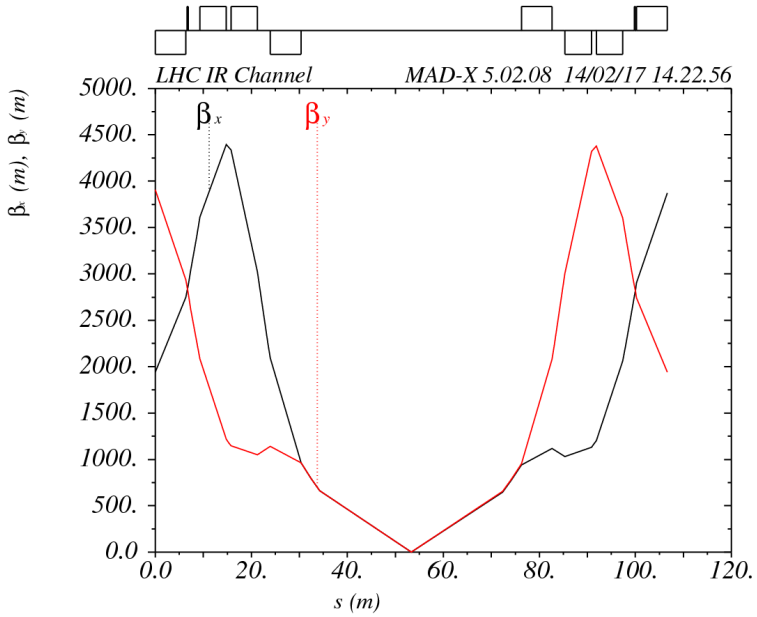

Figure 2.31. MAD-X Betatron Function Plot for the CMS Interaction Region.

quadrupole system (section 2.7.2.1). This plot shows the behavior of the components of the Beta function (which is related to the beam size) having the minimum value in the center, which represents the interaction point of the beams coming from opposite sides.

CHAPTER 3

3 PROTON-ANTIPROTON COLLIDER REMARKS

In this chapter we present some advantages that proton antiproton colliders have with respect to proton-proton colliders. Antiprotons have been used in the past at CERN [18, 32], Fermilab [33–35], and GSI Darmstadt [36, 37]. Also, the SSC (Superconducting Super Collider) Central Design Group [38] presented studies which examined the option of a $p\bar{p}$ collider ring at the SSC Super Collider in Texas.

A prime motivation has always been that production cross sections are often higher for producing high mass states in $p\bar{p}$ collisions. Many high mass states are created through $q\bar{q}$ processes. The accelerator can be operated at lower luminosity generating fewer events per beam crossing. Detectors operate with lower events rates where they function more effectively. These reasons all lead to the conclusion that there is decisive advantage in choosing a $p\bar{p}$ collider over pp colliders for many new high mass physics searches.

3.1 Cross Section for Higher Masses in pp and $\mathrm{p\bar{p}}$ Collisions

The rate of event production in a collider will be proportional to the collider's luminosity $\mathcal{L}$ and particle production cross section σ. The cross section σ is proportional to the probability of an event or reaction to be created in a collision. It has units of area (cm^2 and barns), where 1 barn (b) = 10^{-24} cm^2.

$$N_s = \mathcal{L} \cdot \sigma \tag{3.1}$$

The cross section for producing high mass events, indicating new physics, will be on the order of tens of femtobarns (10^{-15} b). At LHC energies, the inelastic cross section for

production of ordinary particles is of order 85 milibarns (10^{-3} b). At a luminosity $\mathcal{L} = 10^{34}$ cm^2 s^{-1} collider the rate of producing ordinary events is an overwhelming 85×10^{-27} cm^{-2} $\cdot$ 10^{34} cm^2 s^{-1} $= 85 \times 10^7$ s^{-1}. In a typical beam crossing time of 25 ns, typically 15-30 so-called pileup interactions will take place. This all leads to the importance of operating the accelerator at the minimum possible luminosity in order to achieve physics goals.

Fig. 3.1 shows the Higgs boson production cross sections in pp collisions in terms of the Higgs mass for different processes. There it can be seen the gluon fusion (gg) process dominates the lighter Higgs production in pp collisions up to the 1 TeV range. The $q\bar{q}$ part of the total cross section will be more important at higher masses, scaling with mass of the object M over center of mass collision energy $M/\sqrt{s}$. The cross section to produce high mass objects in $p\bar{p}$ collisions can be of order 10 times higher than it is for proton-proton collisions [39, 40].

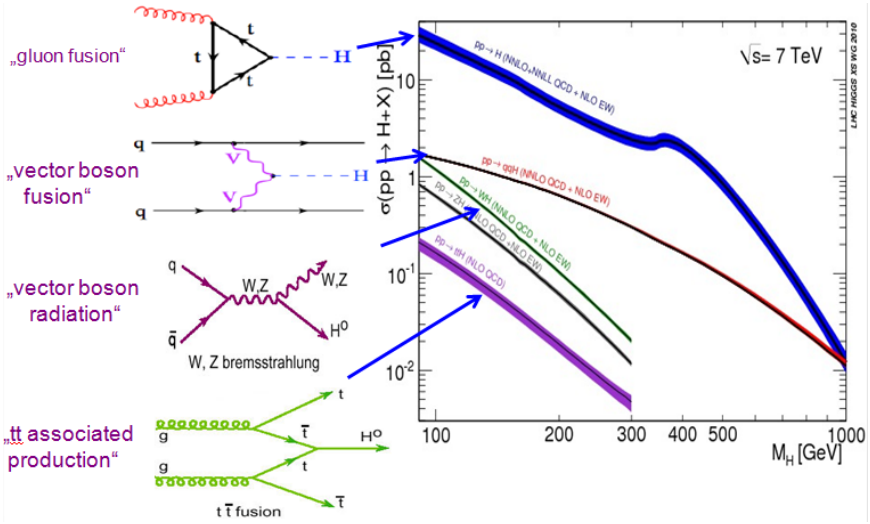

Figure 3.1. Cross sections in term of the mass for the Higgs production at E$_{cm}$ =7 TeV [41].

Because of the typically higher cross sections at proton anti-proton machines the $p\bar{p}$ collider can achieve sensitivity for high mass states while running at a lower luminosity $\mathcal{L}$. At pp colliders, running at higher luminosity, increases detector pileup and synchrotron radiation in the superconducting magnets and the vacuum system. This has adverse affects on the

accelerator design and operation of detector systems. As beam currents are increased more synchrotron radiation is produced in the superconducting magnets in the form of unwanted heat.

Several studies of cross sections are available for producing new physics in pp machines relating to the LHC and upgrade era. In some cases the physics generators for predicting these processes have not fully been verified in the 100 TeV region, as higher level perturbative Feynman diagrams become important. The cross section for $p\bar{p}$ collisions is greater than in pp collisions for higher masses, as in shown in Fig. 3.2. There it can be seen that the cross section for particles similar to the top quark production is greater in proton-antiproton collision than in proton-proton collision as mass increases.

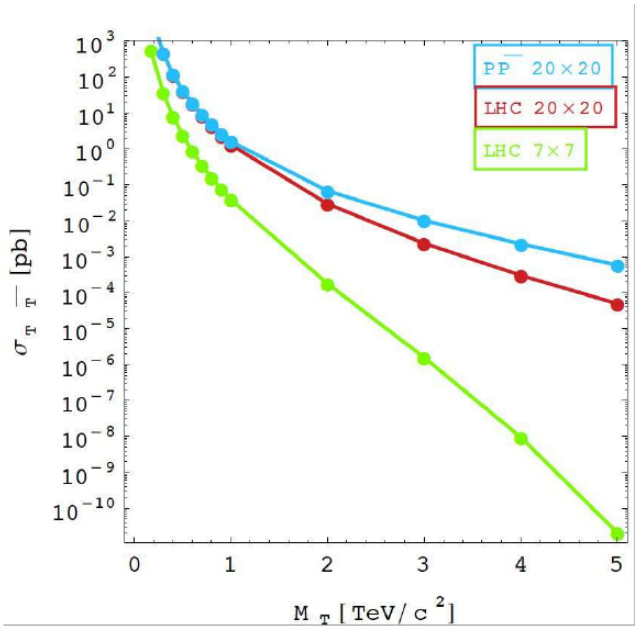

Figure 3.2. Top-like Anti-top-like Cross section production as a function of the mass using pp and $p\bar{p}$ collisions [39].

As fewer detailed calculations were available for guidance in the design of our 100 TeV $p\bar{p}$ collider, we proceeded with our own investigations. Several simulations program packages are available to generate hard events, showering, and hadronization (quarks and gluons). These Monte Carlo programs are used in high energy physics to study the properties

of the process in which the particles are generated by colliding two incoming particle beams. The processes for high mass states are produced as a function of their corresponding cross sections. We can compare the simulation results with existing real data from the experiments or future particle colliders. Some generators used in particle physics are hadronic event generators, in particular Pythia , Herwig, Isajet, and Sherpa. Other multipurpose parton level generators are Madgraph5 and Whizard. We use the generators Madgraph5 [42] and Pythia6 [43] which are currently very commonly used in particles physics.

MadGraph5 [42] is a multi-purpose matrix element generator program for High Energy Physics, written in Python, to simulate and generate events as particles decays and scatterings. It gives useful results as the four momentum vectors (p_x, p_y, p_z, E), cross sections, and all Feynman diagrams for the process generated. It also provides a variety of tools for manipulation and analysis. It generates a lhe (Les Houches Event) output file, which contains the process generated, information as to the number of events, the energy of each beam, the beam type (proton, antiproton, photon, etc.), particle masses, and other relevant parameters. Also it gives a complete list of all particles in the process as the momentum components (p_x, p_y, p_z), energy, and particle mass. This file is used to plot kinematic distributions as mass, momentum, angular variables, etc.

Pythia6 [43] is second event generator which is useful for hadronic processes in collisions involving proton-proton (pp), proton-antiproton ($p\bar{p}$), positron-electron (e^+e^-), electron-proton (e^-p) and muon-muon ($\mu^+\mu^-$) beam interactions. The latest version of the program is written in the C++ programing language, previous versions were written in Fortran. Pythia has built-in over 200 Standard Model (SM) and Beyond Standard Model (BSM) subprocesses.

Our new 100 TeV collider is designed to search for physics beyond the standard model (BSM). Several new particles are predicted by unified theories. We focused on the heavy W' boson, which is a massive version of the standard model W boson. This predicted boson is considered to have a mass at the TeV scale, and be produced through $q\bar{q}$ collision. Fig. 3.3

shows the Feynman diagram for W' production from $q\bar{q}$ and qq collision. There it can be seen that antiquarks for W' production can come directly from an antiproton rather than indirectly from gluon splitting in proton-proton collisions. The anti-quarks which are present in the $\bar{p}$ represent a significant advantage in using $p\bar{p}$ colliders.

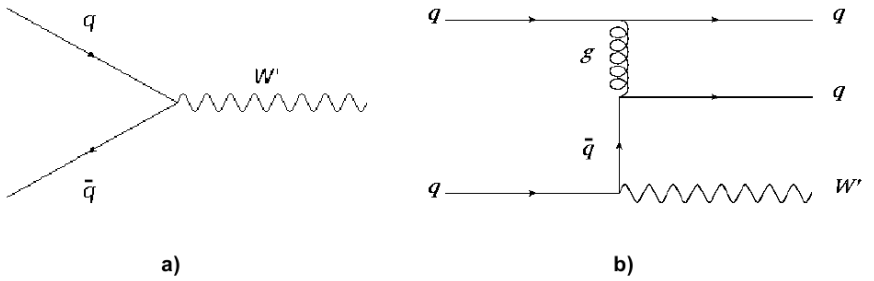

Figure 3.3. Feynman Diagrams for W' production from a) $q\bar{q}$ collision, b) qq collision.

We programmed the two event generators, Madgraph5 and Pythia6, to obtained the W' cross section for different W' masses, using proton-proton and proton-antiproton collisions with a center of mass energy of 100 TeV. These calculations are the first that we know of published with the Madgraph and Pythia generators for $p\bar{p}$ collisions.

The results, using Madgraph, are shown in Fig. 3.4. They show that the cross section for $p\bar{p}$ collisions is greater than in pp collisions for higher masses, as expected. See Fig. 3.2. As the W' mass increases the production cross section obtained with $p\bar{p}$ collisions grows as compared with pp collision, becoming about 10 times larger at 40 TeV/c^2.

The procedure was repeated using the Pythia event generator. The results are shown in Fig. 3.5. Again it can be noticed how the W' cross section is greater in $p\bar{p}$ collisions as the mass increases. The difference in absolute cross sections from those obtained with Madgraph and Pythia generators at higher masses is due to the difference in higher order Feynman amplitudes considered in each generator. However for masses less than 20 TeV/c^2 the cross section values are close in both programs.

Summarizing, the great advantage of having higher cross sections for W' and other high mass states is that it permits a 100 TeV collider with less detector pileup. Pileup

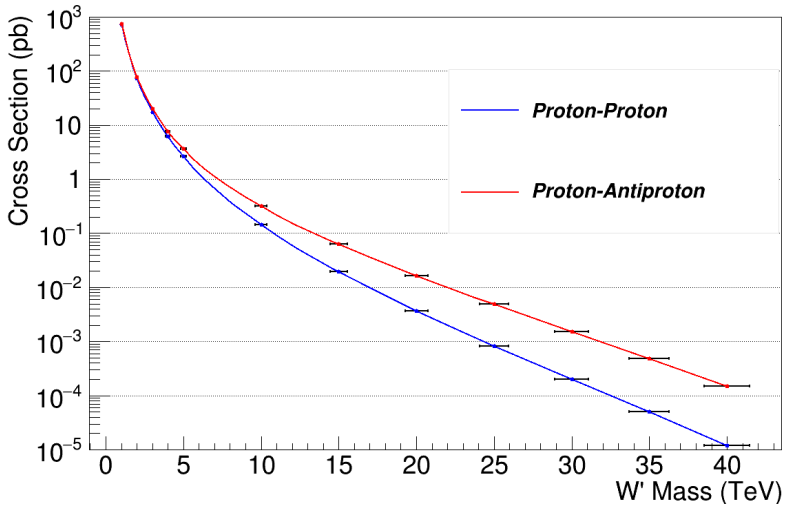

Figure 3.4. MadGraph results for W' Boson production cross section as a function of the mass using pp and $p\bar{p}$ collisions with a E_{cm} = 100 TeV.

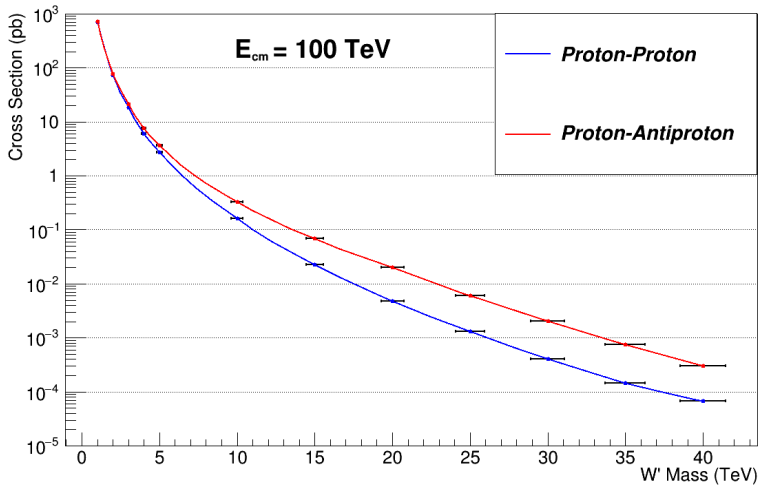

Figure 3.5. Pythia results for W' Boson production cross section as a function of the mass using pp and $p\bar{p}$ collisions with a E_{cm} = 100 TeV.

decreases as antiprotons are distributed into more bunches. There is a limit to this as the number of protons per bunch must stay constant to keep the luminosity constant, and synchrotron radiation rises with the number of protons. Next we consider the substantial advantages in running the accelerator at lower beam current with regard to lowering syn-

chrotron radiation levels.

3.2 Synchrotron Radiation in High Energy Colliders

As noted the higher cross sections particles production ($p\bar{p}$ collider) allow the collider to be run at lower beam currents and luminosities. Synchrotron radiation (SR) in the collider's superconducting magnets and vacuum system, can cause severe radiation damage to materials and cause unwanted heating.

We can estimate the power that is emitted due to Synchrotron Radiation. Equation 2.12 gives the power emitted per particle,

$$P = \frac{c}{6\pi\epsilon_0} q^2 \frac{(\beta\gamma)^4}{\rho R}$$

For example, at the LHC (E = 7 TeV, $\gamma = E/m = 7460$, $\rho = 2.8$ km, R = 4300 m) the SR power for a proton is P = 1.2×10^{-14} kW. Thus, for a proton beam, which consists of 2808 bunches and 1.15×10^{11} protons per bunch, the total SR radiated is 3.9 kW. Now, if the particle energy is increased, the SR power grows as $\gamma^4/\rho R$ creating a serious limitation to deal with in the design of new high energy (100 TeV) colliders [44]. Table 3.1 shows the parameters and the SR power calculations for a 100 km pp collider [45] and for the 270 km $p\bar{p}$ collider proposed is this work.

Table 3.1. Synchrotron Radiation (SR) for a 100 km pp and 270 km $p\bar{p}$ circumference colliders. γ = E/m = 53,300. 50 TeV beam energy.

	R m	B T	ρ m	Packing Fraction	SR/proton kW	Bunches /beam	Particles /bunch	SR/pipe kW	Beam Pipes	SR/meter W/m
pp	15,915	16	10,410	0.66	2.25×10^{-12}	10,600	10×10^{10}	2380	2	29
$p\bar{p}$	42,970	4.5	37,040	0.86	2.33×10^{-13}	10,800	$20/0.32\times10^{10}$	511	1	2.2

It is important to highlight that the SR Power per meter is 13 times lower for the 100 TeV $p\bar{p}$ compared with the pp collider, because higher production cross sections of

high p_T particles allow lower beam currents and because the tunnel circumference is larger. Furthermore, a $p\bar{p}$ collider only requires one ring instead of the two needed for a pp collider. The same magnets are shared by both beams because of their opposite charge, reducing costs. All reasons above are advantages of a high energy proton-antiproton collider.

CHAPTER 4

4 ANTIPROTON CAPTURE

In the design of a new $10^{34}\,\mathrm{cm^{-2}s^{-1}}$ high luminosity proton-antiproton collider increasing the number of available antiprotons is the crucial factor. The Fermilab Tevatron had a powerful antiproton source, which cooled about $40 \times 10^{10}\,\bar{\mathrm{p}}/\mathrm{h}$ in the Debuncher ring and $25 \times 10^{10}\,\bar{\mathrm{p}}/\mathrm{h}$ in the Accumulator ring. In the Tevatron's antiproton source the momentum was 8.9 GeV/c $\pm$ 2%, yielding a 2% momentum acceptance into the next cooling stage. A large number of antiprotons were rejected because of the low acceptance. This chapter presents the viability of being more efficient and collecting more antiprotons, rather than just producing more of them from a Fermilab -like target station. Our goal is to increase the momentum acceptance from 2% to 24%, with 12$\times$ more antiprotons collected.

4.1 Luminosity Requirements

As a starting point, we take as reference the Tevatron collider (TEV). We can estimate the needed increase in luminosity $\mathcal{L}$, equation 2.7, of the new 100 TeV collider by scaling from Tevatron parameters of: luminosity $\mathcal{L}_{TEV} = 3.4 \times 10^{32}\,\mathrm{cm^{-2}s^{-1}}$, energy $E_{TEV} = 0.96$ TeV, and circumference $\ell = 6.28$ km.

$$\mathcal{L} = \frac{E}{E_{TEV}} \times \frac{\ell_{TEV}}{\ell} \times \frac{\beta^*_{TEV}}{\beta^*} \times \mathcal{L}_{TEV}$$

$$\mathcal{L} = \frac{50\ \mathrm{TeV}}{0.98\ \mathrm{TeV}} \times \frac{6.28\ \mathrm{km}}{270\ \mathrm{km}} \times 2 \times 3.4 \times 10^{32}\,\mathrm{cm^{-2}s^{-1}}$$

$$\mathcal{L} = 8 \times 10^{32}\,\mathrm{cm^{-2}s^{-1}}$$

The β^* factor $\times 2$ comes from the reduction of $\beta^* = 28$ cm at the Tevatron to a $\beta^* = 14$ cm at the new collider. With basic dynamical changes in the new collider size and energy the luminosity is increased by a factor of 2.4 over the Tevatron. However, to achieve a luminosity of $10^{34}\,\mathrm{cm^{-2}s^{-1}}$, approximately 12$\times$ more bunches are needed.

The number of antiprotons available for the collisions is given by the event or burn rate, $\bar{p}_{burn\ rate}$, which depends on the total proton/antiproton cross section and the luminosity. At high center of mass (cm) energy ($E_{cm} \geq 200$ GeV) the total annihilation cross section is the same for pp and $p\bar{p}$ collisions [46]. For $E_{cm} = 100$ TeV, the total cross section is $\sigma = 153$ mbarn [47]. The antiproton burn rate will be $\bar{p}_{burn\ rate} = \sigma\mathcal{L} = 551 \times 10^{10}/h$.

The Fermilab Debuncher cooled a peak of 45×10^{10} $\bar{\mathrm{p}}$/h [48]. We then estimate that to keep up with the $\bar{p}_{burn\ rate}$, 12× more antiprotons are needed. At the Fermilab antiproton source a large number of antiprotons were rejected because of the modest momentum acceptance. We adopt a strategy of keeping the antiproton source fixed, and explore means of collecting more of $\bar{p}$'s, specifically around 8.9 GeV/c $\pm$ 24%. Providing a second Accumulator ring might improve the Accumulator ring stacking rate [49]. At Fermilab, the Accumulator stacked 62% of the Debuncher output.

4.2 Increase in Antiproton Momentum Acceptance

At the Fermilab antiproton target station $\bar{p}$'s were created by hitting an Inconel (a low expansion nickel-iron alloy) target with a 0.1 mm spot beam size of 120 GeV protons, with a optimum production of antiprotons with a momentum range from 8 to 13 GeV/c. The angular distribution of the produced antiprotons is gaussian shaped with sigma [50],

$$\sigma_\theta \approx \frac{1.1}{\gamma}\sqrt{\frac{m_\pi}{m_p}} \tag{4.1}$$

where m_π (139.6 MeV/c^2) is the pion mass, m_p (938.3 MeV/c^2) is the proton mass and γ is the relativistic boost factor (E/m) of the antiprotons. For example, for 8.9 GeV/c antiprotons the angular distribution has a sigma value of 45 mrad. The effective geometric emittance (phase space area) of the 8.9 GeV/c antiprotons exiting the target is 26 μm (247 μm rms normalized).

Now, with reference to the antiprotons momentum, Fig. 4.1 shows the momentum distribution for antiprotons created by a 120 GeV proton beam hitting a tungsten target

within a production angle of 60 mrad. This plot was reproduced taking as reference Figure 4 of the paper "Calculation of anti-Proton Yields for the Fermilab anti-Proton Source" [51], considering that Inconel and tungsten should give similar distributions. The plot follows a Landau distribution function (blue trace) in the important momentum range of 5 -18 GeV/c. Thus, the goal is to collect the antiprotons within an approximate momentum range of p = 11.0 GeV/c $\pm$ 24% or p = (11.0 $\pm$ 2.6)GeV/c, taking 11.0 GeV/c as the central momentum.

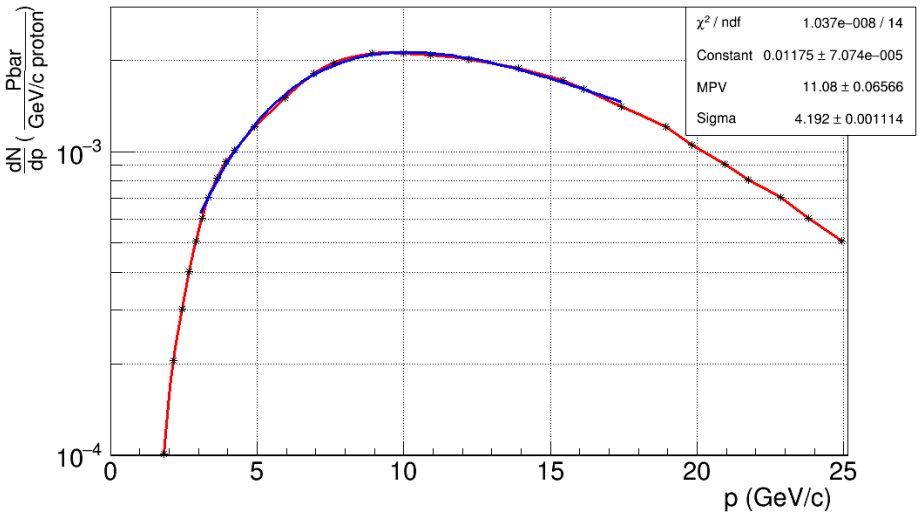

Figure 4.1. Momentum distribution of the antiprotons produced by a 120 GeV proton beam hitting a tungsten target [51].

In the Tevatron target station, the particles that emerged from the target were focused by a lithium lens. This was a solid cylinder of radius 1 cm and length 15 cm, in which an high 500 kA axial current produced a strong radial gradient of 1,000 T/m. The effective focal length was 20.0 cm. To increase the momentum acceptance of the antiprotons, a system of multiple lenses or a longer single lens might be necessary [52]. To go from 8.9 to 11.0 GeV/c the lithium lens is lengthened from 15 to 18.6 cm. The new focal length for the central momentum of 11 GeV/c is 20 cm. This is calculated using the equation 2.28 from Chapter 2.

To measure the effectiveness of the new lens, a G4beamline simulation was performed

by creating a beam with a Landau momentum distribution (11 GeV/c, σ = 4 GeV/c) (Fig. 4.1), a gaussian angular distribution $\theta\,(0,\,45\,mrad)$, a uniform azimuthal distribution $\phi = (0,\,2\pi)$, and momentum components

$$\mathrm{p_x} = \mathrm{p}\,\sin(\theta)\cos(\phi),\;\; \mathrm{p_y} = \mathrm{p}\,\sin(\theta)\sin(\phi),\;\; \mathrm{p_z} = \mathrm{p}\,\cos(\theta)$$

These parameters simulate the beam coming from the target. The purpose of the lithium lens is to reduce the transverse momentum, $\mathrm{p_t} = \sqrt{\mathrm{p_x^2} + \mathrm{p_y^2}}$, of the beam. Fig. 4.2 shows a divergent beam (p = 8.9 GeV/c $\pm\,2\%$) simulated in G4beamline, as if it was coming out of a target and passing through the lithium lens. The beam is oriented in the horizontal

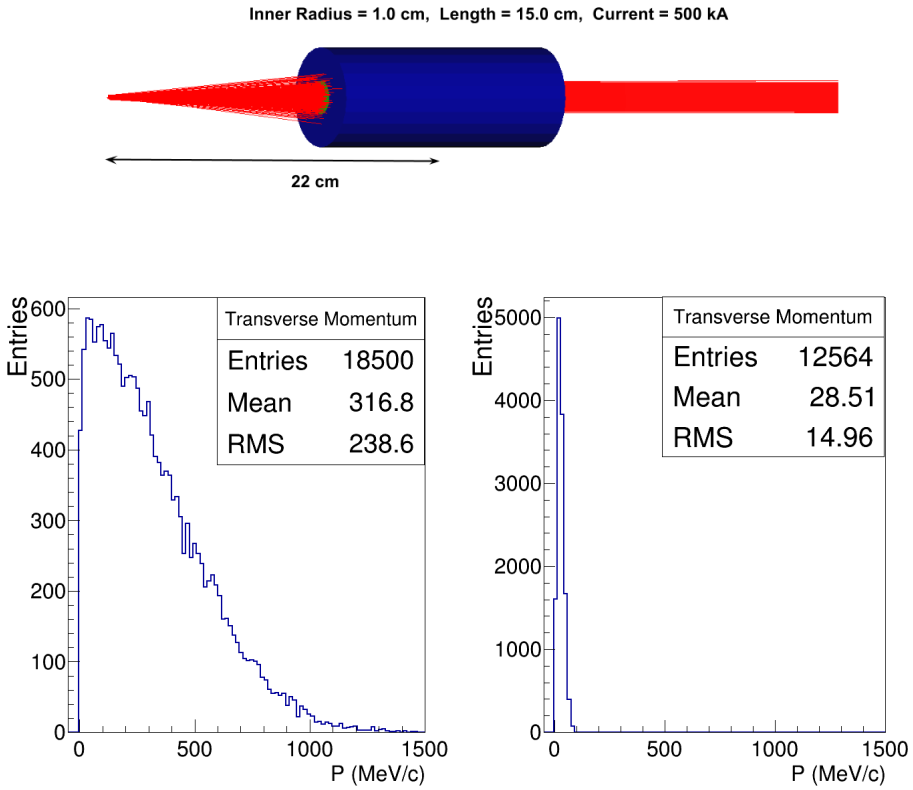

Figure 4.2. 8.9 GeV/c$\pm\,2\%$ antiproton beam simulation crossing a lithium lens. The plots show the transverse momentum distribution of the beam before entering (left plot) and in the output of the lithium lens (right plot).

direction. The transverse momentum of the beam before entering the lens, as well as the

transverse momentum distribution in the lens output is shown in the same figure. Taking as reference the mean transverse momentum value, p_t, this represents a 91% reduction. Similarly, a G4beamline simulation is performed, but using a beam with momentum p = 11 GeV/c $\pm$ 24% and crossing the lithium lens of 18.6 cm in length. The simulation is shown in Fig. 4.3 together with the initial and final transverse momentum distribution of the beam. The optimum position to be placed the lens from the "target" to its center was determined to be 22 cm. Here, the mean value is reduced by 89%. It can be noted that the 18.6 cm lens does a good job of reducing the transverse momentum of a beam with a large momentum spread.

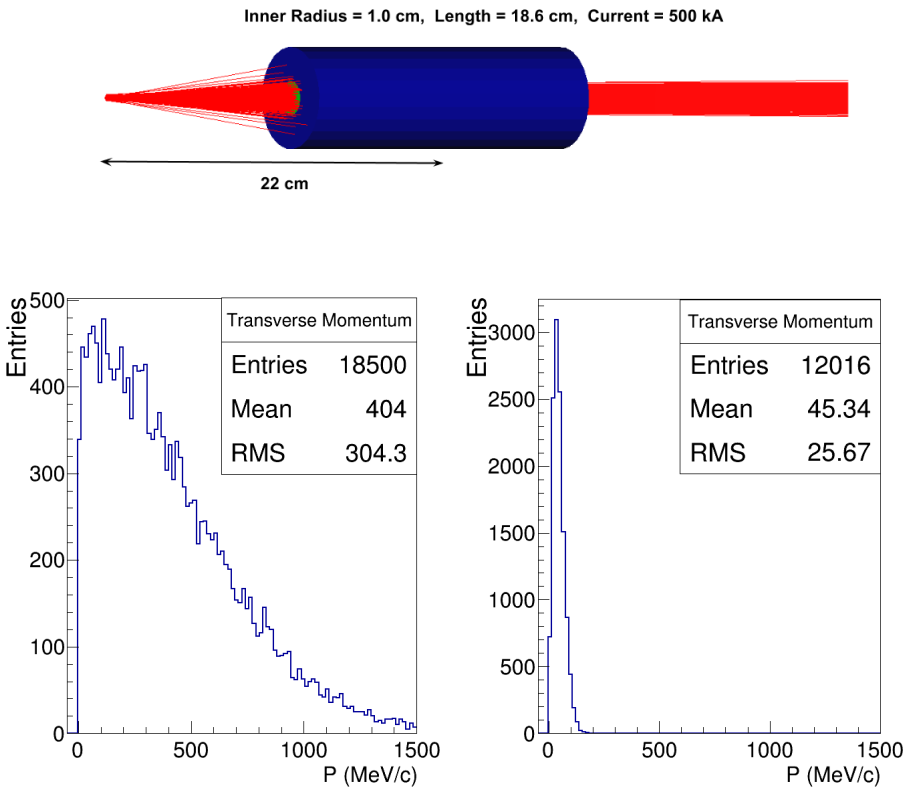

Figure 4.3. 11 GeV/c $\pm$ 24% antiproton beam simulation crossing a lithium lens in G4beamline. The plots show the transverse momentum distribution of the beam before entering (left plot) and in the output of the lithium lens (right plot).

In the lithium lens, the antiprotons experience scattering and absorption. The ab-

sorption causes loss and the scattering causes emittance growth. The deflection angle due to the Coulomb scattering [53] is given by,

$$\theta_0 = \frac{13.6\,\mathrm{MeV}}{\beta cp} z\sqrt{x/X_0}[1 + 0.038\ln(x/X_0)] \tag{4.2}$$

where $\beta = 1$, p = 11 GeV/c, z = 1 (charge number) for the incident antiprotons, x is the Li lens length (18.6 cm), and X_0 is the radiation length of the Li (15.5 cm). Substituting these values the scattering angle is 0.41 mrad. $\beta\gamma = p/m = 11.0/0.938 = 11.7$. Thus, the normalized emittance growth [50],

$$\Delta\epsilon_N = \beta\gamma R_{lens}\theta_0 = 48\,\mu m \tag{4.3}$$

The growth is small when added in quadrature to the initial normalized transverse beam emittance of 330 μm.

To separate the antiprotons from the others particles (p, n, π^+, etc), a pulsed dipole is located after the lithium lens and separates the particles according to charge. The negatively charged antiprotons are bent by 3° and the other particles are sent to a dump (graphite surrounded by steel) to be absorbed.

4.3 Antiproton Beam Separation and Transport

More antiprotons are needed, if luminosity is to be increased. To do this a large momentum spread beam is accepted and then quickly spread into a dozen beams with lower momentum spreads. This is simulated in G4beamline. The simulated antiproton beam coming from the Li lens is dispersed using a 1.5 m long dipole with magnetic field of -1.8 T. Fig. 4.4 shows the momentum vs x position for the initial beam and when the beam is dispersed. Here x(mm) represents the vertical coordinate in the G4beamline simulation. The particles with high momentum experience less deflection.

The dispersed beam can be divided by placing an electrostatic septum and two mag-

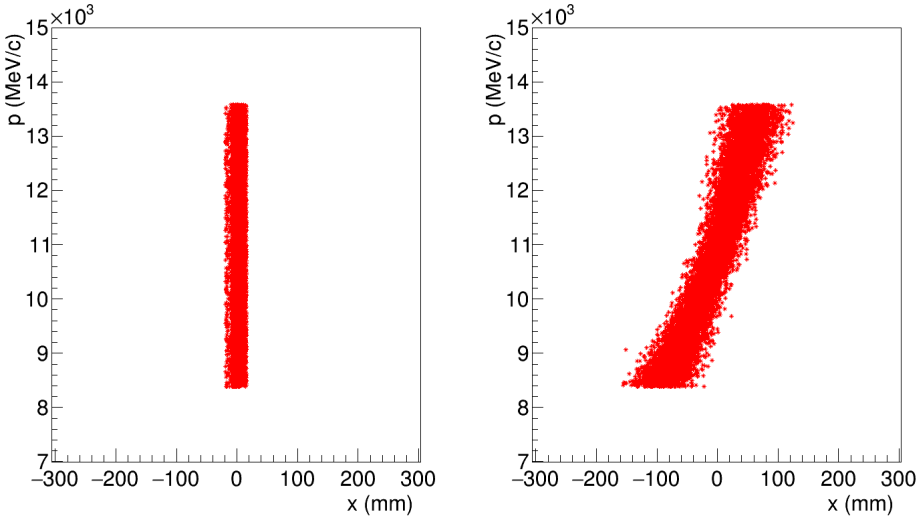

Figure 4.4. Momentum vs x position for the initial beam (left plot) and the dispersed beam (right plot).

netic septa to increase the separation. The electrostatic portion has a thin septum $\leq 100\,\mu m$ minimizing beam loss, and the magnetic one has a thin septum between 2-20 mm. The beam exiting from the electrostatic septum should have equal or greater deflection than the magnetic septum thickness to minimize any interaction with the material. Fig. 4.5 presents the

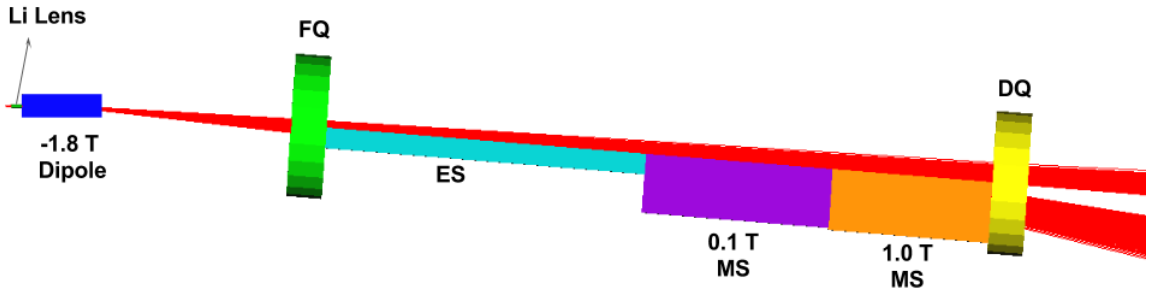

Figure 4.5. Configuration to divide the beam into two parts. An initial beam with momentum acceptance $p = 11.0$ GeV/c $\pm\, 24\%$ is collected by the Li lens and dispersed by a magnetic dipole to be then divided by a electrostatic septa ES and two magnetic dipoles MS.

basic cell to divide the initial dispersed beam into two:

- An initial beam with Landau function momentum distribution (11 GeV/c, 1.5 GeV/c)

enters the Li lens and then is spread by a -1.8 T dipole of 1.5 m in length.

- An electrostatic septum (ES) divides the beam, which is placed in such a way that half is deflected. The parameters used for the septa are: length = 6 m, Electric Field = ±1.0 MV/m, gap = 0.30 m and septum thickness = 0.2 mm.

- Next to the electrostatic septum a 0.1 T magnetic septum (MS), 3.5 m long, with septum thickness of 4.0 mm is placed to increase the beam separation. This magnet provides a deflection range of 27-44 mm into the momentum acceptance required.

- A 3.0 m long magnetic septum, 1.0 T, is placed next to the 0.1 T dipole to allow a greater separation between the divided beam. This provides a deflection range of 200-300 mm.

- To transport the beam a FODO cell (26.3 m) is used. This consists of a focusing quadrupole FQ, a drift space and a defocusing quadrupole DQ. The quadrupoles are 0.66 m in length, aperture radius of 1.0 m and field gradients of ± 2.0 T/m. This FODO length is chosen to be equal to the AP2 transport line in the Tevatron. Table 4.1 presents the parameters of the cell which divides the initial beam.

- The process is repeated to separate the deflected beam into two again, obtaining two beams, and finally each of these beams is separated into three to get the first six beams (Fig. 4.7).

- To obtain the next six beams, the initial half beam, which is was not deflected is transported to be dispersed using a second -1.8 T dipole. Then, the same configuration is used to obtain the other six beams. To get the beams 10, 11 and 12 the beam is dispersed again to improve the separation in momentum distribution plots. At the end 12 beams are produced as is shown in Fig. 4.7.

The momentum distribution of each beam is calculated using G4beamline as soon as a beam is divided. G4beamline provides an output file which contains information, mainly of

Table 4.1. Parameters of the basic cell to divide the initial beam.

	Dipole	**FQ**	**ES**	**MS1**	**MS2**	**DQ**	**Unit**
Magnetic Field B	-1.8	-	0.017	0.1	1.0	-	T
Field Gradient G	-	2.0	-	-	-	-2.0	T/m
Length L	1.5	0.66	6.0	3.5	3.0	0.66	m
Radius R	-	1.0	-	-	-	1.0	m
Width w	0.40	-	0.35	1.0	1.0	-	m
Septum thickness	-	-	0.2	4	20	-	mm

coordinates and momentum components of the particles of the beam. For example, Fig. 4.6 shows the distribution in momentum of the initial beam (upper plot) and after it is divided into two (bottom plot). A separation in momentum is observed. There the lower beam (Beam 1) has a smaller mean momentum and the upper beam (Beam 2) a higher mean momentum. The momentum distributions of the final 12 beams are shown in Fig. 4.8, Fig. 4.9, Fig. 4.10,

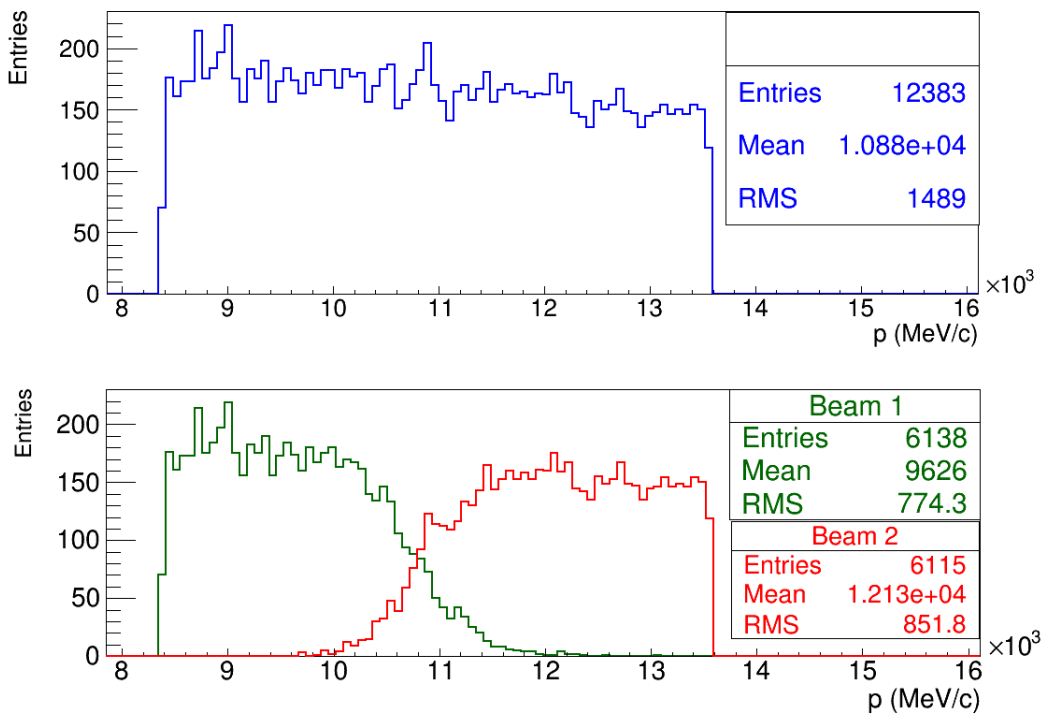

Figure 4.6. Momentum distribution of the initial beam (upper plot) and when it is divided into two (bottom plot).

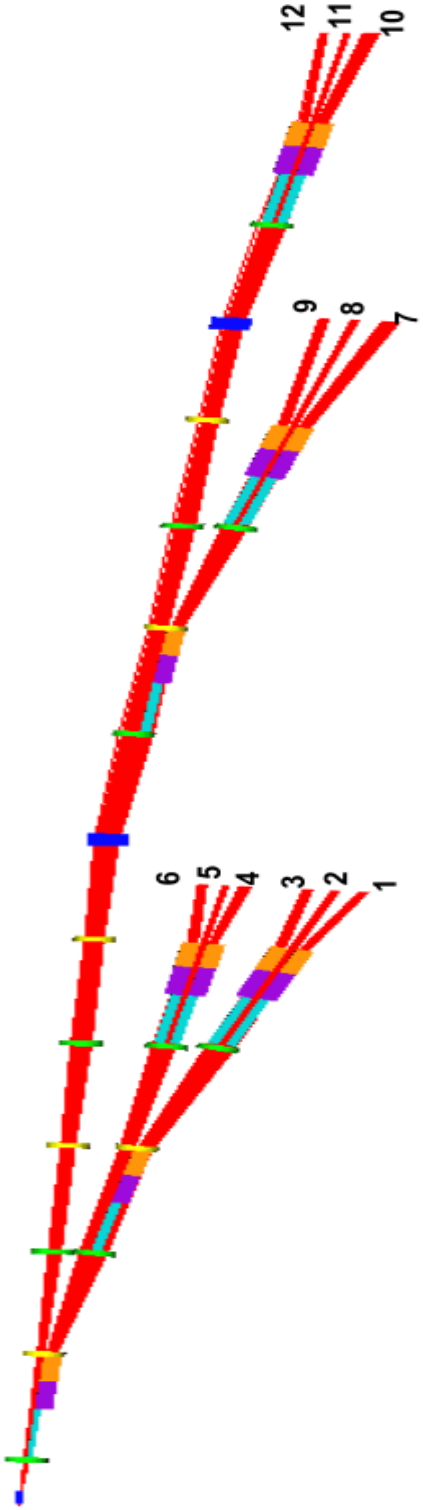

Figure 4.7. An initial beam with momentum acceptance $p = 11.0$ GeV/c $\pm$ 24%is divided to finally get twelve beams.

and Fig. 4.11. There the momenta for each beam can be seen. Twelve different momentum channels are obtained. To calculate the total transmission, the antiproton transmission of all twelve channels are added, and then compared with the transmission of the initial beam (Fig. 4.6, upper plot). The total transmission fraction through all 12 channels is calculated to be 91%, an acceptable result.

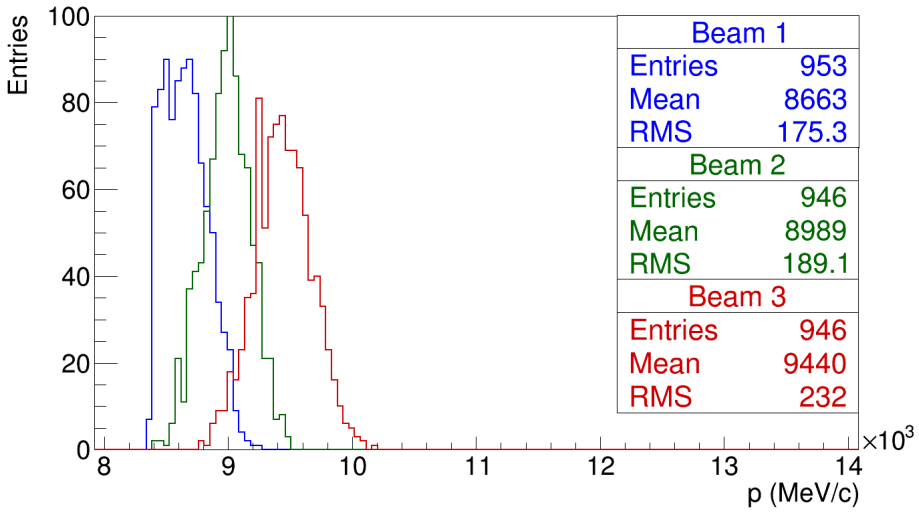

Figure 4.8. Momentum distribution of the beams 1, 2 and 3.

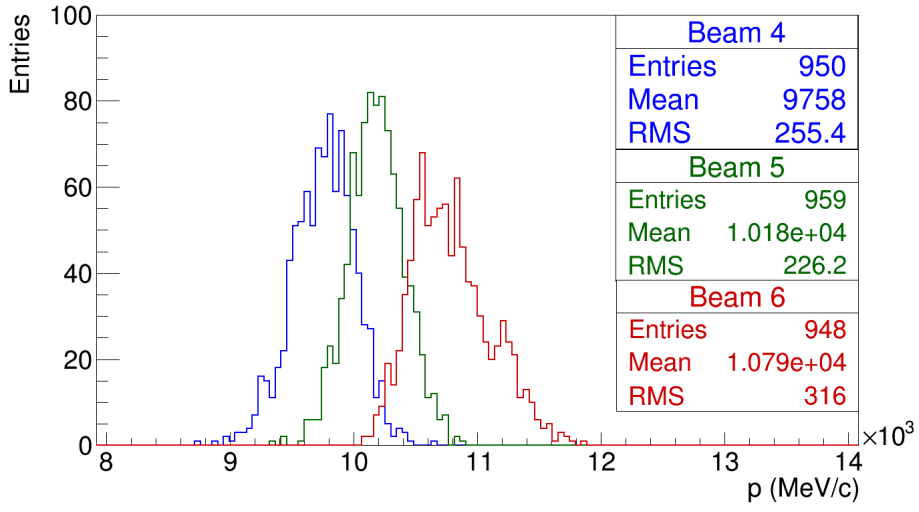

Figure 4.9. Momentum distribution of the beams 4, 5 and 6.

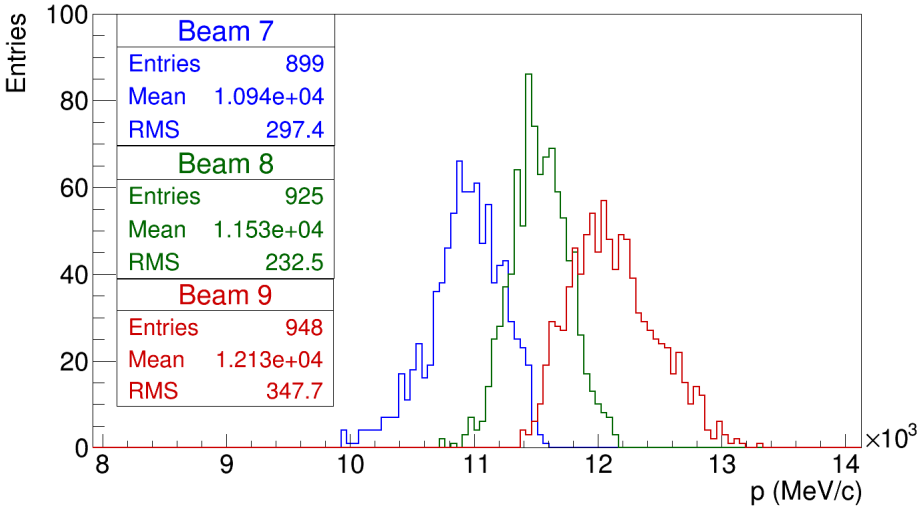

Figure 4.10. Momentum distribution of the beams 7, 8 and 9.

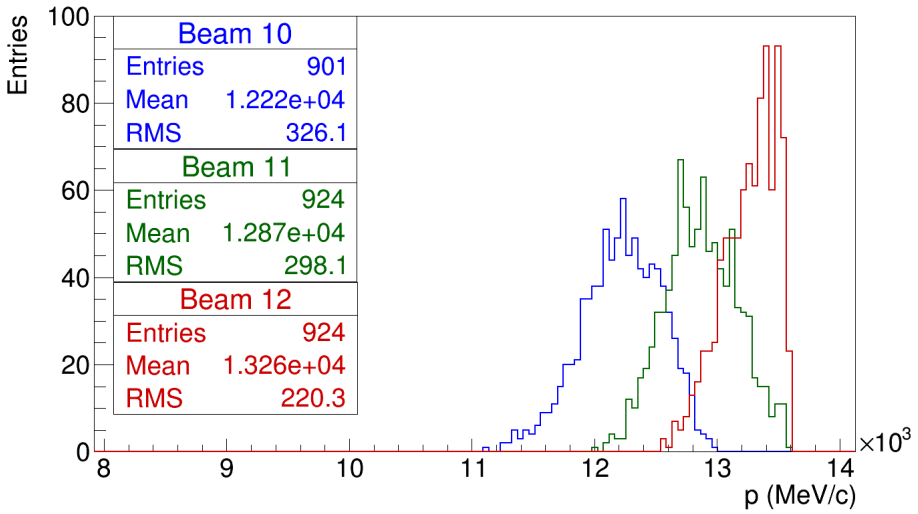

Figure 4.11. Momentum distribution of the beams 10, 11 and 12.

Table 4.3 presents the mean values of the momentum of each beam together with the width of each distribution, which is calculated with the standard deviation and the mean values of each distribution. To improve the acceptance, sextupoles could be used for chromaticity correction. However this is beyond the scope of this work.

Table 4.2. Mean momentum value of the 12 beams obtained.

Beam	p (GeV/c)
1	$8.6 \pm 2.0\,\%$
2	$9.0 \pm 2.1\,\%$
3	$9.4 \pm 2.4\,\%$
4	$9.7 \pm 2.6\,\%$
5	$10.2 \pm 2.2\,\%$
6	$10.8 \pm 2.9\,\%$
7	$10.9 \pm 2.7\,\%$
8	$11.5 \pm 2.0\,\%$
9	$12.1 \pm 2.8\,\%$
10	$12.3 \pm 2.6\,\%$
11	$12.8 \pm 2.3\,\%$
12	$13.2 \pm 1.7\,\%$

CHAPTER 5

5 ANTIPROTON COOLING

In the previous section, it is shown how the initial antiproton beam was dispersed and divided into 12 different momentum channels with a transmission of 91%. Now, because the momentum acceptance into the Debuncher and Accumulator rings is p = 8.9 GeV/c ± 2%, as well as into the Recycler ring, it is necessary to equalize the central momentum of all the 12 beams to that value.

We again look to the Fermilab approach. At Fermilab, antiprotons were stochastically precooled in the Debuncher ring during 2.2 s, with transverse emittance (RMS Normalized) reduction from 330 to 30 μm, then sent to the Accumulator ring to be stochastically cooled and stacked. There, the transverse emittance (RMS Normalized) was reduced from 30 to 15 μm. Table 5.1 shows the reduction in emittance and momentum spread in the Debuncher, Accumulator, and Recycler rings.

Table 5.1. Fermilab antiproton cooling stages [54]. The normalized rms emittance shown comes from multiplying geometric rms emittance by $\beta\,\gamma = \mathrm{p/m} = 8.9/0.938 = 9.49$. A modest amount of stochastic cooling is performed in the Recycler ring to prepare for electron cooling in the same ring.

Stage	Norm. RMS Transverse Emittance $\varepsilon_{N(x,y)}$ (μm)	Momentum Spread Δp/p (MeV/c)
Debuncher Entrance	330	±200
After Phase Rotation		±9
Debuncher Exit	30	±4.5
Accumulator Exit	15	±9
Recycler Exit	2	±1.8

It is known that the stochastic cooling time scales linearly as the number of parti-

cles [20, 55],

$$\tau \approx N \times 10^{-8}\,\mathrm{s}. \tag{5.1}$$

Thus, we take a simple approach, to cool 12× the number of antiprotons, we implement 12 independent cooling channels. Two configurations are proposed. The first choice consists of implementing two Accumulators and one Debuncher for each of the 12 independent systems. The second choice is to use only Debuncher rings, two for each independent system. The total would be 24 Debuncher rings. Finally an electron cooling ring follows either of these configurations. In the second option, stacking is done with electron cooling.

5.1 Debuncher-Accumulator Rings

In choice one, to cool 12× the number of antiprotons, 12 independent cooling systems would be implemented as is shown in Fig. 5.1. Each Debuncher ring phase rotates (section

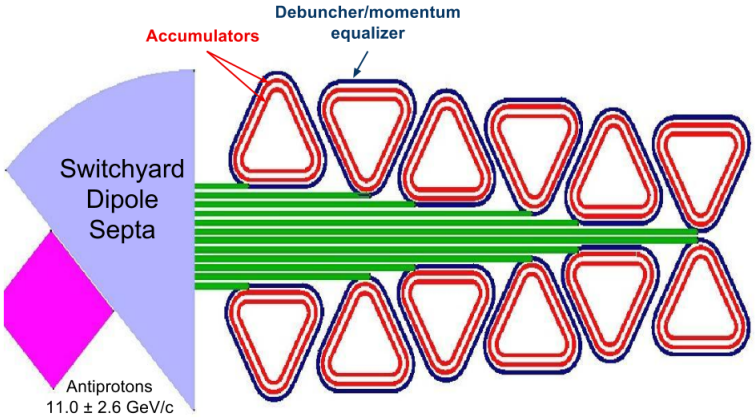

Figure 5.1. To cool 12× more antiprotons, 12 independent cooling systems would be implemented. Two accumulator rings can keep up with one $40 \times 10^{10}\,\bar{p}$/h Debuncher output rate.

2.4.1) the beam to lower the momentum spread, ramps the beam central momenta up or down to 8.9 GeV/c, and stochastically cools. Each Debuncher alternately outputs antiprotons to

each of two associated accumulator rings. Each system would have a Debuncher/momentum equalizer, which would use RF cavities to reduce the 2% momentum spread by decelerating fast antiprotons and accelerating slow ones. In addition, the central momenta of all 12 channels would be equalized. The Debuncher would alternately feed two Accumulator rings. At Fermilab the single Accumulator ring cooled 25×10^{10} $\bar{p}$/h. A second Accumulator ring doubles the time in the deposition orbit and reduces required stack sizes. Two Accumulator rings may be able keep up with one 40×10^{10} $\bar{p}$/h Debuncher. In addition, a single electron cooling ring could follow the stochastic cooling.

5.2 Debuncher Rings

Twenty four Accumulator rings may be difficult to build and operate. Thus, this second option of a cooling system is presented with only Debuncher rings as is shown in Fig. 5.2.

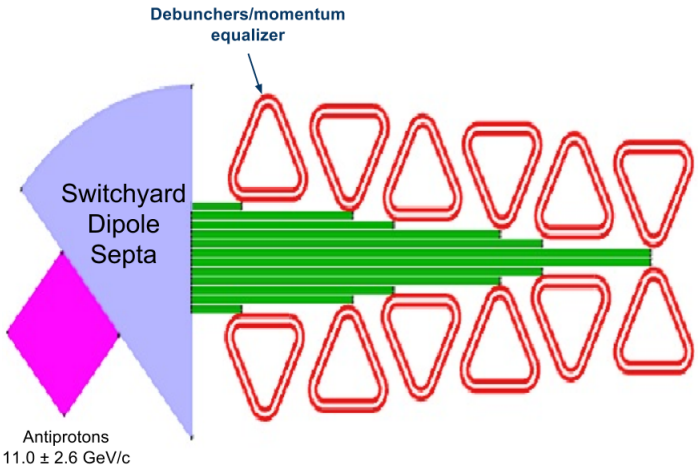

Figure 5.2. 12 independent cooling systems using only Debuncher rings. Alternatively, bunch coalescing might be done with electron rather than stochastic cooling.

In the second option each of the 12 channels would have two Debuncher rings. Each Debuncher receives the respective quantity of antiprotons with a time gap of 2.2 s, but the

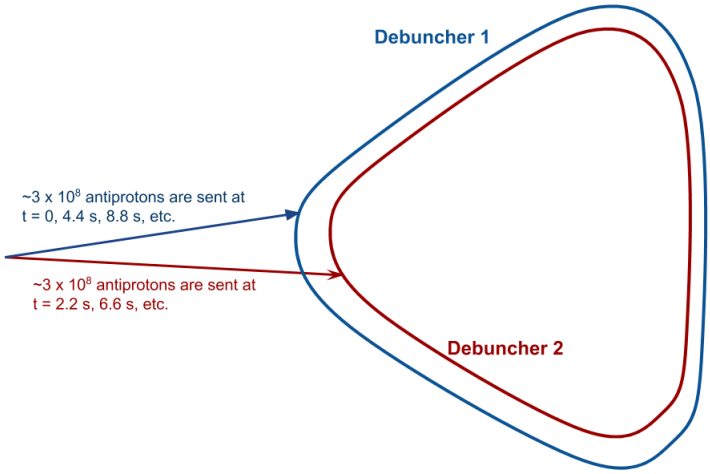

Figure 5.3. Antiprotons are sent alternatively from the target to each Debuncher to increase the cooling time from 2.2 to 4.4 s, allowing emittance (RMS, Normalized) reduction from 330 to 3 μm.

antiprotons would be stay 4.4 s in the respective Debuncher (Fig. 5.3). Thus, the emittance (RMS, normalized) is reduced from 330 to 30 μm during the first 2.2 seconds and from 30 to 3 μm during the next 2.2 s. It will produce more emittance reduction than is obtained with an Accumulator ring. It will not stack bunches. The accumulation and stacking of antiprotons was provided by the Accumulator ring at Fermilab. Since this new proposed cooling system does not include Accumulator rings, stacking would be performed in the electron cooling ring. Antiprotons must be sufficiently pre-cooled for electron cooling to work. The velocities of the antiprotons and electrons must be close to each other.

5.3 Electron Cooling System

In addition to this new cooling system, a single electron cooling ring could follow the antiproton cooling. Electrons can cool large numbers of medium emittance antiprotons in one ring [56, 57]. In 2005 electron cooling was introduced at the Recycler ring at Fermilab with the purpose of providing additional cooling to the antiprotons. An important consequence of this was an increase in luminosity [58]. The Fermilab electron cooling system is shown

in Fig. 5.4. An 8 m high electrostatic generator supplies an electron beam (produced by a thermionic cathode gun) with kinetic energy of 4.3 MeV, current of 0.5 A, and beam power of 2.15 MW. The 20 m cooling section is incorporated into the Recycler ring. In that section the 4.3 MeV electrons and 8.9 GeV antiprotons experience Coulomb interaction so that fast antiprotons will slow down and the slow ones will speed up. The warmer antiprotons cool down and the cooler electrons get warmer. This cooling section is composed of 10 solenoid modules, each 2 m long, with low magnetic field (0.01 T). Finally, the electrons are returned back through a separate line. The electron cooling system parameters are summarized in Table 5.2.

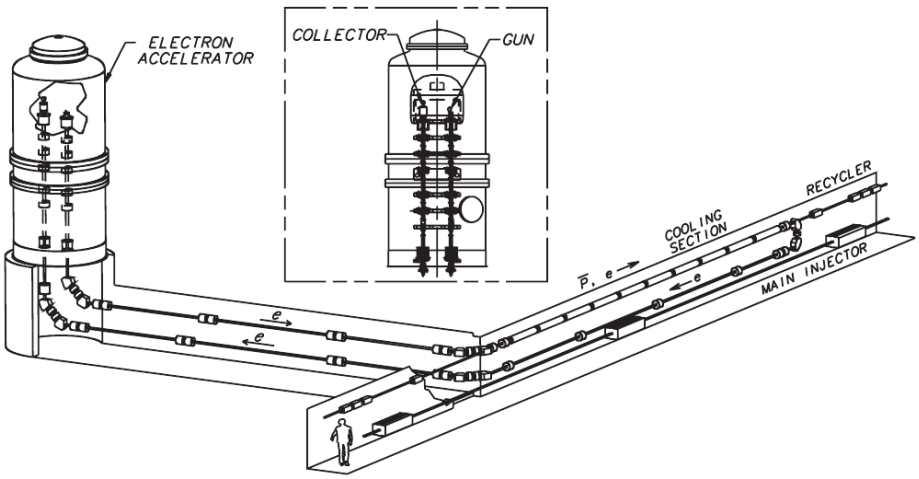

Figure 5.4. Fermilab Electron Cooling System [59].

Table 5.2. Electron Cooling System Main Parameters.

	Value	Unit
Electron Beam Energy	4.3	MeV
Beam current	0.5	A
Voltage ripple, rms	500	V
Cooling Section Length	20	m
Solenoid Module Field	0.01	T
Beam radius	6	mm
Angular Spread	0.2	mrad
Energy Spread	300	eV

This cooling system, decreases the longitudinal emittance from 100 eV-s to 50 eV-s. This emittance reduction is reached in 30 minutes for stacks up to 600×10^{10} antiprotons [60].

With either of the two cooling systems described in the preceding sections, around 20×10^{10} antiprotons per hour are sent alternately by each Accumulator or Debuncher to the electron cooling ring. Thus, in 1 hour the electron cooling ring will receive 480×10^{10} antiprotons.

The electron cooling time is independent of the number of particles being cooled, but is proportional to γ^2 (where $\gamma = \mathrm{E/m}$) and the ring fraction occupied by the electrons. Consequently, if we keep the same electron ring size and the total antiproton energy is reduced by a factor of three, from 8.94 GeV to 2.98 GeV, the cooling rate increases by a factor of nine. Therefore, the electron cooling time would decrease from 30.0 to 3.3 minutes. The parameters of the antiprotons in the ring, where the 20 m electron cooling section is inserted, are shown in table 5.3.

Table 5.3. Electron Ring Main Parameters.

	Value	Unit
Circumference	3300	m
Energy	3.0	GeV
γ_{rel}	3.2	
β_{rel}	0.95	
β function	20	m
ε_N (RMS)	1.5	μm
Beam Size (σ)	3	mm

In the absence of 24 accumulator rings, all the antiprotons bunches would be stacked in the single electron cooling ring. The 8.9 GeV/c antiproton beam started out with a momentum spread of 2% or about 200 MeV/c. Table 5.1 shows the progression of antiproton cooling at Fermilab. Only a small amount of additional stochastic cooling had to occur in the Recycler ring before electron cooling could commence. The Debuncher ring had two longitudinal and four transverse stochastic cooling systems. Antiprotons at Fermilab were cooled from 330 μm to 30 μm in the Debuncher ring. Phase rotation alone in the Debuncher

was almost enough to lower the momentum spread to the level needed for electron cooling. The Fermilab electron cooling ring reduced longitudinal emittance by a factor of two in 30 minutes. In thirty minutes the system in this paper would produce 9000 bunches, which is roughly the number of antiproton bunches in the machine. They would just need to be coalesced with bunches produced in previous half hour intervals. The current system might be enough. However, electron cooling is proportional to $1/\gamma^2$. Reducing the total antiproton energy by a factor of three from 8.94 GeV to 2.98 GeV decreases γ by a factor of three and increases the cooling rate by a margin of nine.

The electric field arising from space charge is given by [61]

$$E_s = E_w - \frac{e g_0}{4\pi\epsilon_0\gamma^2}\frac{\partial\lambda}{\partial s} \tag{5.2}$$

where E_s and E_w are the electric fields at the beam pipe center and wall (see Fig. 5.5), $e = 1.6 \times 10^{-19}$ coulombs, $g_0 = 1 + 2\ln(b/a)$ is a geometry factor, a is the beam radius, b is the beam pipe radius, $\epsilon_0 = 8.85 \times 10^{-12}$ farads/meter, and λ is the antiproton line density. The Fermilab Recycler had four RF cavities and a combined total accelerating gap voltage

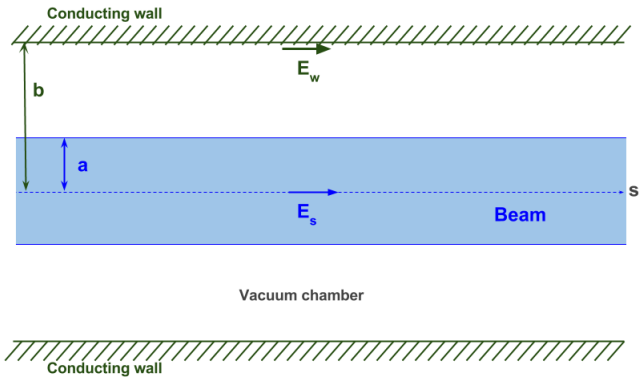

Figure 5.5. Electric fields at the beam pipe center and wall of a circulating beam.

of 2 kV [62]. This may need to be increased to 36 cavities and 18 kV to control space charge,

if the ring energy were lowered by a factor of three.

5.4 Recycling of Antiprotons in the Collider Ring

The production of antiproton beams is more difficult than proton beams, thus maximal conservation of antiprotons is important. It will be most efficient to recycle $\bar{p}$'s to conserve, rather than dumping them at the end of runs. Antiprotons in the collider ring can be recycled without leaving the ring. During the CERN S$p\bar{p}$S ramping run [63, 64] beam energy was ramped as collisions occurred.

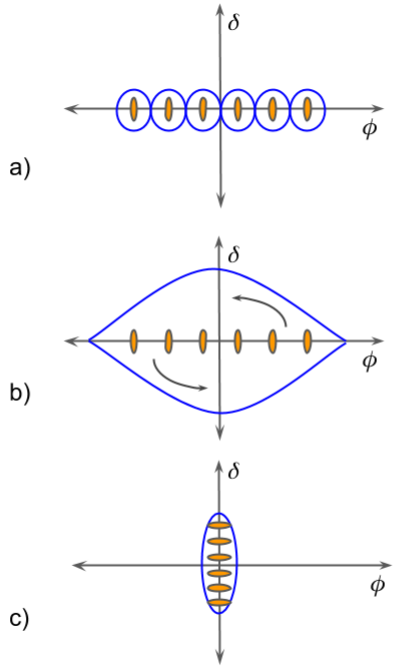

Figure 5.6. Snap Bunch Coalescing. (a) A group of bunches are centered at low frequency and their momentum spread is reduced. From (b) to (c) the bunches are rotated for 1/4 of a synchrotron oscillation period at low frequency and then captured at high frequency. The momentum spread increases and the bunches are captured in a single bucket.

New antiprotons would be joined to depleted bunches in the collider ring. This technique is called snap bunch coalescing, in which two bunches are combined to form a larger bunch with more antiprotons. This process is shown in Fig. 5.6. The horizontal axis corresponds to the azimuth angle (ϕ) in the ring or time spread, and the vertical axis is the energy

offset with respect to the ring energy. Generally two radio frequency (RF) systems operate with different frequency . The bunches are rotated for 1/4 of a synchrotron oscillation period at low frequency (2.5 MHz) and then captured at high frequency (53 MHz) [65]. Finally new and old antiprotons bunches would be completely coalesced with synchrotron damping (section 2.6), which decreases transverse emittance. Synchrotron damping also compensates for the loss of antiprotons from collisions so that the luminosity can be maintained during a run [5].

CHAPTER 6

6 COLLIDER DESIGN AND PARAMETERS

6.1 Collider Layout

For the construction of the 100 TeV $p\bar{p}$ collider, two possible rock strata are considered: Fermilab (Chicago, IL) dolomite and Dallas (Texas) chalk. Driving the decision on location are the considerations that Fermilab would have the advantage of existing infrastructure and Texas would have lower tunneling costs. Fig. 6.1 shows the proposed configuration for the 100 TeV $p\bar{p}$ collider.

The components are described below:

- An upgraded 800 MeV super-conducting Linac [66], which Fermilab has proposed to provide megawatt proton beams for muon and neutrino experiments. The 190 m long Linac would accelerate H^- ions to an energy of 800 MeV before passing them through a thin carbon foil, as was done previously at low energy, to remove the electrons. This allows charge exchange injection into the Booster and avoids a kicker magnet. More 800 than 400 MeV protons can be injected into the Booster.
- The Booster accelerates the 800 MeV protons to an energy of 8.94 GeV. The Booster would run at 15 Hz.
- The 120 GeV ring receives the 8.94 GeV protons to be accelerated to 120 GeV energy, which are sent to the antiproton source to produce the antiprotons.
- For antiproton production, a Fermilab-like antiproton source is adapted to the new collider. This will collect 12× more antiprotons with the switchyard dipole septa, where the antiprotons are dispersed and separated into 12 different momentum channels. For antiproton cooling 12 sets of rings are implemented.

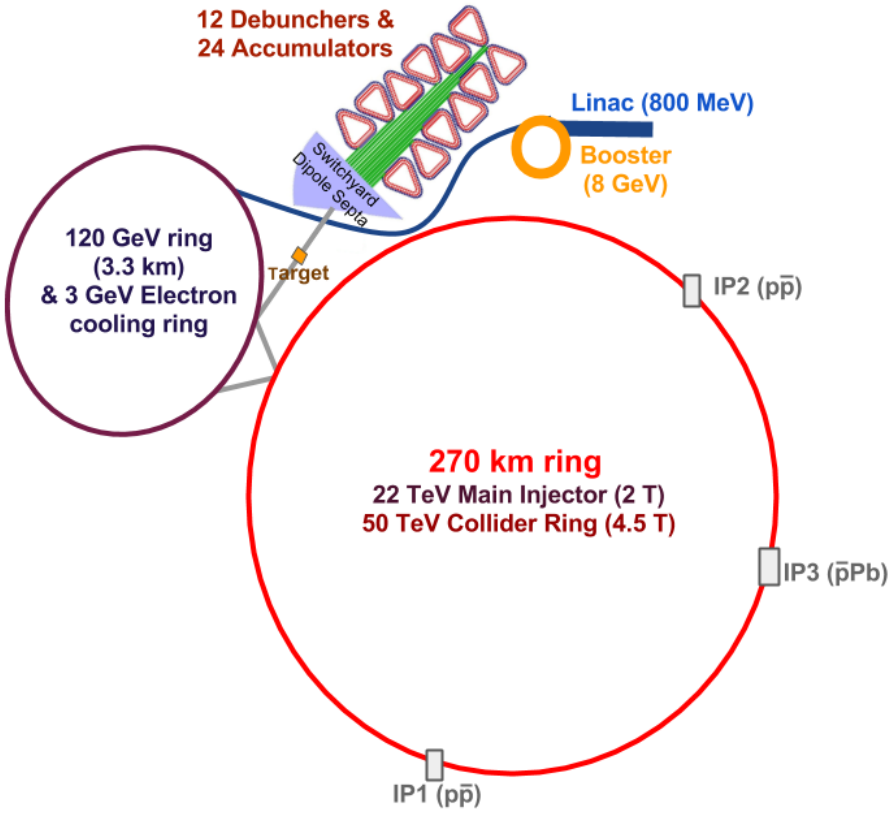

Figure 6.1. 100 TeV proton-antiproton collider (not to scale). An intermediate energy ring between 120 GeV and 22 TeV is not shown. Bunch stacking in the single electron cooling ring might replace the 24 Accumulator rings. A bit of additional transverse cooling would have to be coaxed out of the Debuncher rings to allow electron cooling.

- The electron cooling ring receives and provides additional cooling to the antiprotons coming from the antiproton source. The 20 m long electron cooling system is inserted inside the 3 GeV ring, which would be 3.3 km in circumference.
- In the 120 GeV ring, both protons and antiprotons are accelerated to 120 GeV before transfer to the 22 TeV Injector. An intermediate energy ring may also be useful.
- The 22 TeV Injector accelerates the protons and antiprotons to 22 TeV. This energy would be reached using 2 T magnets in the 270 km ring tunnel.

- Finally, the 50 TeV collider ring will accelerate the protons and antiprotons from 22 TeV to 50 TeV to collide them with a 100 TeV center of mass energy. The 50 TeV energy would be reached using 4.5 T magnets in a 270 km circumference ring. Both 22 and 50 TeV rings share the same tunnel.

The relatively inexpensive 2 T superferric magnet injector would be built first and used as a collider. The 4.5 T NbTi magnets would be an upgrade. Collisions would include $p\bar{p}$ and $\bar{p}\,Pb$. Using both the 2 T and 4.5 T rings would allow asymmetric $Pb\,Pb$ collisions. Lepton colliders might also share the tunnel [39, 40, 67–78].

In Illinois, the 270 km ring could be annexed to the Tevatron at Fermilab as is shown in Fig. 6.2. In Texas, the 270 km ring could be connected to the partially existing SSC

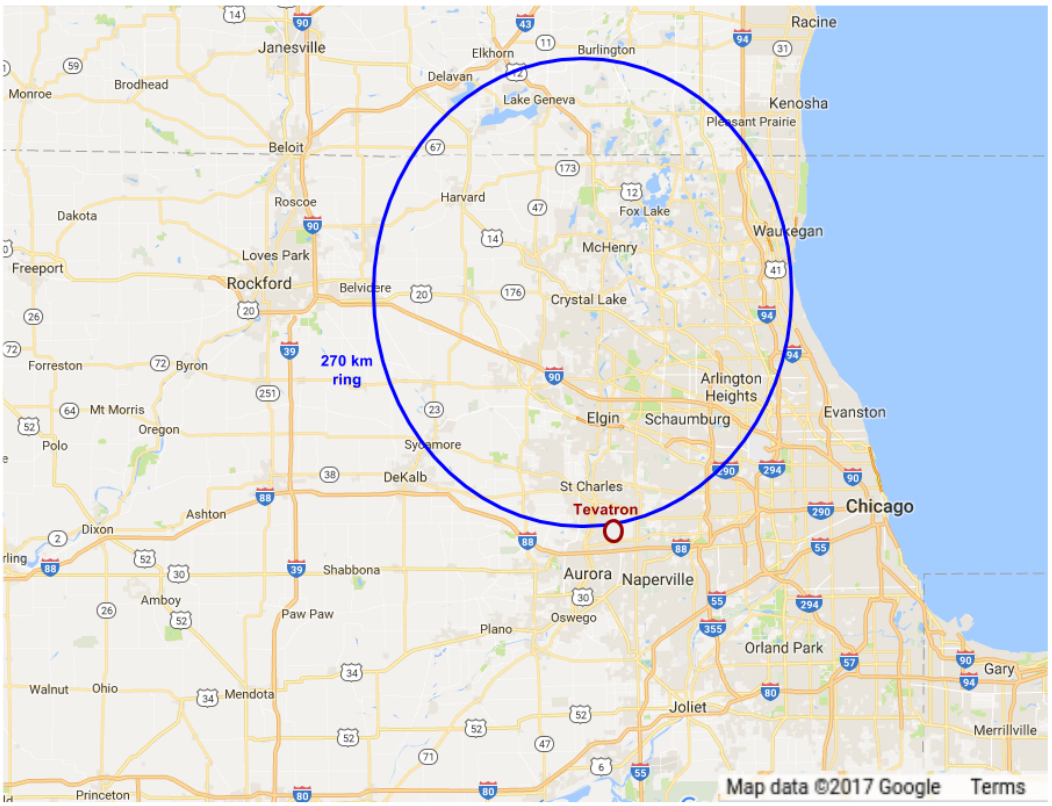

Figure 6.2. Possible scenario to construct the 270 km ring in Illinois connected to Fermilab. An engineering study has been done for a 233 km ring at Fermilab [79, 80]. Map data: Google.

(Superconducting Super Collider) [81] ring tunnel. Of its initial 87 km design, 45% was bored. The goal of this tunnel was to provide proton-proton collisions with a center of mass energy of 40 TeV, much higher than the Large Hadron Collider. The project was canceled in 1993 due to the higher costs (around $12 billion) compared with the initial $4.4 billion budgeted cost [82]. The increase in cost was partially due to the magnets (6.6 T) that were in development. This geographical zone has the advantage of a homogeneous soft rock composition allowing rapid and cheaper tunnel boring, which is a way to reduce costs. Fig. 6.3 shows the 270 km ring on a map.

Figure 6.3. Layout of the 270 km ring around Dallas, Texas [83]. Map data: Google.

The 270 km ring would be difficult to build at CERN due to the cost of tunneling under the Jura mountains. Recent analysis does consider the construction of a 100 TeV collider FCC (Future Circular Collider) with a 80-100 km ring circumference in the Lake Geneva valley as shown in Fig. 6.4. This would be a positron-electron (e^+e^-) and a proton-

proton collider. For this 80-100 km ring, geological conditions are being evaluated. Risks and costs are being considered [84].

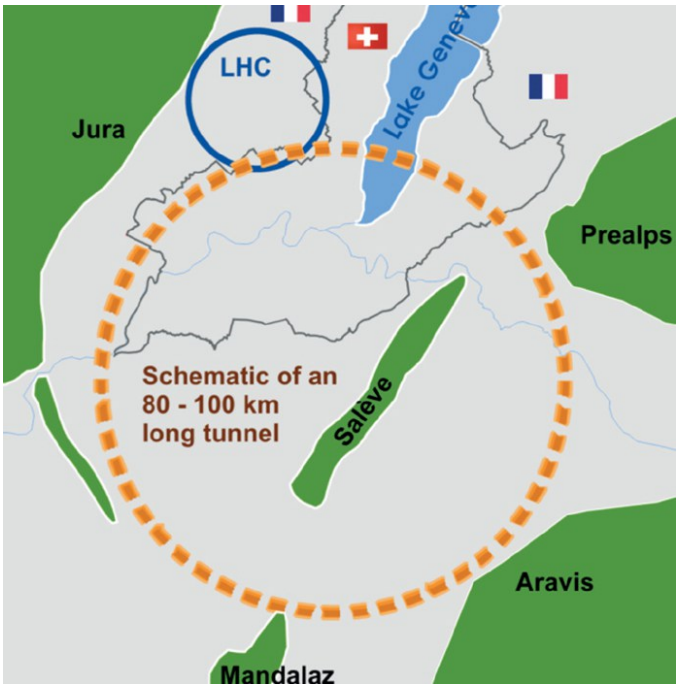

Figure 6.4. 80-100 km tunnel to host a 100 TeV pp collider at CERN in the Lake Geneva valley. Image credit: CERN.

6.2 Tunneling

Tunneling cost depends on geology. Table 6.1 shows the cost per meter estimates for boring 4 m diameter tunnels in three different locations. These values are taken from M. Breidenbach and W. Barletta, ESS-DOC-371 [85] to estimate the total cost of a 270 km tunnel. At CERN the tunnel is limited to 80-100 km due to the French Jura mountains. A tunnel larger than 100 km would cost much more than \$39,000/m. For this reason the total cost for a 270 km tunnel at CERN is not presented in the table. Now, comparing the total cost for tunneling at Fermilab and Texas, the cost difference is a factor of 2.5. Texas chalk is easier to bore than Illinois dolomite.

The LEP tunnel construction project took 4 years, beginning in 1985 and finishing in 1989. Three tunneling machines were used to bore the 4 m diameter tunnel. The average

Table 6.1. Comparison between tunneling cost for three different locations considered for a 270 km collider ring [85].

	Cost/m	270 km tunnel
CERN (Molasse/limestone)	\$39,000	100 km limit
FERMILAB (Dolomite)	\$15,000	\$4 billion
Texas(Chalk/marl)	\$6,000	\$1.6 billion

bore rate per tunneling machine was approximately 5 meters/day. The three tunnels that compose the channel tunnel between France and the UK is each 50 km long. The project took 6 years using eleven tunneling machines. All this information is shown in Table 6.2, along with the calculation of the volume of rock removed. The channel project consisted of two 8 m diameter tunnels plus one 4 m diameter tunnel. From this, we can estimate that the rock removed was 0.025 million m^3/year per machine for LEP and 0.085 million m^3/year per machine for the Channel Tunnel. For a 270 km tunnel, 3.4 million m^3 of rock would have to be removed. However, rock in Texas is faster to bore; 40 m/day based on SSC tunneling rates [5]. Thus, it would take about 4.6 years using 4 tunneling machines, even better, 3.7 years using 5 tunneling machines. Fermilab has relatively constant dolomite layers. For a 4 m diameter tunnel the average advance rate for a tunnel boring machine is about 20 m/day [86]. Thus, it can be estimated that using 8 boring machines the tunneling time is roughly 4.6 years.

Table 6.2. Tunneling-time estimate.

	Length (km)	Volume of rock (million m^3)	Time (years)	Tunneling Machines
LEP	27	0.3	4	3
Channel Tunnel	3×50	5.6	6	11
Tunnel (Illinois)	270	3.4	4.6	8
Tunnel (Texas)	270	3.4	3.7	5

6.3 Main Dipole Magnets

In a collider the dipole magnets represent a large budget item. The main LHC magnets are located in the 27 km main ring with a packing fraction of 66%, which gives a bending radius of 2.8 km. According to the equation 2.17 (from chapter 1), ρ[m] = p[GeV/c]/0.3B[T], the magnetic field is ∼8.3 T for an energy of 7 TeV. These twin bore magnets are made of Niobium-Titanium (NbTi) superconducting material running at a temperature of 1.9 K. Fig. 6.5 shows a single aperture, of the LHC main dipole magnet, of the two required for the two beams traveling in opposite direction for the collision. Two layers of NbTi cable

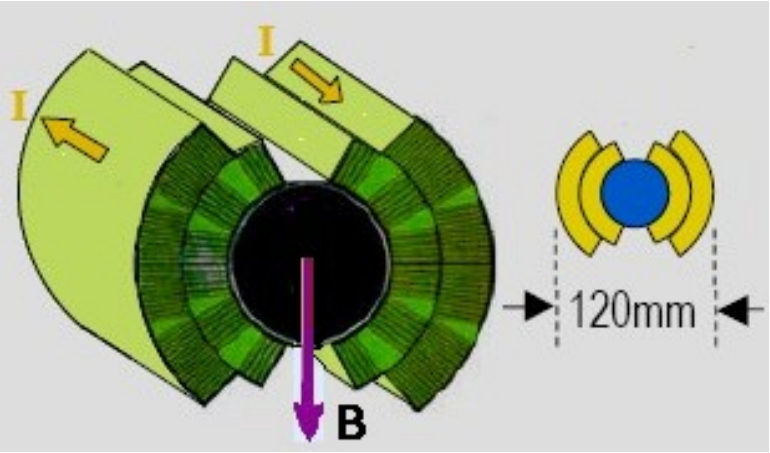

Figure 6.5. LHC Main Dipole Magnet. There are two cosθ layers [87].

are distributed to form a "cos θ" structure. The dipole is 14.3 m long, it operates at 1.9 K and the total current for a 8.3 T magnetic field is 11.8 kA. The LHC required 1232 main dipoles, which represented a total cost of $660 million. The cost of each dipole magnet was $0.5 million [88]. Furthermore, the LHC dipole magnet cost is about 3 times more than its superconductor.

A 100 km collider with E_{cm} = 100 TeV requires 16 T magnets, which would need Nb_3Sn material and its production is still under study [89]. A better balance between magnet and tunneling costs may be found at lower magnetic fields. Stored magnetic field energy decreases linearly with ring circumference. A 100 TeV proton-proton collider in a 270

km tunnel around Dallas, Texas using 4.5 T dipole magnets has been proposed [83]. These magnets use superconducting NbTi cable in conduits as is shown in Fig. 6.6. Twenty turns of cable make up each dipole winding. The magnet operates at 4.5 K. These 4.5 T magnets use about half as much NbTi conductor per Tesla/meter as 8 T $\cos\theta$ LHC magnets. Fig. 6.7 shows the magnetic configuration of the dipole.

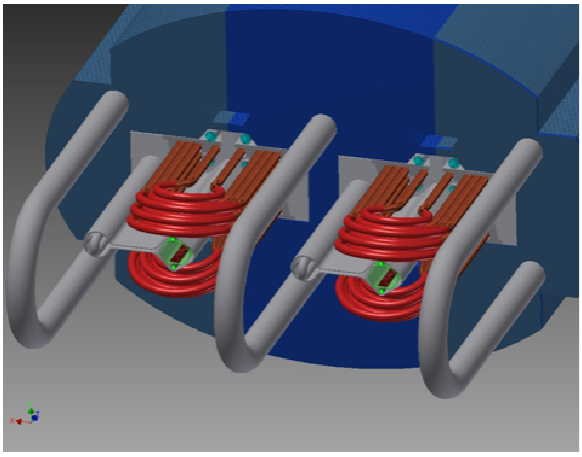

Figure 6.6. 4.5 T superferric dual bore dipole magnet [5]. A $p\bar{p}$ collider would only require one bore.

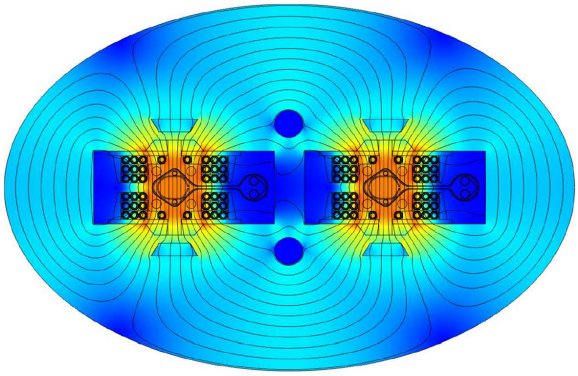

Figure 6.7. 4.5 T superferric dual bore dipole magnetic design [5]. A $p\bar{p}$ collider would only require one bore.

For the 100 TeV proton antiproton collider, the energy of the Injector would be 22 TeV. Using 2 T superferric, iron dominated magnets, the packing fraction would be 86%. The Injector Ring would share the same 270 km tunnel as the collider ring. These superferric

magnets need minimal current because the magnetic field just has to be generated inside the gap. The iron does limit the maximum magnetic field generated to 2 T. The relatively inexpensive 2 T superferric magnets would be built first and used as a 44 TeV collider. Ultra low carbon steel would be employed [90]. These would be H frame, iron dominated magnets with superconducting MgB_2 cable in conduit at a temperature of 25 K. At today's \$5 per kiloamp-meter cost, the total conductor price would be approximately \$150M. Cooling would be with neon which costs \$100 per liquid liter. Liquid neon has a heat of vaporization of 1.71 kilo-Joule/mole, much larger than 0.083 kilo-Joule/mole for helium. The MgB_2 would be in the magnet fringe field at a fraction of a Tesla. CERN plans to use MgB_2 as magnet leads for superconducting Nb_3Sn quadrupoles [91].

The high luminosity, 100 TeV $p\bar{p}$ collider resides in the 270 km tunnel. With a packing fraction of (86%), the bending radius would be 37 km, which would requires ∼4.5 T magnets for a 50 TeV energy beam. Because of the advantages of the 4.5 T dipole magnets as described above, these are proposed for the 270 collider ring with the difference that only a single bore is needed, instead of a dual bore as required for a proton-proton collider. It is important to note that with respect to the LHC collider, the energy is increased 7 times using only a factor of two more NbTi superconductor. Table 6.3 summarizes the main parameters for the 270 km ring.

Table 6.3. Main Dipole Magnets for the 270 km collider ring.

Circumference	270 km
Injection Momentum	22 TeV/c
Collision Momentum	50 TeV/c
Magnetic NbTi Field Dipole	4.5 T
Dipole cost (T-m)	\$1150
Packing fraction	0.86
Total cost estimate	\$1.2 Billion

6.4 Parameter Calculation

Table 6.4 lists the main parameters for the Tevatron, the LHC, a 100 TeV (pp) Future Circular Collider FCC-hh, and this 100 TeV $p\bar{p}$ collider. The calculations of the parameters for the 100 TeV $p\bar{p}$ collider are explained below:

Table 6.4. Parameter list for the Tevatron, the LHC, the Future Circular Collider FCC-hh, and the 100 TeV $p\bar{p}$ proposed here.

Collider Parameters	**Tevatron**	**LHC**	**FCC-hh** [92]	**100 TeV p$\bar{\text{p}}$**	**Unit**
Luminosity ($\mathcal{L}$)	3.4 x 10^{32}	1.0 x 10^{34}	5.0 x 10^{34}	1.0 x 10^{34}	$cm^{-2}s^{-1}$
Energy Center of Mass (E_{cm})	1.96	14	100	100	TeV
Magnetic Field (B)	4.3	8.3	16	4.5	T
Packing fraction	0.77	0.66	0.66	0.86	
Circumference (C)	6.28	27	100	270	km
Bending Radius (ρ)	760	2801	10416	37040	m
Revolution Frequency (f_0)	0.048	0.01	0.003	0.0011	MHz
Collision Frequency (f)	1.7	40	40	12	MHz
Lorentz Gamma Factor (γ)	1044	7460	53304	53304	
Number of Bunches (N_B)	36	2808	10600	10800	
Number of Protons/Bunch (N_p)	29 x 10^{10}	11.5 x 10^{10}	10 x 10^{10}	20 x 10^{10}	
Number of Antiprotons/Bunch (N_a)	8 x 10^{10}			0.32 x 10^{10}	
Total/Inelastic Cross Section	81.9 / 61.9	111 / 85	153 / 108	153 / 108	mb
Events per Bunch Crossing	12	27	170	90	
Norm. RMS Trans. Emittance (ε_N)	3.0 (protons)	3.75	2.2	2.2 (protons)	μm
	1.5 (antiprotons)			1.5 (antiprotons)	μm
Betatron Function at IP (β^*)	0.28	0.55	1.1	0.14	m
Beam Size at IP (σ)	33 (protons)	16.6	6.8	2.4 (protons)	μm
	29 (antiprotons)			2.0 (antiprotons)	μm
Beam-Beam Tune Shift per IP (ξ)	0.006 (protons)	0.003	0.005	0.0003 (protons)	
	0.012 (antiprotons)			0.011 (antiprotons)	
Number of IPs (N_{IP})	2	4	2	3	
SR per meter	0.00015	0.13	29	2.2	W/m
Energy loss per turn (U_0)	0.0000095	0.0067	4.6	1.3	MeV
Longitudinal Damping Time (τ_ε)	305	13	0.5	4.8	h
Transverse Damping Time (τ_x)	610	26	1.0	9.7	h

- The luminosity, $\mathcal{L}$, would be 29 times higher than the Tevatron. The luminosity would be the same as the LHC.

- The center of mass energy E_{cm} would be 100 TeV, the same as the FCC-hh collider and about 50 times the Tevatron energy.

- No new technology is required for the 4.5 T dipole magnets. They are based on NbTi.

- A 270 km ring is needed in order to use 4.5 T magnets. A 100 km ring requires 16 T magnets, which are expensive and still in development studies.

- The revolution frequency f_0 is calculated considering that the particles move almost at the speed of light. This frequency is inversely proportional to the ring circumference. Luminosity is directly proportional to the revolution frequency.

- The collision frequency f is determined by the number of bunches inside the ring, where the distance between bunches is calculated considering that these move almost at the speed of light. Also, the collision frequency equals the number of bunches per beam multiplied by the revolution frequency.

- The Lorentz gamma factor γ is calculated dividing the beam energy by the particle mass. The luminosity is proportional to this factor.

- The number of antiprotons and the luminosity is fixed. More bunches mean fewer antiprotons per bunch, which decreases the number of events per beam crossing. But to keep the luminosity constant, the number of protons per bunch must remain fixed even with more bunches. This increases the amount of synchrotron radiation deposited into magnets. Nonetheless, the events per beam crossing and the synchrotron radiation per meter are both lower in the $p\bar{p}$ machine than in the FCC-hh machine. The number of bunches N_B into the ring would have to be 12 times higher than the Tevatron according to the calculations obtained in chapter 4 for the luminosity requirements, and keeping the same number of protons and antiprotons per bunch. However, using 12 times more bunches than Tevatron, the number of events per bunch crossing was 13 $\times$ higher than the FCC-hh value. Thus, the number of bunches was increased by a factor of 25 to increase the collision frequency, reducing the number of antiprotons per bunch by a factor of 25 in order not to affect the luminosity. Finally the number of bunches is $12 \times 25 \times 36 = 10{,}800$.

- The number of events per bunch crossing equals the cross section times luminosity divided by the collision frequency ($\sigma_{Inelastic}\mathcal{L}/f$). This number is half the value for the FCC-hh collider. This means that the pile-up is less, which is good for the detectors and readout system. Detectors only need half as many channels for reasonable occupancy.

- The Normalized RMS Emittance (ε_N) would be the same as the Tevatron for antiprotons, and for protons the same value as in the FCC-hh machine.

- The beam radius at the interaction point is given by $\sqrt{\epsilon_N \beta^*/(\beta\,\gamma)}$, where $\beta\,\gamma$ = p/m.

- The beam-beam tune shift (ξ) is calculated from equation 2.10 for both protons and antiprotons. The beam-beam tune shift is limit to 0.012-0.015 for each interaction point based on Tevatron experience [93]. This is to avoid beam losses due to resonances. The proton tune shift is caused by the antiproton bunches and vice versa.

- Two interaction regions would be for $p\,\bar{p}$ detectors and one interaction region would be for a $\bar{p}\,Pb$ and asymmetric $Pb\,Pb$ detector.

- The synchrotron radiated power is calculated using equation 2.12.

- The energy loss per turn U_0 is calculated using the equation 2.13. For the 100 TeV $p\bar{p}$ collider this is smaller by a factor of 3.5 compared to the FCC-hh collider because of the lower magnetic field requirement.

- The longitudinal emittance damping time (τ_ε) is calculated using the equation 2.14. The transverse emittance damping time (τ_x) is twice the longitudinal damping time.

6.5 Inner Quadrupole System

The inner quadrupole system provides the final focusing of the beams in the collision point (see section 2.7.2.1). This system plays an important role in the luminosity with regard to the β^* factor, which is the value of the betatron function in the interaction point (IP). Because we are looking for a factor of 2 in luminosity by halving the β^* of the Tevatron, it

is necessary to modify the inner quadrupole system used in one of the experiments of the Tevatron interaction regions. We took as reference the D0 Experiment [94] inner quadrupole triplet.

A MAD-X [31] simulation can be done to study the beam behavior through the quadrupoles before collision. For example, Fig. 6.8 shows the simulation done in MAD-X of the D0 Experiment inner triplet quadrupole to focus the beam at the interaction point (IP) together with the corresponding beta function plots, which are related to the beam size so that the minimum value must be at the IP. There, $\beta^* = 28$ cm and the quadrupoles gradient are 141 T/m for Q1 and Q3, and 138 T/m for Q2.

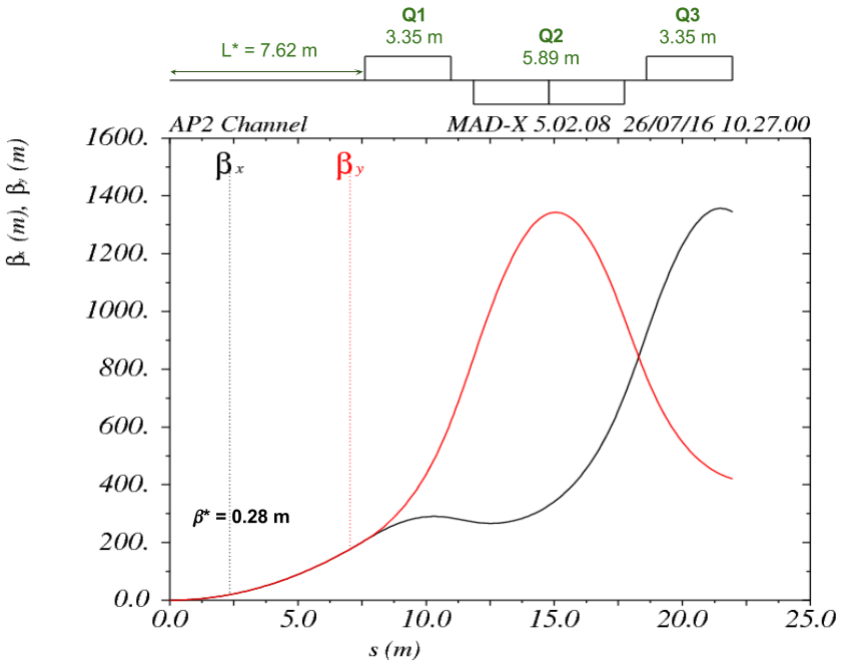

Figure 6.8. Beta function plots for the D0 Experiment interaction region.

The Tevatron and LHC have used NbTi quadrupoles. The LHC plans to upgrade with new technology Nb_3Sn quadrupoles, which can reach high fields around 13 T [95–97]. We take the D0 Experiment triplet quadrupole system as reference to determine the new parameters for a 100 TeV collision energy. The quadrupole system is simulated using Mad-X,

where the β^* value is fixed and the quadrupole lengths are varied in order to obtain $\beta_{x,max}$ = $\beta_{y,max}$ in the beta functions plot. Because a smaller β^* will allow higher luminosity, this is chosen to be half of the β^* at the D0 Experiment's IP. In order to preserve the distance from the interaction point to the quadrupole Q1 (L^*) and β^*= 14 cm, the quadrupole length (l), the separation between the quadrupoles (a) are increased by a factor of 5. Fig. 6.9 shows the inner triplet quadrupole system scaled, where $\beta_{x,max} = \beta_{y,max} = 27$ km. Also, to obtain that optimization the field gradients of the quadrupoles need to be 605 T/m for Q1 and Q3, and 354 T/m for Q2.

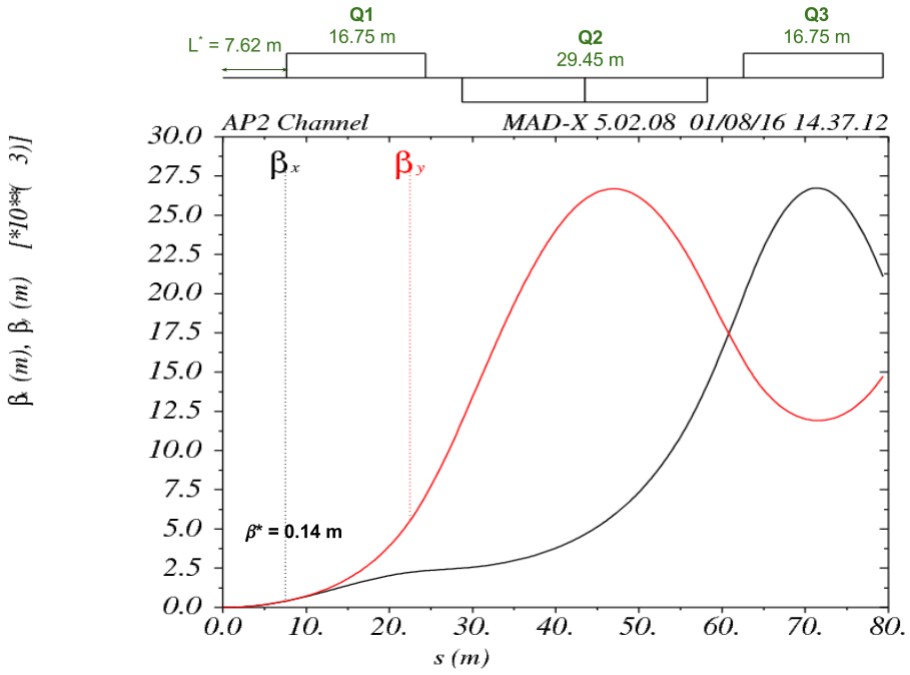

Figure 6.9. Beta functions plots for the 100 TeV $p\bar{p}$ collider interaction region. A combination of quadrupoles focus the beam in the IP with $\beta^* = 14$ cm.

The maximum beam size can be calculated using,

$$\sigma_{(x,y)max} = \sqrt{\frac{\beta_{(x,y)max}\varepsilon_{N(x,y)}}{\beta_{rel}\gamma}} \tag{6.1}$$

with $\varepsilon_{N(x,y)}$ being the normalized transverse emittance, β_{rel}=p/E and γ=E/m is the Lorentz

Table 6.5. Inner Triplet Quadrupole parameters

	E_{beam} (TeV)	G (T/m)	l (m)	L^* (m)	β^*(m)	β_{max}(km)	σ_{max}(mm)
Tevatron	0.98	141/138	3.35	7.6	0.28	1.4	1.7
LHC	7	205	5.5	23	0.55	4	1.4
High Energy pp	50	220/190	20/17.5	36	1.10	40	1.6
High Energy $p\bar{p}$	50	605/354	16.75/14.7	7.6	0.14	27	1.1

gamma factor. Using the same normalized transverse emittance than the Tevatron ($\varepsilon_{N(x,y)}$ = 2.25 μm), a value of 1.1 mm is obtained for the beam size. The quadrupoles field aperture should be around $10\sigma_{max}$ [98] to be large enough for the beam, and a factor of 2 for field quality could be added, to obtain finally a 40 mm aperture. In Table 6.5 are listed the inner triplet quadrupoles parameters, corresponding to the Tevatron, LHC, the 100 TeV pp [99] and $p\bar{p}$ colliders. There, it can be observed that the quadrupole field gradients are higher than those required for the pp collider. However, the quadrupole bore sizes are smaller and the 13 T pole tip field limit is not exceeded. More optimization may be possible. Also, the high field gradients are necessary in order to keep the same distance L^* of the D0 interaction region at the Tevatron. Proton-antiproton events are more central and allow a shorter detector. Quadrupole triplets only have to deal with one beam line in $p\bar{p}$ machines rather than two in pp machines.

CHAPTER 7

7 CONCLUSIONS

The Higgs Boson has been added to the Standard Model of particle physics, but mysteries such as dark matter remain. Exploration to search for new physics in the multi-TeV range would be useful. Currently new physics is being explored with the Large Hadron Collider at CERN and with Intensity Frontier programs at Fermilab and KEK (High Energy Accelerator Research Organization) in Japan. In addition studies and proposals for future high energy colliders have been in development. Among them is a 100 TeV proton-proton collider (FCC-hh) at CERN. A high luminosity 100 TeV proton-antiproton collider may be simpler providing higher cross sections and less synchrotron radiation.

Proton antiproton colliders have shown made important discoveries. In 1982-1983 at CERN the W and Z bosons were detected with the Super Proton Synchrotron (SPS), which was used as a proton-antiproton collider. In addition, the Tevatron proton-antiproton collider at Fermilab, discovered the top quark in 1995. A high luminosity 100 TeV proton-antiproton collider could explore physics beyond the standard model.

A new 100 TeV collider would be designed to search for physics beyond the standard model (BSM). For example, a heavy W' boson may have a mass at the TeV scale and be produced through $q\bar{q}$ annihilation. Antiquarks for W' production and other high mass states can come directly from an antiproton rather than indirectly from gluon splitting in proton-proton collisions.

Compared with a 100 TeV pp collider, the cross section for $p\bar{p}$ collisions is greater than in pp collisions for many high mass states. Synchrotron radiation in superconducting magnets and the vacuum system are reduced because lower beam currents can produce the

same rare events rates. In addition, a $p\bar{p}$ collider only requires one ring instead of the two needed for a pp collider, reducing costs. The SR/meter in our $p\bar{p}$ collider is around 13 times less than the FCC pp collider proposed at CERN. This is driven by the lower required beam currents and using a larger tunnel than can be accommodated at CERN.

It was determined to obtain high luminosity ($\mathcal{L} = 10^{34}$ cm^{-2}s^{-1}) in the 100 TeV $p\bar{p}$ collider, 12× more antiprotons are required. These can be collected by using the same target that the Tevatron used for antiproton production. Antiprotons are plentiful. The key is increasing the antiproton momentum acceptance from 2% to 24% to get 12x more antiprotons. Then, these can be dispersed into 12 different momentum channels to get the require acceptance of about 2% in momentum.

With the increase in the number of antiprotons, 12 parallel cooling systems are required. The stochastic cooling rate in a ring is inversely proportional to the number of antiprotons. One option would be to use two accumulator rings for each Debuncher ring. At Fermilab the Debuncher ring could cool 40 x 10^{10} antiprotons per hour but the Accumulator ring could only handle 25 x 10^{10} antiprotons per hour. The number of Debuncher rings would be 12, which would equalize the antiprotons momentum to 8.9 GeV/c and lower momentum spread using phase rotation followed by longitudinal stochastic cooling. Also, the Debunchers pre-cool the antiprotons transversely during 2.2 s, reducing the normalized rms emittance from 330 to 30 μm. For each Debuncher two Accumulator rings can probably handle the Debuncher output rate of $40 \times 10^{10}\,\bar{p}$/h. Modest final electron cooling in a single ring would follow. The second option is to use only Debuncher rings. Twenty-four Accumulator rings might be difficult to build and operate. In option two, there would be 24 Debunchers in total, two for each of 12 channels. Thus, antiprotons are sent to each Debuncher to increase the cooling time from 2.2 to 4.4 s, allowing a reduction in the transverse emittance (rms, normalized) from 330 to 3 μm. Longitudinal antiproton stacking and additional cooling would be done in a single electron cooling ring. Reducing the total antiproton energy by a factor of three increases the electron cooling rate by a factor of nine.

Large tunnels have already been successfully bored. A 270 km circumference ring permits to use simple 4.5 T superferric NbTi magnets and reduced stored magnetic field energy. These magnets use 2× as much NbTi superconductor as LHC magnets, but provide 7 times more energy. Nb_3Sn is only used for quadrupole triplets to generate small spot sizes at detectors.

Antiprotons would be recycled during runs without leaving the collider ring, by joining them to new bunches with snap bunch coalescence and synchrotron damping. This effectively increases antiproton production.

The collider would be staged. The 270 km ring would initially provide collisions at E_{cm} = 44 TeV with 2 T low cost iron dominated superconducting magnets. The 100 TeV collider would follow as an upgrade, using 4.5 T dipoles.

Proton antiproton events are more central and allow a shorter detector. An Inner Quadrupole System presented herein, permits a low β^* with quadrupoles closer to the IP. A factor of 2 in luminosity is gained. The Tevatron used NbTi final focus quadrupole triplets, which could be replaced with high gradient Nb_3Sn quadrupoles that can reach 13 T.

Two location options are presented to build the proton-antiproton collider. In Texas tunneling is cheaper and faster. At Fermilab the existing facilities would represent an advantage.

Finally, it is important to point out that to construct this high luminosity 100 TeV proton-antiproton collider does not require new technology dipole magnets, and most of the Tevatron components can be used and extended in order to get a powerful collider.

BIBLIOGRAPHY

BIBLIOGRAPHY

[1] G. Aad *et al.* [ATLAS Collaboration], "Observation of a new particle in the search for the Standard Model Higgs boson with the ATLAS detector at the LHC," Phys. Lett. B **716** (2012) 1.

[2] S. Chatrchyan *et al.* [CMS Collaboration], "Observation of a new boson at a mass of 125 GeV with the CMS experiment at the LHC," Phys. Lett. B **716** (2012) 30.

[3] F. Abe *et al.* [CDF Collaboration], "Observation of top quark production in $\bar{p}p$ collisions," Phys. Rev. Lett. **74** (1995) 2626.

[4] S. Abachi *et al.* [D0 Collaboration], "Observation of the top quark," Phys. Rev. Lett. **74** (1995) 2632.

[5] P. McIntyre *et al.*, "Magnet Design and Synchrotron Damping Considerations for a 100 TeV Hadron Collider," IPAC-2015-THPF134.

[6] N. Serra (2015, April 25). Standard Model. Physik Institut. Retrieved from http://www.physik.uzh.ch/groups/serra/StandardModel.html.

[7] Luigi Di Lella and Carlo Rubbia, "The Discovery of the W and Z Particles," Adv. Ser. Dir. High Energy Phys. **23** (2015) 137.

[8] G. Arnison *et al.* (UA1), "Experimental Observation of Isolated Large Transverse Energy Electrons with Associated Missing Energy at $\sqrt{s} = 540$ GeV," Phys. Lett. **122B** (1983) 103.

[9] M. Banner *et al.* (UA2), "Observation of Single Isolated Electrons of High Transverse Momentum in Events with Missing Transverse Energy at the CERN $\bar{p}p$ Collider," Phys Lett. **122B** (1983) 476.

[10] G. Arnison *et al.* (UA1), "Experimental Observation of Lepton Pairs of Invariant Mass Around 95 GeV/c^2 at the CERN SPS Collider," Phys. Lett. **126B** (1983) 476.

[11] P. Bagnaia *et al.* (UA2), "Evidence for $Z^0 \to e^+e^-$ at the CERN $\bar{p}\,p$ Collider," Phys. Lett. **129B** (1983) 130.

[12] Elvin Harms, Jim Morgan, Brian Drendel, and Stan Johnson, "The Antiproton Source Rookie Book," (2009), p 32. http://operations.fnal.gov/rookie_books/Pbar_v2.2.pdf.

[13] S. Nagaitsev, "Fermilab Antiproton Source, Recycler Ring, and Main Injector," arXiv:1408.0759.

[14] Matthew Sands, "The Physics of Electron Storage Rings: An Introduction," SLAC-R-121 (1970).

[15] S. Schröder *et al.,* "First laser cooling of relativistic ions in a storage ring," Phys. Rev. Lett. **64** (1990) 2901.

[16] D. Neuffer, "Principles and Applications of Muon Cooling," Part. Accel. **14** (1983) 75.

[17] A. V. Tollestrup and G. Dugan, "Elementary Stochastic Cooling," AIP Conf. Proc. **105** (1983) 954.

[18] Simon van der Meer, "Stochastic Cooling and the Accumulation of Antiprotons," Rev. Mod. Phys. **57** (1985) 689 (p. 691).

[19] J. Liouville, "Note on the Theory of the Variation of Arbitrary Constants," J. Math. Pure. Appl. **3** (1838) 342.

[20] M.G. Minty and F. Zimmermann, "Measurement and Control of Charged Particle Beams," Springer, 2003, DOI:10.1007/978-3-662-08581-3.

[21] Vladimir Shiltsev and Alvin Tollestrup, "Emittance Growth Mechanisms in the Tevatron Beams," JINST **6** (2011) P08001.

[22] Stephen D. Holmes and Vladimir D. Shiltsev, "The Legacy of the Tevatron in the Area of Accelerator Science," Ann. Rev. Nucl. Part. Sci. **63** (2013) 435.

[23] W. Barletta,
http : *//uspas.fnal.gov/materials/*09*UNM/Unit*_11*_Lecture*_18*_Synchrotron_radiation.pdf*.

[24] CERN, http://www.lhc-closer.es/1/4/12/0.

[25] Denis Barak, Beau Harrison, and Adam Watts, "Concepts Rookie Book," (2013), p 9, 11, http://operations.fnal.gov/rookie_books/concepts.pdf.

[26] M. J. Barnes *et al.,* "Injection and Extraction Magnets: Septa," arXiv:1103.1062.

[27] Adam Watts, "Magnetic Control of Fermilab Switchyard Beam Splits," Beams-5040, beamdocs.fnal.gov/AD/DocDB/0050/005040/001/magnetic-control-fermilab.pdf.

[28] Fermilab, ILC-SRF R&D. https://ilc.fnal.gov/ilc-srf.html.

[29] Tom Roberts, G4beamline Users Guide 2.16,
http://www.muonsinternal.com/muons3/G4beamline;
T. J. Roberts *et al.,* EPAC08-WEPP120.

[30] D. J. Summers *et al.,* "Final Muon Emittance Exchange in Vacuum for a Collider," IPAC-2015-TUPWI044.

[31] Hans Grote *et al.,* "The MAD-X Program (Methodical Accelerator Design) Version 5.02.08 Users Reference Manual," (2016), http://madx.web.cern.ch/madx/releases/last-dev/madxuguide.pdf; CERN-SL-90-13-AP.

[32] C. Rubbia, P. McIntyre, and D. Cline, "Producing Massive Neutral Intermediate Vector Bosons with Existing Accelerators," Print-76-0252-HARVARD.

[33] J. Peoples, "The Fermilab Antiproton Source," IEEE Trans. Nucl. Sci. **30** (1983) 1970.

[34] TeVI Group, "Design Report Tevatron 1 Project," FERMILAB-DESIGN-1984-01.

[35] R. J. Pasquinelli *et al.*, "Progress in Antiproton Production at the Fermilab Tevatron Collider," FERMILAB-CONF-09-126-AD.

[36] B. Franzke *et al.,* "Fast cooling of antiproton and radioactive ion beams in future storage rings at GSI," Nucl. Instrum. Meth. A **532** (2004) 97.

[37] C. Dimopoulou, "Beam Cooling Systems and Activities at GSI and FAIR," IPAC-2014-MOPRI067.

[38] B. C. Barish *et al.*, "An Assessment of the AntiProton-Proton Option for the SSC," SSC-SR-1022 (1986).

[39] D. J. Summers, *et al.,* "A 233 km Tunnel for Lepton and Hadron Colliders," AIP Conf. Proc. **1507** (2012) 860.

[40] G. T. Lyons, III, Master's Thesis, "A 233 km Circumference Tunnel for e^+e^-, $p\bar{p}$, and $\mu^+\mu^-$ Colliders," arXiv:1112.1105.

[41] W. de Boer, "The Discovery of the Higgs Boson with the CMS Detector and its Implications for Supersymmetry and Cosmology," arXiv:1309.0721.

[42] J. Alwall *et al.*, "The automated computation of tree-level and next-to-leading order differential cross sections, and their matching to parton shower simulations," JHEP **1407**, 079 (2014) doi:10.1007/JHEP07(2014)079 [arXiv:1405.0301 [hep-ph]].

[43] http://home.thep.lu.se/∼torbjorn/Pythia.html; T. Sjöstrand *et al.,* Comput. Phys. Commun. **191** (2015) 159.

[44] W. Barletta, M. Battaglia, M. Klute, M. Mangano, S. Prestemon, L. Rossi and P. Skands, "Future hadron colliders: From physics perspectives to technology R&D," Nucl. Instrum. Meth. A **764** (2014) 352.

[45] F. Zimmermann, "Future Highest-Energy Circular Colliders," PoS CORFU **2014**, 032.

[46] A. Donnachie and P. V. Landshoff, "pp and $\bar{p}p$ total cross sections and elastic scattering," Phys. Lett. B **727** (2013) 500.

[47] R. Tomás *et al.*, "FCC study: parameters and optics for hadron and lepton colliders," Nucl. Part. Phys. Proc. **273-275** (2016) 149.

[48] D. McGinnis, "Design Considerations for Antiproton stacking and cooling," Director's Review, May 2003 (unpublished), http://www-bd.fnal.gov/reviews/DirRev2003/Dir_Rev_May_03_McGinnis2.pdf.

[49] V. Lebedev, "Improvements to the Stacktail and Debuncher Momentum Cooling Systems," COOL09-MOA1MCCO02 (2009).

[50] D. McGinnis *et. al.,* "Plans for Tevatron Run IIb," Internal Fermilab document (2001).

[51] C. Hojvat and A. Van Ginneken, "Calculation of anti-Proton Yields for the Fermilab anti-Proton Source," Nucl. Instrum. Meth. **206** (1983) 67.

[52] S. Childress, R. Coleman, G. Koizumi, A. Malensek, C. D. Moore, R. Schailey, R. Stefanski and L. Stutte, "Fermilab Fixed Target Beams from the Main Injector," FERMILAB-TM-1599.

[53] H. Bichsel, D. E. Groom, and S. R. Klein, "Passage of particles through matter" (2004).

[54] K. Gollwitzer and J. Marriner, "Antiproton Sources," Handbook of Accelerator Physics and Engineering (2013) pp. 8-10.

[55] R. B. Palmer, "Stochastic Cooling in General and its Application to $\bar{p}$ Storage in Particular," BNL-18395.

[56] S. Nagaitsev *et al.*, "Experimental demonstration of relativistic electron cooling," Phys. Rev. Lett. **96** (2006) 044801.

[57] A. Shemyakin and L. R. Prost, "Ultimate Performance of Relativistic Electron Cooling at Fermilab," COOL-2011-THIOA01.

[58] V. Papadimitriou, "Luminosity determination at the Tevatron" arXiv:1106.5182.

[59] S. Nagaitsev, L. Prost,and A. Shemyakin, "Fermilab 4.3 MeV electron cooler" JINST **10** (2015) T01001.

[60] S. Nagaitsev *et al.*, "Commissioning of Fermilab's electron cooling system for 8-GeV antiprotons," Conf. Proc. C **0505161**, 540 (2005).

[61] S. Y. Lee, "Accelerator Physics." World Scientific (2012), p. 350.

[62] J. E. Dey and D. W. Wildman, "Wideband RF system for the Fermilab recycler ring," Conf. Proc. C **990329**, 869 (1999).

[63] J. G. Rushbrooke, "Proposal for Achieving $p\bar{p}$ Collisions at up to 1 TeV Center-of-Mass Energy by Means of Cyclic Variation of Stored Beam Energy in the SPS Collider," CERN-EP/82-6.

[64] C. Albajar *et al.* [UA1 Collaboration], "Production of Low Transverse Energy Clusters in $\bar{p}\,p$ Collisions at $\sqrt{s} = 0.2$ TeV to 0.9 TeV and their Interpretation in Terms of QCD Jets," Nucl. Phys. B **309** (1998) 405.

[65] G. W. Foster, "Multibatch $\bar{p}$ production via snap coalescing," FERMILAB-TM-1902.

[66] P. Derwent, S. Holmes and V. Lebedev, "An 800-MeV superconducting LINAC to support megawatt proton operations at Fermilab," arXiv:1502.01728 [physics.acc-ph].

[67] V. I. Telnov, "Restriction on the Energy and Luminosity of e^+e^- Storage Rings due to Beamstrahlung," Phys. Rev. Lett. **110** (2013) 114801.

[68] D. Neuffer, "Colliding Muon Beams at 90 GeV," FERMILAB-FN-0319 (1979).

[69] R. Palmer *et al.,* "Muon Colliders," AIP Conf. Proc. **372** (1996) 3.

[70] J. Gallardo *et al.,* "$\mu^+\mu^-$ Collider: Feasibility Study," Snowmass 1996, BNL-52503.

[71] C. M. Ankenbrandt *et al.,* "Status of muon collider research and development and future plans," Phys. Rev. ST Accel. Beams **2** (1999) 081001.

[72] M. M. Alsharo'a *et al.,* "Recent progress in neutrino factory and muon collider research within the Muon collaboration," Phys. Rev. ST Accel. Beams **6** (2003) 081001.

[73] M. Chung *et al.,* "Pressurized H_2 RF Cavities in Ionizing Beams and Magnetic Fields," Phys. Rev. Lett. **111** (2013) 184802.

[74] D. Stratakis, R. C. Fernow, J. S. Berg, and R. B. Palmer, "Tapered channel for six-dimensional muon cooling towards micron-scale emittances," Phys. Rev. ST Accel. Beams **16** (2013) 091001.

[75] D. Stratakis and R. B. Palmer, "Rectilinear six-dimensional ionization cooling channel for a muon collider: A theoretical and numerical study," Phys. Rev. ST Accel. Beams **18** (2015) 031003.

[76] D. Stratakis, "Advanced cooling scheme with gas filled rf cavities and discrete absorber," AIP Conf. Proc. **1777** (2016) 100008.

[77] Y. Bao *et al.,* "Conceptual design and modeling of a six-dimensional bunch merging scheme for a muon collider," Phys. Rev. Accel. Beams **19** (2016) 031001.

[78] D. Stratakis, "A hybrid six-dimensional muon cooling channel using gas filled rf cavities," JINST (2017).

[79] G. Ambrosio *et al.,* "Design Study for a Staged Very Large Hadron Collider," FERMILAB-TM-2149 (2001).

[80] CNA Consulting Engineers, "Estimate of Heavy Civil Underground Construction Costs for a Very Large Hadron Collider in Northern Illinois," VLHC-2001-CNA-REPORT.

[81] J. D. Jackson *et al.,* "Conceptual Design of the Superconducting Super Collider," SSC-SR-2020 (1986).

[82] "The Worlds Largest Super Collider Sits Abandoned In Texas," Wackulus, (June 24, 2015). http://wackulus.com/worlds-largest-super-collider-sits-abandoned-texas/.

[83] P. McIntyre *et al.,* "Higgs Factory and 100 TeV Hadron Collider: Opportunity for a New World Laboratory within a Decade," arXiv:1402.5973.

[84] Peter Kenyon, "Designing a 100 km collider tunnel for CERN," http://www.tunneltalk.com/CERN-10Dec2014-Future-Circular-Collider-preliminary-alignment-studies.php.

[85] M. Breidenbach and W. Barletta, "Accelerator Research in the U.S. for High Energy Physics: A biased perspective," ESS-DOC-371 (2015).

[86] G. W. Foster and E. Malamud, "Low cost hadron colliders at Fermilab: A Discussion paper," FERMILAB-TM-1976, FERMILAB-VLHCPUB-011.

[87] X. Cid Vidal and R. Cid Manzano, "Taking a Closer Look at the LHC (2017)," "http://www.lhc-closer.es/".

[88] CERN."http://lhc-machine-outreach.web.cern.ch/lhc-machine-outreach/components/magnets.htm".

[89] L. Bottura *et al.,* "16.2 T Peak Field Reached in RMC Racetrack Test Magnet," http://acceleratingnews.web.cern.ch/fcc.

[90] H. Laeger *et al.,* IEEE Trans. Magnetics **24** (1988) 835.

[91] A. Ballarino and J. P. Burnet, Adv. Ser. Direct. High Energy Phys. **24** (2015) 157.

[92] F. Su, J. Gao, M. Xiao, D. Wang, Y. W. Wang, S. Bai and T. J. Bian, "Method study of parameter choice for a circular proton-proton collider," Chin. Phys. C **40** (2016) 017001.

[93] V. Lebedev and V. Shiltsev, "Accelerator physics at the Tevatron Collider," p. 4, doi:10.1007/978-1-4939-0885-1.

[94] V. M. Abazov *et al.,* "The Upgraded D0 Detector," Nucl. Instrum. Meth. **A565** (2006) 463.

[95] P. Ferracin *et al.*, "Magnet Design of the 150 mm Aperture Low-β Quadrupoles for the High Luminosity LHC," IEEE Trans. Appl. Supercond. **24** (2014) 4002306.

[96] A.V. Zlobin, V.V. Kashikin, and J.B. Strait, "Aperture Limitations for 2nd Generation Nb_3Sn LHC IR Quadrupoles," PAC03-WPAE018.

[97] T. Sen, J. Strait, and A.V. Zlobin, "Second Generation High Gradient Quadrupoles for the LHC Interaction Regions," PAC-2001-RPPH083.

[98] S. Feher and J. Strait, "Estimated inner triplet quadrupole length and aperture for really large hadron colliders of E(beam) = 30, 60, 100 TeV," eConf C **960625**, ACC042 (1996).

[99] R. Martin, R. Tomás, and B. Dalena, "Interaction Region for a 100 TeV Proton-Proton Collider," IPAC-2015-TUPTY001.

LIST OF APPENDICES

APPENDIX A: G4BEAMLINE CODE

```
#physics QGSP disable=Decay
physics QGSP_BERT_EMX doStochastics=0 disable=Decay list=1
bug1021
g4ui when=4 "/vis/viewer/set/background 1 1 1"
particlecolor reference=0,1,0 proton=1,0,0
beam root particle=proton nEvents=18500 file=point_beam.root \
directory=NTuple name=z0 beamZ=-980

param pi=3.14159265
param Rho=(4000/(3*($pi/180)))
param z0=2000
param Blength=1500 // Dipole Length
param Sep1_length=6000 // Electrostatic Septa Length
param BSep1_length=3500 // Magnetic Septa (1) Length
param BSep2_length=3000 // Magnetic Septa (2) Length
param Cell_lenght=($Sep1_length+$BSep1_length+$BSep2_length)
##########################################################################
zntuple format=root z=-660 //Beam output Li Lens
zntuple format=root z=$Blength*2+$z0-610 //Beam divided into two
zntuple format=root z=$Blength*2+$z0+3*$Cell_lenght+33640 //Beams 1,2,3,4,5,6
zntuple format=root z=$Blength*2+$z0+6*$Cell_lenght+65790 //Beams 7,8,9
zntuple format=root z=$Blength*2+$z0+7*$Cell_lenght+86450 //Beams 10,11,12
##########################################################################
// Definiton of elements to use
lilens lens1 radius=10.0 length=186 current=500000 material=Li color=0,1,0 \
maxStep=0.1
```

```
genericquad quadD ironColor=1,1,0 fieldLength=660.0 ironLength=660.0 \
ironRadius=1220 apertureRadius=1200 gradient=-2.0 fringe=0 kill=1

genericquad quadF ironColor=0,1,0 fieldLength=660.0 ironLength=660.0 \
ironRadius=1220 apertureRadius=1200 gradient=2.0 fringe=0 kill=1

genericbend bend1 ironColor=0,0,1 fieldLength=$Blength fieldHeight=600 \
fieldWidth=380 ironLength=$Blength ironHeight=620 ironWidth=400 \
fieldMaterial=Vacuum kill=1 fringe=0 By=1.8

genericbend bend2 ironColor=0,0,1 fieldLength=$Blength fieldHeight=1200 \
fieldWidth=2280 ironLength=$Blength ironHeight=1220 ironWidth=2300 \
fieldMaterial=Vacuum kill=1 fringe=0 By=1.8

genericbend Esepta1 ironColor=0,0.8,0.8 fieldLength=$Sep1_length \
fieldHeight=2000 fieldWidth=600 ironLength=$Sep1_length ironHeight=2020 \
ironWidth=600.4 fieldMaterial=Vacuum kill=1 fringe=0 By=0.017

genericbend Esepta2 ironColor=0,0.8,0.8 fieldLength=$Sep1_length \
fieldHeight=2000 fieldWidth=350 ironLength=$Sep1_length ironHeight=2020 \
ironWidth=350.4 fieldMaterial=Vacuum kill=1 fringe=0 By=0.017

genericbend Bsepta1 ironColor=0.58,0,0.83 fieldLength=$BSep1_length \
fieldHeight=2000 fieldWidth=1000 ironLength=$BSep1_length ironHeight=2020 \
ironWidth=1008 fieldMaterial=Vacuum kill=1 fringe=0 By=0.1

genericbend Bsepta2 ironColor=1,0.55,0 fieldLength=$BSep2_length \
```

```
fieldHeight=2000 fieldWidth=1000 ironLength=$BSep2_length ironHeight=2020 \
ironWidth=1040 fieldMaterial=Vacuum kill=1 fringe=0 By=1

genericbend Bsepta1_1 ironColor=0.58,0,0.83 fieldLength=$BSep1_length \
fieldHeight=2000 fieldWidth=1000 ironLength=$BSep1_length ironHeight=2020 \
ironWidth=1008 fieldMaterial=Vacuum kill=1 fringe=0 By=0.1

genericbend Bsepta2_1 ironColor=1,0.55,0 fieldLength=$BSep2_length \
fieldHeight=2000 fieldWidth=1000 ironLength=$BSep2_length ironHeight=2020 \
ironWidth=1040 fieldMaterial=Vacuum kill=1 fringe=0 By=1

group separator
place Esepta1 z=$Sep1_length/2 x=300.2 By=-0.017
place Bsepta1 z=$Sep1_length+$BSep1_length/2 x=504 By=-0.1
place Bsepta2 z=$Sep1_length+$BSep1_length+$BSep2_length/2 x=520 By=-1.0
endgroup

group separator1
place Esepta2 z=$Sep1_length/2 x=-175.2 By=0.017
place Bsepta1 z=$Sep1_length+$BSep1_length/2 x=-504 By=0.1
place Bsepta2 z=$Sep1_length+$BSep1_length+$BSep2_length/2 x=-520 By=0.7
endgroup

group separator2
place Esepta1 z=$Sep1_length/2 x=-300.2 By=0.017 #By=0.017
place Bsepta1_1 z=$Sep1_length+$BSep1_length/2 x=-504 By=0.1
place Bsepta2_1 z=$Sep1_length+$BSep1_length+$BSep2_length/2 x=-520 By=1.0
```

```
endgroup


group separator3
place Esepta1 z=$Sep1_length/2 x=-300.2 By=0.017 #By=0.017
place Bsepta1_1 z=$Sep1_length+$BSep1_length/2 x=-504 By=0.1
place Bsepta2_1 z=$Sep1_length+$BSep1_length+$BSep2_length/2 x=-520 By=1.4
endgroup
tubs external length=186 outerRadius=30.0 innerRadius=10.0 color=0.0,0.8,0.0 \
material=Fe kill=1
tubs drift length=10000 outerRadius=500.0 color=0.1,0.1,0.1,0.4 material=Vacuum
tubs limite length=1000 outerRadius=8000.0 color=1.0,1.0,1.0 material=Fe kill=1
tubs limite1 length=200 outerRadius=800.0 color=1.0,1.0,1.0 material=Fe kill=1
##########################################################################
place external z=-760
place lens1 z=-760
place bend1 z=$Blength/2-660 By=1.8
cornerarc z=$Blength/2-660 angle=-4.31 centerRadius=1334
place quadF z=$Blength*2+$z0-330+50 x=-2
place separator1 z=2*$Blength+$z0+50+$Cell_lenght/2 x=-2
place quadD z=2*$Blength+$z0+50+$Cell_lenght+330 x=-2
##########################################################################
place quadF z=$Blength*2+$z0+$Cell_lenght+13040 x=450 rotation=Y1.0
place quadF z=$Blength*2+$z0+$Cell_lenght+13040 x=-1900 rotation=Y-6.0
place separator2 z=$Blength*2+$z0+(3/2)*$Cell_lenght+13370 x=-2380 rotation=Y-6.5
place quadD z=$Blength*2+$z0+2*$Cell_lenght+13700 x=600 rotation=Y1.0
place quadD z=$Blength*2+$z0+2*$Cell_lenght+13650 x=-3300 rotation=Y-6.0
##########################################################################
```

```
place quadF z=$Blength*2+$z0+2*$Cell_lenght+26360 x=800 rotation=Y1.0
place quadF z=$Blength*2+$z0+2*$Cell_lenght+26360 x=-4000 rotation=Y-6.0
place quadF z=$Blength*2+$z0+2*$Cell_lenght+26360 x=-6900 rotation=Y-13.0
//Beams 4, 5 & 6
place separator z=$Blength*2+$z0+(5/2)*$Cell_lenght+26740 x=-4392 rotation=Y-5.0
place separator2 z=$Blength*2+$z0+(5/2)*$Cell_lenght+26740 x=-4728 rotation=Y-5.5
//Beams 1, 2 & 3
place separator z=$Blength*2+$z0+(5/2)*$Cell_lenght+26640 x=-8385 rotation=Y-14.3
place separator2 z=$Blength*2+$z0+(5/2)*$Cell_lenght+26590 x=-8807 rotation=Y-14.3
place limite z=$Blength*2+$z0+3*$Cell_lenght+34640 x=-9500
place quadD z=$Blength*2+$z0+3*$Cell_lenght+26770 x=1000 rotation=Y1.0
place bend2 z=$Blength*2+$z0+3*$Cell_lenght+39100 x=1200 rotation=Y1.0
#########################################################################
place quadF z=$Blength*2+$z0+4*$Cell_lenght+39760 x=750 rotation=Y-2.0
place separator3 z=$Blength*2+$z0+(9/2)*$Cell_lenght+40140 x=149 rotation=Y-2.5
place quadD z=$Blength*2+$z0+(10/2)*$Cell_lenght+40470 x=-50 rotation=Y-3.0
#########################################################################
// Beams 7, 8 & 9
place quadF z=$Blength*2+$z0+(10/2)*$Cell_lenght+53130 x=-50 rotation=Y-2.0
place quadF z=$Blength*2+$z0+(10/2)*$Cell_lenght+53130 x=-3050 rotation=Y-8.5
place separator z=$Blength*2+$z0+(11/2)*$Cell_lenght+53460 x=-4015 rotation=Y-10.5
place separator2 z=$Blength*2+$z0+(11/2)*$Cell_lenght+53460 x=-4328 rotation=Y-10.5
place quadD z=$Blength*2+$z0+(12/2)*$Cell_lenght+53790 x=-450 rotation=Y-1.8
place bend2 z=$Blength*2+$z0+(12/2)*$Cell_lenght+65790 x=-850 rotation=Y-1.8
place limite z=$Blength*2+$z0+(12/2)*$Cell_lenght+67790 x=-11000
#########################################################################
//Beams 10, 11 & 12
```

```
place quadF z=$Blength*2+$z0+(12/2)*$Cell_lenght+77460 x=-2250 rotation=Y-4.8
place separator z=$Blength*2+$z0+(13/2)*$Cell_lenght+78450 x=-2810 rotation=Y-5.5
place separator2 z=$Blength*2+$z0+(13/2)*$Cell_lenght+78450 x=-3103 rotation=Y-5.7
place drift
```

APPENDIX B: MADX PROGRAM FILE

```
TITLE,'IR Beta Functions';
BEAM, PARTICLE=PROTON, PC=50000.0;
Q1: QUADRUPOLE, L=16.75, K1=0.3*605/50000; // K=0.3G[T/m]/p[GeV/c]
Q2: QUADRUPOLE, L=14.725, K1=-0.3*354/50000;
Q3: QUADRUPOLE, L=14.725, K1=-0.3*354/50000;
Q4: QUADRUPOLE, L=16.75, K1=0.3*605/50000;
D1: DRIFT, L=4.0;
D2: DRIFT, L=0.0;
D3: DRIFT, L=4.0;
D4: DRIFT, L=7.62;
IP: MARKER;
FP: MARKER;
FODO: LINE=(IP, D4, Q4, D3, Q3, D2, Q2, D1, Q1, FP);
USE, PERIOD=FODO;
TWISS,SAVE,BETX=0.14 ,BETY=0.14;
PLOT,HAXIS=S, VAXIS=BETX, BETY, colour=100, INTERPOLATE=TRUE;
PLOT, NOVERSION=true, HAXIS=S, HMIN=-1.0, HMAX=10.0, VAXIS1=BETX,BETY,
VMIN=0.0, VMAX=2.0, COLOUR=100, INTERPOLATE=TRUE,
TITLE="unmatched beta functions";
TWISS;
Value, TABLE(SUMM,Q1);
Value, TABLE(SUMM,Q2);
WRITE,TABLE=SUMM,FILE=print.dat;
```

VITA

Sandra J. Oliveros

Education

- Ph.D. Candidate in Physics, University of Mississippi - Oxford, 2017.
- M.A in Physics, University of Mississippi - Oxford, 2014.
- M.S in Physics, University of Puerto Rico - Mayaguez, 2010.
- B.S in Physics, District University of Bogota - Colombia, 2005.

Teaching Experience

- Teaching Assistant, Department of Physics and Astronomy, University of Mississippi 2012-2013.
- Teaching Assistant, Department of Physics, University of Puerto Rico - Mayaguez 2007.

Research Interests

My research interest is experimental high energy particle physics, particularly in the next generation of particle accelerators to explore new physics beyond the Standard Model.

Honors and Awards

- Dissertation Fellowship, University of Mississippi - Graduate School, Spring 2017.
- Zdravko Stipcevic Honors Fellowship, University of Mississippi, 2012-2013.

Publications

Proceedings:

• S. J. Oliveros, et al. High Luminosity 100 TeV Proton Antiproton Collider, NAPAC-2016-MOB3CO04.

• S. J. Oliveros, et al. Cooling for a High Luminosity 100 TeV Proton Antiproton Collider, COOL-2015-TUPF01.

• T. L. Hart, J. G. Acosta, L. M. Cremaldi, S. J. Oliveros, D. J. Summers and D. V. Neuffer. Final 6d Muon Ionization Cooling Using Strong Focusing Quadrupoles, NAPAC-2016-TUPOB44.

• J. G. Acosta, L. M. Cremaldi, T. L. Hart, S. J. Oliveros, D. J. Summers and D. V. Neuffer. Final Muon Ionization Cooling Channel using Quadrupole Doublets for Strong Focusing, COOL-2015-MOPF07.

• Don Summers, John Acosta, Lucien Cremaldi, Terry Hart, Sandra Oliveros, Lalith Perera, Wanwei Wu and David Neuffer. Final Muon Emittance Exchange in Vacuum for a Collider, IPAC-2015-TUPWI044 (arXiv:1505.01832).

• D.J. Summers, T.L. Hart, J.G. Acosta, L.M. Cremaldi, S.J. Oliveros, L.P. Perera and D.V. Neuffer. Muon Emittance Exchange with a Potato Slicer, arXiv:1504.03972.

Colombian Journal of Physics:

• S. Oliveros, J. Acosta, and N. Forero. Analisis espectral de la radiacion termica del tungsteno utilizando Labview . En: Colombia Revista Colombiana De Fisica ISSN: 012022650 ed: Revista De La Sociedad Colombiana De Fisica v.38 fasc.4 p.1671-1675, 2006.

• J. Acosta, S. Oliveros, and N. Forero. Diseno y construccion de un monocromador controlado con Labview. En: Colombia Revista Colombiana De Fisica ISSN: 01202650 ed: Revista De La Sociedad Colombiana De Fisica.v.38 fasc.4 p.1655-1659, 2006

• J. Acosta, S. Oliveros, and N. Forero. Determinacion del tiempo de respuesta de una termopila. En: Colombia Revista Colombiana De Fisica ISSN: 01202650 ed: Revista De La Sociedad Colombiana De Fisica v.38 fasc.2 p.758-762 , 2006.

Workshop - Conference Presentations

• High Luminosity 100 TeV Proton-Antiproton Collider. NAPAC 2016 Conference, Chicago IL, October 2016.

• Exploration of a High Luminosity 100 TeV Proton-Antiproton Collider. SESAPS 2015 Conference, Mobile AL, November 2015.

• Cooling for a 100 TeV ppbar Collider that Exploits Large qqbar to X Cross Sections. COOL Workshop 2015 - Poster Session, Jefferson Lab (Newport News, VA), July 2015.

• Study of the use of the micro-twisted pair cable links in the CMS pixel system. CMS Upgrade Workshop, Fermilab, October 2009.

• Address levels study using micro-twisted pair cables with different lengths. PIRE Workshop, University of Nebraska, September 2009.

• Twisted pair cable - impedance and transmission simulations. PIRE Workshop, University of Kansas, September 2008.